Dalitz Plot Analysis of the Decay $B^\pm \to K^\pm K^\pm K^\mp$

Thesis by

Alexei Dvoretskii

In Partial Fulfillment of the Requirements

for the Degree of

Doctor of Philosophy

California Institute of Technology

Pasadena, California

2006

(Defended March 20, 2006)

Acknowledgements

In an experiment as large as *BABAR* any result is ultimately only possible because of substantial dedicated contributions from many collaborators and the Stanford Linear Accelerator staff in the accelerator, detector, and computing groups, to whom I am deeply grateful.

Graduate school is a long experience — in my case, with a duration of almost eight years, particularly so. It is because of the wonderful people whom I have met at Caltech and during my stay in the Bay Area, too many to list here, that I will always remember this time with a lot of fondness. To all of you, thank you for you support and friendship.

Finally, I thank my family who have always been supportive and understanding of my desire to pursue a doctoral degree abroad.

Abstract

We perform an analysis of the three-body charmless decay $B^{\pm} \to K^{\pm}K^{\pm}K^{\mp}$ using a sample of 226.0 ± 2.5 million $B\overline{B}$ pairs collected by the *BABAR* detector and measure the total branching fraction and CP asymmetry to be $\mathcal{B} = (35.2 \pm 0.9 \pm 1.6) \times 10^{-6}$ and $A_{CP} = (-1.7 \pm 2.6 \pm 1.5)\%$. We fit the Dalitz plot distribution using an isobar model and report the measured values of magnitudes and phases of the production coefficients. The decay dynamics is dominated by the K^+K^- S-wave, for which we perform a partial-wave analysis in the region $m(K^+K^-) < 2\,\mathrm{GeV}/c^2$. We find no evidence of CP violation for individual components of the isobar model.

Contents

List of Figures

List of Tables

Chapter 1

Introduction

Rare charmless decays of B mesons provide a rich laboratory for studying different aspects of weak and strong interactions. Many branching fractions and CP asymmetries for such modes have now been measured at the high-luminosity SLAC and KEK B factories. The already considerable precision of such measurements will be further improved with still larger datasets that will become available within the next several years.

An understanding of strong interaction effects in B decays is often a prerequisite for precise determination of the weak interaction parameters. The experimental measurements from the B factories have motivated recent theoretical progress in developing phenomenological models of quantum chromodynamics (QCD) effects leading to specific predictions for two-body pseudoscalar-pseudoscalar, $B \to PP$, and pseudoscalar-vector, $B \to PV$, branching fractions and asymmetries [1–6]. Global fits to experimental data in the QCD factorization framework [7–9] show a reasonable agreement between theory and experiment and are already sensitive to the parameters of the Cabibbo-Kobayashi-Maskawa (CKM) quark mixing matrix. Hadronic uncertainties in these modes can also be controlled by relating measurements in different modes using the $SU(2)$ and $SU(3)$ symmetries in the light-quark sector. In particular, simultaneous measurements of CP asymmetries and branching fractions in isospin or $SU(3)$-related channels can provide information about the Unitarity Triangle angles α and γ [10–12].

Improved experimental measurements of a comprehensive set of charmless B decays coupled with further theoretical progress hold the potential to provide significant constraints on the CKM matrix

Table 1.1: Branching fractions for charmless decays of B mesons to fully-charged two-body and three-body final states [14].

B^0 decay	$\mathcal{B}$	$B^\pm$ decay	$\mathcal{B}$
$B^0 \to \pi^+\pi^-$	$(4.6 \pm 0.4) \times 10^{-6}$	$B^\pm \to \pi^\pm\pi^\pm\pi^\mp$	$(11 \pm 4) \times 10^{-6}$
$B^0 \to K^+\pi^-$	$(18.2 \pm 0.8) \times 10^{-6}$	$B^\pm \to K^\pm\pi^\pm\pi^\mp$	$(57 \pm 4) \times 10^{-6}$
$B^0 \to K^+K^-$	$< 0.6 \times 10^{-6}$	$B^\pm \to K^\pm\pi^\pm K^\mp$	$< 6.3 \times 10^{-6}$
		$B^\pm \to K^\pm K^\pm K^\mp$	$(30.8 \pm 2.1) \times 10^{-6}$

parameters and to discover hints of physics beyond the Standard Model in penguin-mediated $b \to s$ transitions.

We study the three-body charmless decay $B^\pm \to K^\pm K^\pm K^\mp$. Experimentally, it is one of the most accessible charmless modes having a relatively large branching fraction (Table 1.1) and a clean final state signature. In addition to measuring the overall branching fraction and CP asymmetry, our goal in this analysis is to describe the dynamics of the decay matrix element and study the K^+K^- spectrum. Light scalar meson spectroscopy is an area of active experimental and theoretical research. Among the most interesting questions, are the nature of the $f_0(980)$ resonance and searches for a possible light 0^{++} glueball state [13].

The CLEO collaboration measured the quasi-two-body branching fraction $\mathcal{B}(B^\pm \to K^\pm\phi) = (5.5^{+2.1}_{-1.8} \pm 0.6) \times 10^{-6}$, using a sample of 9.7 million $B\overline{B}$ decays [15]. Based on a sample of 88.8 million $B\overline{B}$ decays collected during 1999–2002, BABAR has previously reported the measurements of the total branching fraction and CP asymmetry, $\mathcal{B}(B^\pm \to K^\pm K^\pm K^\mp) = (29.6 \pm 2.1 \pm 1.6) \times 10^{-6}$, $A(B^\pm \to K^\pm K^\pm K^\mp) = (0.02 \pm 0.07 \pm 0.03)$ [16]; the quasi-two-body branching fraction and asymmetry $\mathcal{B}(B^\pm \to K^\pm\phi) = (10.0^{+0.9}_{-0.8} \pm 0.5) \times 10^{-6}$, $A(B^\pm \to K^\pm\phi) = 0.04 \pm 0.09 \pm 0.01$ [17]; and the quasi-two-body branching fraction $\mathcal{B}(B^\pm \to K^\pm\chi_{c0}) = (1.49^{+0.36}_{-0.34} \pm 0.22) \times 10^{-6}$ [18]. In a quasi-two-body analysis, possible interference effects between different decay channels leading to the same final state are neglected. This introduces a significant systematic uncertainty, thus limiting the applicability of the quasi-two-body approach to low-statistics analyses.

A more advanced formalism involves studying the structure of the full matrix element using a Dalitz plot fit. The most recent results published by the Belle collaboration are based on an isobar-

model amplitude analysis of the $B^\pm \to K^\pm K^\pm K^\mp$ Dalitz plot based on a sample of 152 million $B\overline{B}$ decays [19]. The total branching fraction, excluding the mode $B^\pm \to K^\pm \chi_{c0}$, is measured to be $\mathcal{B}(B^\pm \to K^\pm K^\pm K^\mp) = (30.6 \pm 1.2 \pm 2.3) \times 10^{-6}$.

We present herein the first *BABAR* amplitude analysis of the $B^\pm \to K^\pm K^\pm K^\mp$ Dalitz plot based on the dataset collected during Run 1–4 periods in 1999–2004. The dataset consists of $205.4\,\mathrm{fb}^{-1}$ taken on the $\Upsilon(4S)$ resonance corresponding to 226.0 million B^+B^- decays.

Chapter 2

Theory

This chapter describes the Standard Model (SM) theory of weak interactions as applied to charmless decays of $B^\pm$ mesons. While the weak interaction theory is well understood, the hadronic uncertainties due to the non-perturbative nature of QCD are difficult to estimate, complicating the extraction of the weak interaction parameters from the measurements of the branching fractions and CP asymmetries in hadronic decays of B mesons. We describe several phenomenological methods that lead to specific predictions for quasi-two-body branching fractions and asymmetries.

2.1   The Standard Model of quark weak interactions

The weak interaction in the quark sector of the SM is governed by the following Lorentz-invariant hermitian Lagrangian:

$$\mathcal{L} = -\frac{g}{\sqrt{2}} V_{ij} (\bar{U}_{i\alpha} D_{j\alpha})^\mu_{V-A} W^+_\mu + \text{h.c.},$$

describing a charged flavor-changing weak current transition between a left-handed up-like, (u, c, t), quark U and a left-handed down-like, (d, s, b), quark D mediated by an intermediate $W^\pm$ boson. The Greek indices indicate a sum over N_c QCD colors. Left-handed and right-handed quark currents are given by

$$(\bar{U}_{i\alpha} D_{j\alpha})^\mu_{V\mp A} = \bar{U}_{i\alpha}(1 \mp \gamma_5)\gamma^\mu D_{j\alpha}.$$

We have written the Lagrangian in terms of the quark mass eigenstates; the unitary Cabibbo-Kobayashi-Maskawa (CKM) matrix V_{ij} [20] describes the transformation between the mass eigen-
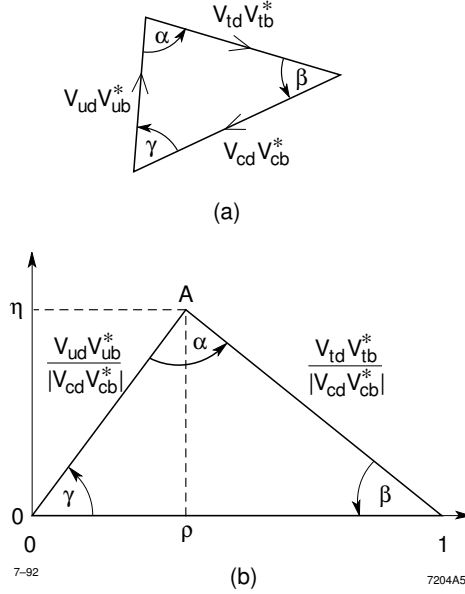
Figure 2.1: The Unitarity Triangle.

states and the weak interaction flavor eigenstates that define the weak current.

Because of the unitarity requirement and the freedom to choose the phases of the mass eigenstates, the three-generation quark mixing CKM matrix has four parameters, three real angles and one complex phase, that must be determined experimentally. The irreducible complex phase is the sole source of CP violation in the SM. A parameterization that makes manifest the relative sizes of the CKM matrix elements is due to Wolfenstein [21]:

$$V_{ij} = \begin{pmatrix} 1 - \frac{\lambda^2}{2} & \lambda & A\lambda^3(\rho - i\eta) \\ -\lambda & 1 - \frac{\lambda^2}{2} & A\lambda^2 \\ A\lambda^3(1 - \rho - i\eta) & -A\lambda^2 & 1 \end{pmatrix} + \mathcal{O}(\lambda^4),$$

where the Cabibbo angle [22], $\lambda = 0.221 \pm 0.002$, is used as an expansion parameter. For B meson decays the most important unitarity relation is

$$V_{ud}V_{ub}^* + V_{cd}V_{cb}^* + V_{td}V_{tb}^* = 0,$$

which defines the Unitarity Triangle (UT) shown in Fig. 2.1.
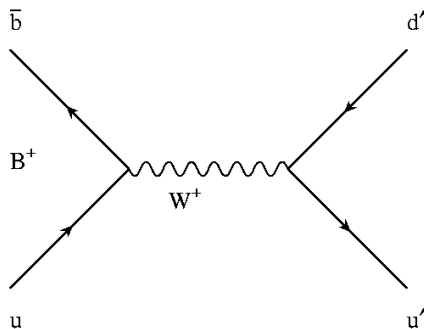
Figure 2.2: $B^{\pm}$ annihilation diagram.

Charged B mesons decay via the weak interaction primarily through the $b \to cW^-$ transition with an average lifetime of 1.5 ps [14]. The relatively long lifetime is due to the large mass of the virtual W meson and the smallness of the V_{cb} matrix element.

2.2 Low-energy effective Hamiltonian

To first order the matrix element of the transition is

$$\mathcal{M} = \frac{G_F}{\sqrt{2}} V_{Ub} V^*_{U'D'} Q_1 + \text{h.c.},$$

where $G_F/\sqrt{2} = g^2/8m_W^2$ is the Fermi constant and Q_1 is a transition operator given by

$$Q_1 = (\bar{b}_\alpha U_\alpha)^\mu_{V-A} (\bar{D'}_\beta U'_\beta)_{\mu V-A}.$$

The weak decays of the B mesons are dominated by diagrams in which the constituent b quark
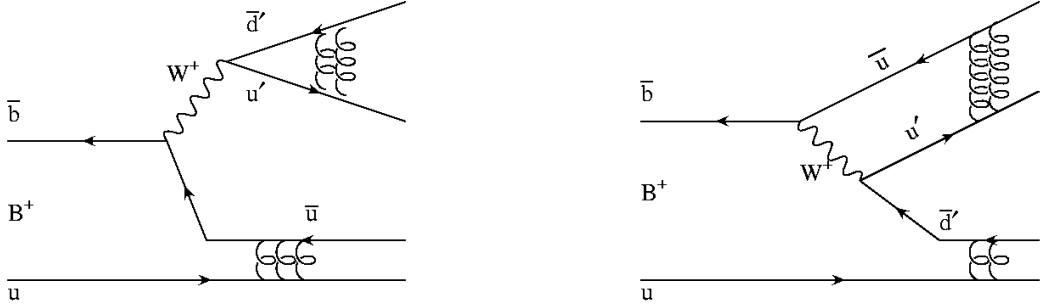
Figure 2.3: External (left) and internal (right) W-emission diagrams.

decays weakly and the light quark is a spectator. The contribution of annihilation topology diagrams (Fig. 2.2), where the charged current is formed by the constituent quarks of the $B^{\pm}$ meson, is small because of the small value of $|V_{ub}|$ and the helicity suppression [23].

The two possible spectator topologies corresponding to the $b \to U D' \bar{U}'$ transition induced by the Q_1 four-quark operator are the external and internal W-emission tree topologies (Fig. 2.3). The gluon exchange lines in Fig. 2.3 indicate the hadronization process into final state mesons. The internal-emission diagram is suppressed by a factor $1/N_c$ because the colors of the quarks in hadronizing mesons must match.

The exchange of hard gluons with virtualities between m_W and some relevant hadronic scale μ can introduce new types of operators. Quark color indices can be rearranged via the radiative correction to the W-emission diagram (Fig. 2.4) inducing the operator

$$Q_2 = (\bar{b}_\alpha U_\beta)^\mu_{V-A} (\bar{D}'_\beta U'_\alpha)_{\mu V-A}.$$

This operator corresponds to the same tree diagram topologies as in Fig. 2.3, but here the external-
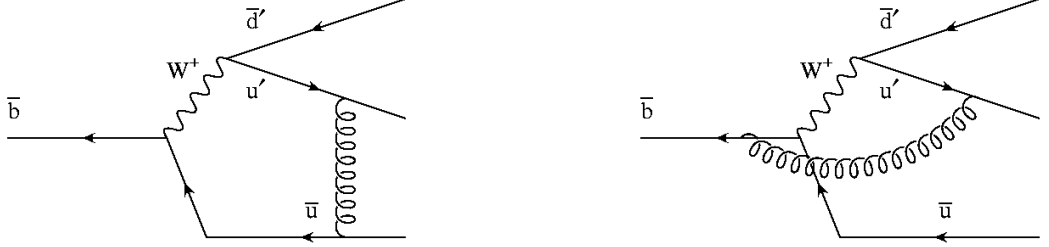
Figure 2.4: Examples of radiative correction to the tree diagrams inducing the Q_2 operator.

emission diagram is suppressed by $1/N_c$ with respect to the internal-emission diagram.

QCD penguin diagrams (Fig. 2.5), a different type of decay topology, correspond to the $b \to DQ\bar{Q}$ transition. As gluons couple to both left-handed and right-handed quarks, they give rise to the following four operators:

$$
\begin{aligned}
Q_3 &= (\bar{b}_\alpha U_\alpha)^\mu_{V-A} (\bar{Q}_\beta Q_\beta)^\mu_{V-A} \\
Q_4 &= (\bar{b}_\alpha U_\beta)^\mu_{V-A} (\bar{Q}_\beta Q_\alpha)^\mu_{V-A} \\
Q_5 &= (\bar{b}_\alpha U_\alpha)^\mu_{V-A} (\bar{Q}_\beta Q_\beta)^\mu_{V+A} \\
Q_6 &= (\bar{b}_\alpha U_\beta)^\mu_{V-A} (\bar{Q}_\beta Q_\alpha)^\mu_{V+A}.
\end{aligned}
$$

The contribution of QCD penguin diagrams is expected to be suppressed relative to the contribution of tree diagrams by a factor of order

$$
\frac{\alpha_s}{12\pi} \log \frac{m_t^2}{m_b^2} \sim 0.03,
$$
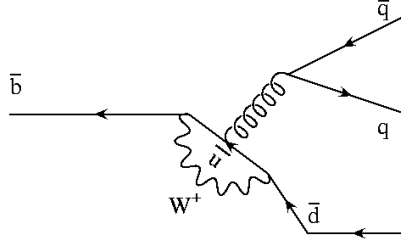
Figure 2.5: QCD penguin diagram.

where α_s is the strong interaction coupling constant. Electroweak penguin diagram topologies (Fig. 2.6) are even more suppressed by a similar factor due to the smallness of the respective coupling constants.

For the $B^{\pm} \rightarrow K^{\pm}K^{\pm}K^{\mp}$ decays considered here, the dominant contribution is due to the QCD penguin-mediated $b \rightarrow s\bar{s}s$ transition described by the Q_{3-6} operators with the $(\bar{b}s)(\bar{s}s)$ flavor structure. After the QCD effects are taken into account, the low-energy effective Hamiltonian is written as an operator product expansion in terms of four-quark operators Q_k, and the Wilson coefficients c_k:

$$\mathcal{H}_{\text{eff}} = \frac{G_F}{\sqrt{2}} \sum_{q=(u,c,t)} V_{qb}V_{qs}^* \sum_{k=3}^{6} c_k(\mu)Q_k(\mu) + \text{h.c.} \tag{2.1}$$

The Wilson coefficients account for the short-distance corrections arising from the exchange of gluons with virtualities between μ and m_W. They can be computed perturbatively, with the renormalization scale μ chosen to be of order m_B for B decays. As the Hamiltonian should not depend on the choice of scale, the scale dependence of the Wilson coefficients must cancel that of the current-current operators Q_k.
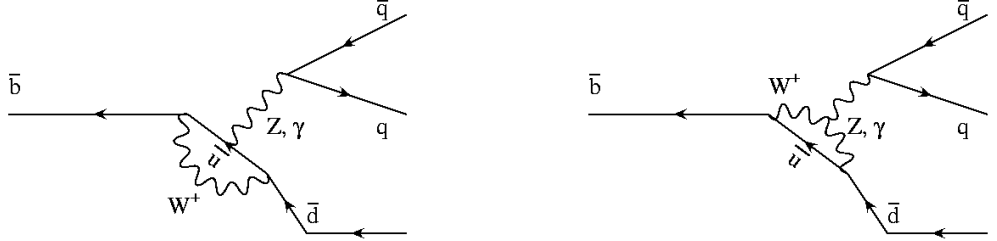
Figure 2.6: Electroweak penguin diagrams.

2.3 Direct CP violation

The Hamiltonian of Eq. (2.1) involves sums of products of the CKM matrix elements and the hadronic operators. The matrix element for the decay of a $B^{\pm}$ meson into a final state $f^{\pm}$ can be written as

$$\mathcal{M}(B^{\pm} \to f^{\pm}) = \sum_j |\mathcal{M}_j| e^{i(\delta_j \pm \phi_j)},$$

where ϕ_j are the "weak phases" and δ_j are the "strong phases". The weak phases arise because of the irreducible complex phase of the CKM matrix and change sign under CP conjugation. The strong phases are generated by the hadronic operators, e.g., in quark rescattering processes, and do not change sign under CP.

The CP asymmetry is defined as

$$A \equiv \frac{|\mathcal{M}(B^- \to f^-)|^2 - |\mathcal{M}(B^+ \to f^+)|^2}{|\mathcal{M}(B^+ \to f^+)|^2 + |\mathcal{M}(B^- \to f^-)|^2}.$$

The difference between the rates of two CP-conjugate processes is proportional to

$$|\mathcal{M}(B^- \to f^-)|^2 - |\mathcal{M}(B^+ \to f^+)|^2 = 2\sum_{i \neq j} |\mathcal{M}_i||\mathcal{M}_j| \sin(\delta_i - \delta_j)\sin(\phi_i - \phi_j),$$

hence CP violation can be generated through interference between terms with different weak phases that also acquire different strong phases. This type of CP violation is referred to as CP *violation in decay*, or *direct CP violation*, as opposed to CP violation produced in the interference between mixing and decay amplitudes in B^0 and $\overline{B}^0$ decays.

In the Hamiltonian of Eq. (2.1), the leading terms are proportional to $V_{cb}V_{cs}^*$ and $V_{tb}V_{ts}^*$, both of order $\mathcal{O}(\lambda^2)$ and having a zero weak phase. The term with a non-zero weak phase is supresed by $V_{ub}V_{us}^* = \mathcal{O}(\lambda^4)$. Direct CP violation in $B^\pm \to K^\pm K^\pm K^\mp$ in the SM is therefore expected to be small as has been confirmed experimentally by *BABAR* in Ref. [16].

2.4 Time-dependent CP asymmetry

The picture of CP violation is somewhat more complicated for decays of neutral B mesons into a CP eigenstate. The two neutral B mesons produced by a decay of the $\Upsilon(4S)$ are in a coherent state. In a time-dependent asymmetry measurement, the first neutral B decays into a tagging mode that identifies its flavor. At that time, taken to be zero, the second neutral B must have the opposite flavor. Because of $B^0\overline{B}^0$ mixing, the flavor eigenstates and the mass eigenstates (measured mass difference $\Delta m/\Gamma_B = 0.77 \pm 0.01$) of neutral B mesons are different. Therefore, when the second B decays into a CP eigenstate f_{CP} at time t, the decay amplitude is a superposition of B^0 and $\overline{B}^0$ decay amplitudes.

The asymmetry is defined in terms of decay rates into a CP eigenstate f_{CP} for time-evolving neutral B mesons that begin at time zero as a B^0 or a $\overline{B}^0$:

$$A(t) = \frac{\Gamma(B^0(t=0) \to f_{CP})(t) - \Gamma(\overline{B}^0(t=0) \to f_{CP})(t)}{\Gamma(B^0(t=0) \to f_{CP})(t) + \Gamma(\overline{B}^0(t=0) \to f_{CP})(t)}.$$

Defining

$$
\begin{aligned}
\mathcal{M}(B^0 \rightarrow f_{CP}) &= \sum_j |\mathcal{M}_j| e^{i(\delta_j + \phi_j)}, \\
\mathcal{M}(\overline{B}^0 \rightarrow f_{CP}) &= \sum_j |\mathcal{M}_j| e^{i(\delta_j - \phi_j)},
\end{aligned}
$$

and a direct CP asymmetry:

$$
A_0 = \frac{|\mathcal{M}(B^0 \rightarrow f_{CP})|^2 - |\mathcal{M}(\overline{B}^0 \rightarrow f_{CP})|^2}{|\mathcal{M}(B^0 \rightarrow f_{CP})|^2 + |\mathcal{M}(\overline{B}^0 \rightarrow f_{CP})|^2},
$$

it can be shown that

$$
A(t) = A_0 \cos(\Delta m_B t) - \eta_{CP} \Im(\lambda)(1 - A_0) \sin(\Delta m_B t),
$$

where η_{CP} is the CP parity of the final state and

$$
\lambda = \frac{V_{td} V_{tb}^*}{V_{td}^* V_{tb}} \frac{\mathcal{M}(\overline{B}^0 \rightarrow f_{CP})}{\mathcal{M}(B^0 \rightarrow f_{CP})}.
$$

Even when the direct CP asymmetry is zero,

$$
A(t) = -\eta_{CP} \sin(\arg(\lambda)) \sin(\Delta m_B t),
$$

showing that there can still be time-dependent CP asymmetry. Further, if the leading terms in the sums of Eq. (2.2) have the same weak phase ϕ, the hadronic uncertainties cancel giving $\arg(\lambda) = -2(\beta + \phi)$. This is the case for $B^0 \rightarrow J/\psi K_s^0$, where $A(t) \propto \sin 2\beta$, and the measurement of the time-dependent asymmetry gives the best determination of the UT angle β to date.

Measurements of time-dependent CP asymmetries in charmless final states can be sensitive to the other two angles of the UT. However, for most final states f_{CP}, the contributing diagrams have different weak phases and an understanding of the hadronic uncertainties is needed to relate the asymmetry measurements to the underlying parameters of the weak interaction. This can be

done by calculating the hadronic contributions in a model-dependent way using phenomenological approaches, some of which are described in the sections below.

Another approach is to use light-quark symmetry to control hadronic uncertainties in a model-independent way. It was shown in Ref. [10, 11] that by measuring the decay rates in isospin-related $B \rightarrow \rho\pi$ channels, hadronic uncertainties due to penguin contributions can be eliminated. It is possible then to determine the UT angle α without ambiguities by a time-dependent Dalitz plot analysis of $B^0 \rightarrow \pi^+\pi^-\pi^0$. It has also been shown that $SU(3)$ symmetry can be used to bound the hadronic uncertainties in the CP asymmetry measurements in the $B^0 \rightarrow \eta' K_S^0$ and $B^0 \rightarrow \phi K_S^0$ decays [12]. In all cases, it is necessary to measure decay rates and CP asymmetries in many channels related by isospin or $SU(3)$. A global $SU(3)$ fit in Ref. [24] has shown sensitivity to the UT angle γ and predictions have been made for yet-unobserved channels.

2.5 Factorization

At present, the evaluation of hadronic matrix elements is not possible by direct calculation, e.g., by using lattice QCD techniques. This has motivated the development of several phenomenological models. Factorization [25, 26] is a powerful theoretical tool, which has been successfully used to relate the hadronic matrix elements to experimentally measured parameters.

The basis of factorization is the color-transparency argument: in two-body decays of B mesons the light quark-antiquark pair that couples to the W boson is created with a high momentum in a color singlet; it leaves the interaction region quickly and then undergoes hadronization. The quark-antiquark pair effectively behaves like a pointlike colorless particle. Soft gluons, therefore, are ineffective in rearranging the quarks. The remaining quark produced by the b quark decay picks up the spectator quark and undergoes hadronization. To first order, there is no interaction between the two components, and the matrix elements are expected to factorize into products of color-singlet quark currents.

For a two-body decay, such as $B^\pm \to K^\pm \phi$, we can then write in the factorization approximation

$$< K^\pm \phi | (\bar{b}s)^\mu (\bar{s}s)_\mu | B^\pm > \; = \; < K^\pm | (\bar{b}s)^\mu | B^\pm > < \phi | (\bar{s}s)_\mu | 0 > .$$

The factorized matrix elements can be related to experimentally measurable quantities:

$$< \phi | (\bar{s}s)^\mu | 0 > \quad = \quad \epsilon^\mu f_\phi m_\phi, \tag{2.2}$$

$$< K^\pm | (\bar{b}s)^\mu | B^\pm > \quad = \quad F_+(q^2) p^\mu + (F_0(q^2) - F_+(q^2)) \frac{pq}{q^2} q^\mu, \tag{2.3}$$

where $f_\phi = 237 \pm 4\,\mathrm{MeV}$ is the ϕ-meson decay constant describing the strength of the $\bar{s}s$ quark interaction inside the ϕ, ϵ^μ is the polarization of the ϕ vector resonance, $p^\mu \equiv p_B^\mu + p_K^\mu$. Transition form factors, $F_0^{BK}(q^2)$ and $F_+^{BK}(q^2)$ [27], are functions of the momentum transfer, $q^\mu \equiv p_B^\mu - p_K^\mu$, and can be meausured in semileptonic decays, such as $B \to K l \bar{\nu}$.

The *naive factorization* (NF) framework outlined above in many cases provides predictions of the branching fractions that have the correct order of magnitude. However, it has two significant shortcomings. Firstly, the hadronic operator matrix elements evaluated in terms of the form factors of Eq. (2.3) are independent of the renormalization scale μ, and thus cannot cancel the scale dependence of the Wilson coefficients. Secondly, under the assumption of no rescattering, the matrix elements of the hadronic operators are all real. Therefore, under NF, direct *CP* asymmetries are always zero. Finally, for $B^\pm \to K^\pm \chi_c$, where χ_c are 0^{++} charmonium states, the prediction for the branching fraction is $\mathcal{B}(B^\pm \to K^\pm \chi_c) \propto | < \chi_c | (\bar{c}c)_{V \mp A} | 0 > |^2 = 0$ under NF. The form factor vanishes because the di-quark current and the meson have opposite *CP* parity. The observations of the decay $B^\pm \to K^\pm \chi_{c0}$ by the *BABAR* and Belle collaborations [18, 19, 28] clearly show that the factorization assumption breaks down in this case.
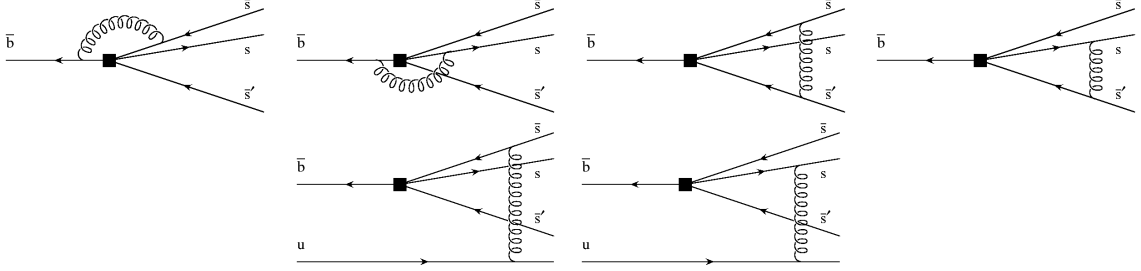
Figure 2.7: First-order gluon exchanges contributing to the Type I (top) and Type II (bottom) QCDF scattering kernels.

2.6   QCD factorization

These shortcomings motivated the development of an extended approach, called QCD factorization (QCDF) [29, 30]. In QCDF, hard scattering corrections of order α_s and $\Lambda_{\mathrm{QCD}}/m_b$ are systematically evaluated. They introduce a scale dependence into the matrix elements of hadronic operators, restoring the overall scale independence, and also give rise to complex scattering phases that can generate direct CP violation.

Under NF, the dynamics of the strong interactions is absorbed into products of transition form factors and meson decay constants. In QCDF this product is replaced by a more general expression given by

$$F^{BK}(q^2)f_\phi \rightarrow F^{BK}(q^2)\int T^I(x)\Phi_\phi(x)dx + \int T^{II}(\xi,x,y)\Phi_B(\xi)\Phi_K(x)\Phi_\phi(y)dxdyd\xi.$$

The first term describes hard gluon exchanges without the participation of the spectator quark (Fig. 2.7, top). The spectator quark is simply picked up by a final-state kaon through soft gluon exchange, and this process is characterized by the transition form factor. The scattering kernel T^I then describes the corrections to the four-quark effective vertex. The integration is performed over light meson distribution functions Φ. The second term, with a scattering kernel T^{II}, describes six-quark vertices where the spectator quark is involved in scattering (Fig. 2.7, bottom), and annihilation type diagrams.

The long-distance perturbative effects are absorbed into the transition form factor and provide

the overall normalization of the meson distribution functions. The scattering kernels are calculated perturbatively. Formally, in the limit of $m_b \to \infty$, QCDF reduces to the NF formula. In the QCDF framework, the strong phases are suppressed by α_s, and therefore the predicted CP asymmetries are small.

2.7 Perturbative QCD

Perturbative QCD (PQCD) [31] is an alternative theoretical framework that gives somewhat different predictions for charmless decays. The non-perturbative long-distance effects are included in the universal meson wave functions that parameterize the distribution of momentum between the partons inside the meson. Whereas in QCDF the effective theory is defined at the energy scale $\mu \sim m_b$, in PQCD the matching is done at a lower scale. This introduces large double logarithms of order $\log^2(m_b/\mu)$. It is argued that the resummation of these logarithms introduces form factors that suppress the long-distance effects, and that most of the contribution to the transition form factors is from the region where $\alpha_s/\pi < 0.3$, which justifies a perturbative calculation. In PQCD, therefore, the strong phases arise in the leading order and predicted CP asymmetries can be large. PQCD also predicts larger contributions for penguin and annihilation diagrams due to the enhancement of the corresponding Wilson coefficients evolved to a lower mass scale.

2.8 Intrinsic charm

The large observed branching fraction in $B^\pm \to K^\pm \chi_{c0}$ has highlighted the importance of intrinsic charm (IC) contributions to three-body charmless final states [32–35]. Typical rescattering diagrams for the decay $B^\pm \to K^\pm \chi_{c0}$ are shown in Fig. 2.8. These diagrams are formally suppressed, because rescattering is required to produce a charmless final state, but can give competitive contributions because they correspond to CKM-favored tree and penguin $b \to c\bar{c}s$ transitions.
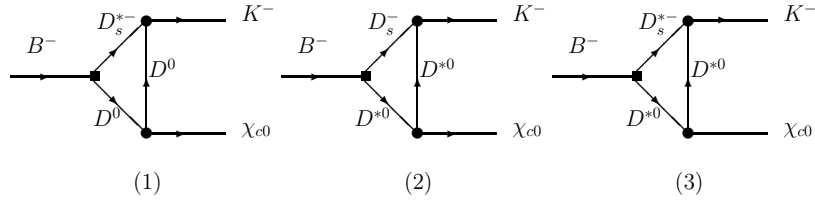
Figure 2.8: Typical rescattering diagrams with intrinsic charm for the decay $B^{\pm} \to K^{\pm}\chi_{c0}$. The boxes and disks represent effective weak and strong vertices, respectively.

Table 2.1: Theoretical predictions of branching fractions and CP asymmetries for charmless quasi-two-body decays.

Mode	Ref.	Method	$\mathcal{B}$	A
$B^{\pm} \to K^{\pm}\phi$	[36]	NF	$(2.5 - 15) \times 10^{-6}$	-
	[1]	QCDF	$(4.3^{+3.0}_{-1.4}) \times 10^{-6}$	-
	[2, 37]	NF	$(3.8 - 3.9) \times 10^{-6}$	-
		QCDF	$(6.2 - 7.2) \times 10^{-6}$	$(1.0 - 1.4)\%$
	[3]	QCDF	$(2.5 - 11.6) \times 10^{-6}$	$(0.6 - 1.7)\%$
	[4]	PQCD	$(10.2^{+3.9}_{-2.1}) \times 10^{-6}$	-
	[24]	$SU(3)$ fit	$(8.7 \pm 0.4) \times 10^{-6}$	-
$B^{\pm} \to K^{\pm}f_0(980)$	[5]	QCDF	$(5.5 - 10.9) \times 10^{-6}$	-
$B^{\pm} \to K^{\pm}\chi_{c0}$	[6]	IC	$(1.3 - 3.5) \times 10^{-4}$	-

2.9 Theoretical predictions

Significant theoretical progress has been made as outlined above. Global fits to the available data peformed using the QCDF [7, 8] framework show a reasonable agreement between theory and experiment. The experimental and theoretical uncertainties are still large, but global fits performed in Ref. [9] already show some sensitivity to the CKM matrix parameters. Charmless decays therefore have a lot of promise to further constrain the parameters of the weak interaction, once a better understanding of the hadronic phenomenology is achieved. In Table 2.1 we summarize current phenomenological predictions of quasi-two-body branching fractions and asymmetries for decays contributing to the $K^{\pm}K^{\pm}K^{\mp}$ final state.

Chapter 3

PEP-II and the *BABAR* Detector

In this chapter we briefly discuss the SLAC B factory complex, which consists of the PEP-II collider used to produce a large sample of $B\bar{B}$ pairs in e^+e^- collisions, and the *BABAR* detector used to detect the products of B meson decays.

3.1 PEP-II

The PEP-II [38] is a high-luminosity asymmetric energy e^+e^- collider at the Stanford Linear Accelerator Center (SLAC) with two storage rings: the high-energy ring (HER) storing $9.0\,\mathrm{GeV}$ electrons and the low-energy ring (LER) storing $3.1\,\mathrm{GeV}$ positrons. The two rings are located in the PEP tunnel with a circumference of $2.2\,\mathrm{km}$ and are filled from the existing $3\,\mathrm{km}$ SLAC linear accelerator complex (Fig. 3.1).

The two beams are brought together and collide head-on at Interaction Region 2 where the *BABAR* detector is located. The nominal center-of-mass energy of the two beams is $\sqrt{s} = 10.580\,\mathrm{GeV}$, just above the $B\bar{B}$ threshold and corresponding to the peak cross-section for the production of the $\Upsilon(4S)$ $b\bar{b}$ resonance, $\sigma(e^+e^- \to \Upsilon(4S)) = 1.1\,\mathrm{nb}$.

Other important processes at this energy include the production of lighter quark pairs: $\sigma(e^+e^- \to d\bar{d}) = 0.35\,\mathrm{nb}$, $\sigma(e^+e^- \to u\bar{u}) = 1.39\,\mathrm{nb}$, $\sigma(e^+e^- \to s\bar{s}) = 0.35\,\mathrm{nb}$, $\sigma(e^+e^- \to c\bar{c}) = 1.30\,\mathrm{nb}$; leptoproduction $\sigma(e^+e^- \to \mu^+\mu^-) = 1.16\,\mathrm{nb}$, $\sigma(e^+e^- \to \tau^+\tau^-) = 0.94\,\mathrm{nb}$; and Bhabha scattering with $\sigma(e^+e^- \to e^+e^-) \sim 0.4\,\mathrm{nb}$ within the acceptance of the *BABAR* detector [39]. A fraction of the data is taken 40 MeV below the $\Upsilon(4S)$ peak, about 20 MeV below the $B\bar{B}$ threshold, and is used
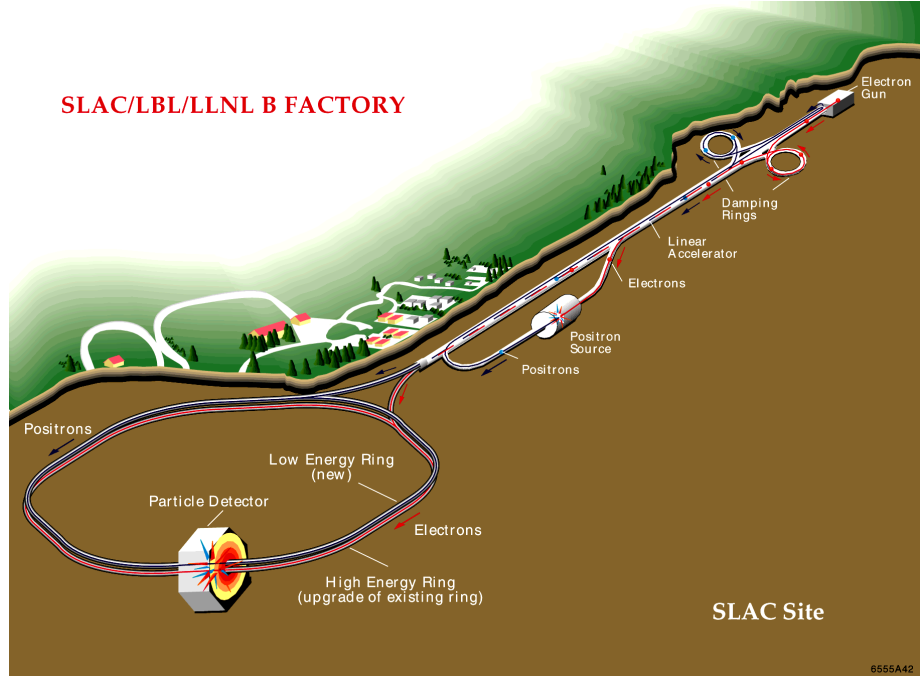
Figure 3.1: Schematic drawing of the PEP-II storage ring and the linear accelerator complex.

to study backgrounds due to these processes.

The $\Upsilon(4S)$ resonance decays predominantly to a pair of $B\overline{B}$ mesons each with a momentum of $0.335\,\mathrm{GeV}$ in the center of mass. A key feature of the B factory is the boost of $\beta\gamma = 0.56$ between the center-of-mass frame and the lab frame. Because of the boost the typical distance between the decay vertices of the two B mesons Δz is increased to $\beta\gamma c\tau \sim 250\,\mu$m, well within the resolution of the *BABAR* silicon vertex tracker. Sensitivity to Δz makes it possible to perform time-dependent analysis of CP asymmetries in decays of B^0 and $\overline{B}^0$. The application of this powerful technique to the $B^0(\overline{B}^0) \to J/\psi K_S^0$ decay has allowed the determination of the weak sector mixing matrix parameter $\sin 2\beta$ with great precision [40].

This analysis studies decays of charged B mesons, and we do not make use of the Δz information. However, because the branching fractions for charmless three-body B decays are very small, a critical factor for this analysis is the other unique feature of the B factory — its high luminosity. This analysis is based on a sample of 226.0 ± 2.5 million $B\overline{B}$ pairs collected during Run 1–4 data-taking periods in 1999–2004. The integrated luminosity delivered by PEP-II and recorded by *BABAR*
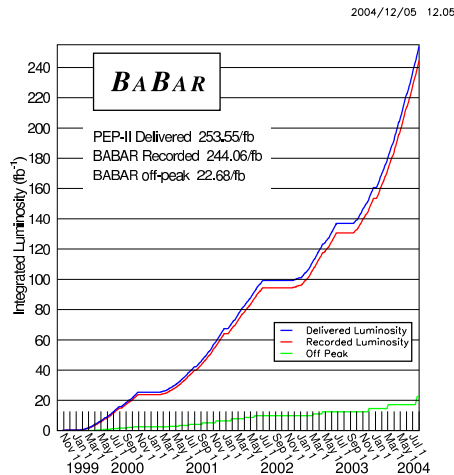
Figure 3.2: Integrated luminosity delivered by PEP-II and recorded by *BABAR* during the Run 1–4 data taking periods in 1999–2004.

is shown in Fig. 3.2. The total integrated Run 1–4 luminosity is $210.6\,\mathrm{fb}^{-1}$ taken at the $\Upsilon(4S)$ resonance and $21.6\,\mathrm{fb}^{-1}$ taken 40 MeV below. The dataset used in this analysis corresponds to the integrated luminosity of $205.4\,\mathrm{fb}^{-1}$ and $16.1\,\mathrm{fb}^{-1}$ on-peak and off-peak, respectively.

3.2 The *BABAR* detector

The *BABAR* detector [41] is a multisystem particle detector optimized for the study of B meson decays at a high-luminosity asymmetric-energy B factory. A schematic drawing of the *BABAR* detector is shown in Fig. 3.3. The *BABAR* detector consists of five subdetector systems. They are, in order of increasing distance from the interaction point (IP): the silicon vertex tracker (SVT), the drift chamber (DCH), the detector of internally-reflected Cherenkov light (DIRC), the electromagnetic calorimeter (EMC), and the instrumented flux return (IFR). The first four subsystems are located inside a superconducting solenoid that provides a 1.5 T magnetic field. The data acquisition system (DAQ) provides event triggering, data readout, and detector control and monitoring.
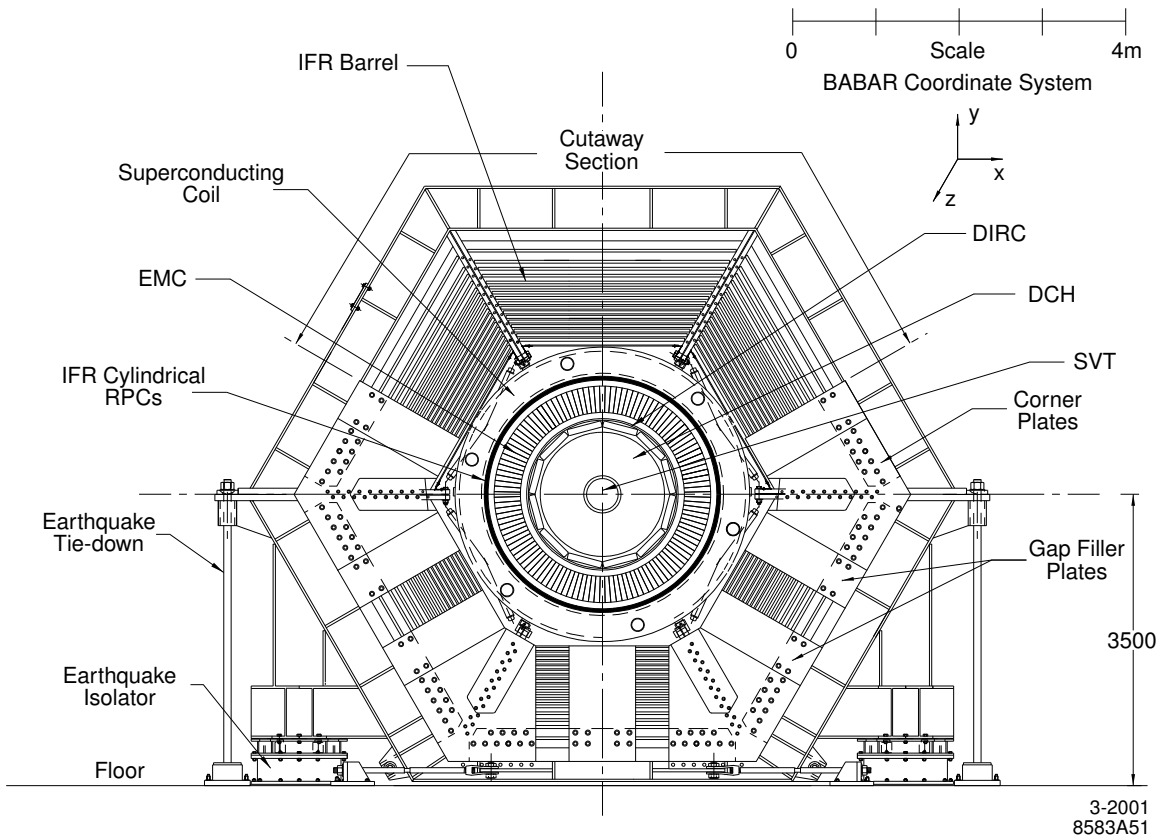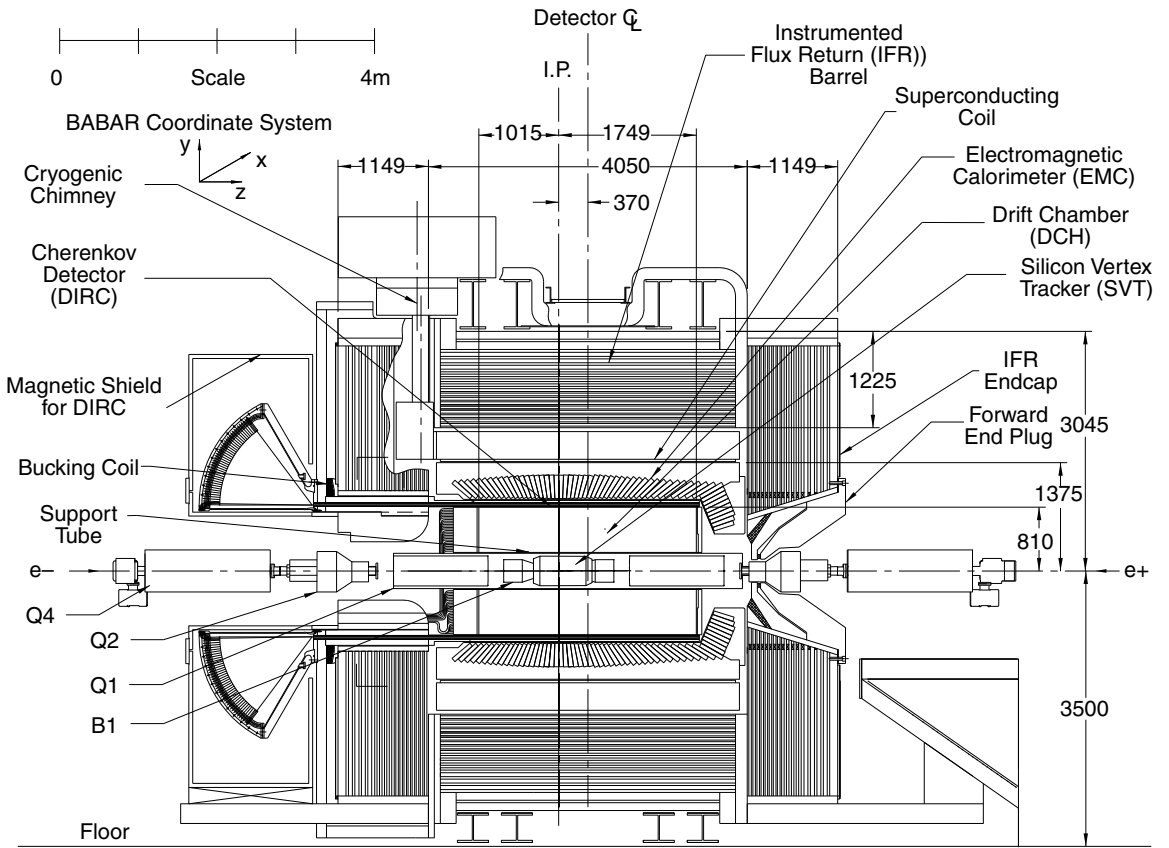
Figure 3.3: Schematic drawing of the *BABAR* detector.

The *BABAR* coordinate system is right-handed, with an origin at the nominal interaction point. The z axis is along the axis of the DCH in the direction of the higher-energy electron beam; the y axis points vertically upward; and the x axis points horizontally outward from the center of the storage rings.

3.3   The silicon vertex tracker

The SVT and the DCH, the two innermost systems of the *BABAR* detector, are used jointly for charged particle tracking.

For the rare charmless three-body decays considered here, the high efficiency of *BABAR* particle tracking is critical. Its excellent momentum resolution is essential for reconstructing this and many other exclusive B and D decays and rejecting combinatorial backgrounds; it also enables us to study the dynamic aspects of the matrix element of the decay. Precise tracking is also necessary for extrapolating particle trajectories into the DIRC, EMC, and IFR, and improves the overall performance of those systems as well.

Precise vertexing is less important for the decay considered in this analysis. It is critical, however, for time-dependent analyses of CP violation in decays of neutral B. In this analysis most final state particles will have momenta greater than $0.7\,\mathrm{GeV}/c$. In many other analyses, however, particle ID for slow final state particles will be provided by the dE/dx measurements in the tracking detectors.

In the 1.5 T magnetic field of the solenoid, the helical trajectory formed by a charged particle with transverse momentum $p_T > 0.18\,\mathrm{GeV}/c$ extends beyond the outermost layer of the DCH. DCH-only tracking is possible for momenta down to $p_T > 0.12\,\mathrm{GeV}/c$. For transverse momenta $p_T < 0.12\,\mathrm{GeV}/c$ SVT information must be used.

The helical trajectory is parameterized by five parameters: the distance of closest approach to the z axis, d_0; the corresponding azimuthal angle, ϕ_0; the corresponding z coordinate, z_0; the dip angle λ; and the curvature, which is inversely proportional to the transverse momentum $\omega = 1/p_T$.

The SVT has been designed to provide precise reconstruction of particle trajectories and vertices near the IP. The SVT is also a standalone tracker for charged particles that do not enter the DCH,

considerably expanding the transverse momentum coverage down to about $80 \, \text{MeV}/c$.

The SVT consists of five layers of double-sided silicon microstrip sensors arranged as shown in Fig. 3.4. The segmentation into strips is along the z axis of the detector on the inner side and azimuthally on the outer side. Each SVT module is divided into a forward and a backward half and is read out from both ends.

The SVT dominates the resolution of the vertex parameters, (d_0, ϕ_0, z_0), giving on average $\sigma(d_0) = 23 \, \mu\text{m}$ and $\sigma(z_0) = 29 \, \mu\text{m}$.

3.4   The drift chamber

The DCH is the main charged-particle tracker. The DCH design requirements include: efficient detection of charged particles with high momentum resolution over a wide range of particle momenta; maximum hermiticity; small amount of material in front of the EMC to avoid energy resolution degradation; small outer radius to minimize the cost of the EMC; longitudinal resolution better than $1 \, \text{mm}$ for K_S^0 vertex reconstruction; high dE/dx resolution necessary for particle identification for particles with momenta less than $700 \, \text{MeV}/c$; fast trigger input to the charged particle trigger; and ability to operate reliably in the presence of large machine backgrounds.

The drift chamber (Fig. 3.5) is a cylinder with an inner radius of $23.6 \, \text{cm}$ and an outer radius of $80.9 \, \text{cm}$, offset from the IP by $370 \, \text{mm}$ in the direction of the electron beam to provide better forward coverage.

The chamber consists of 7104 hexagonal drift cells arranged in 40 layers, each 4 layers forming a superlayer. Superlayers 1, 4, 7, and 10 are axial with the wires parallel to the z axis. The other superlayers have wires strung at a small stereo angle enabling z coordinate measurements. The stereo angle of the wires increases from $+45 \, \text{mrad}$ to $-76 \, \text{mrad}$ going outward with alternating positive and negative stereo superlayers.

The working gas mixture is a 4:1 mixture of helium and isobutane. Charge particles leave a trace of ionization in the drift cell; the ionization electrons are accelerated towards the sense wires causing an avalanche; the signal on the sense wires is read out by the front-end electronics mounted

580 mm

Space Frame

Bkwd.
support
cone

520 mrad

e⁻

VI   IV   IV   IV   IV   IV   IV
IV   IV   IV   V   IV   IV
VI   V   V   V   V   IV
VI
III   III   III   III   III   III
II   II   II   II
I   I   I   I

Fwd. support
cone

350 mrad

e⁺

Front end
electronics

Beam Pipe

Beam Pipe 27.8mm radius

Layer 5a

Layer 5b

Layer 4b

Layer 4a

Layer 3

Layer 2

Layer 1
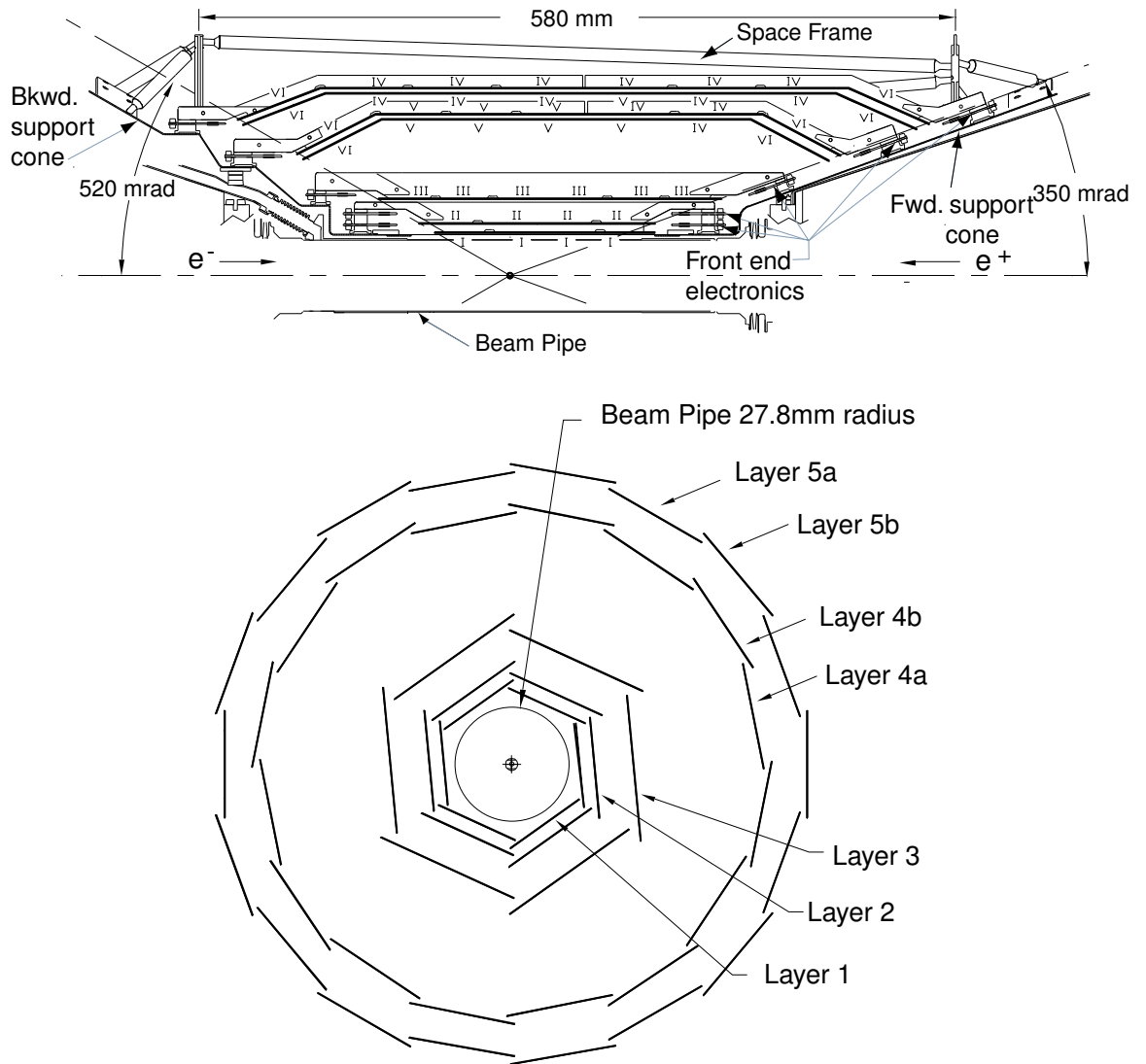
Figure 3.4: Schematic drawing of the SVT.
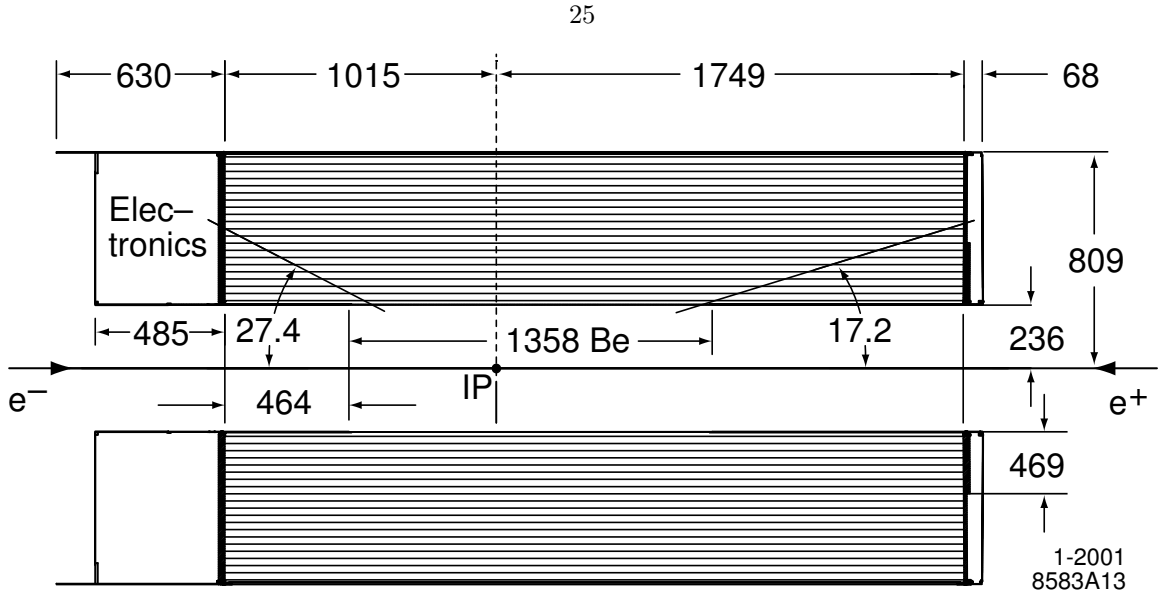
Figure 3.5: Longitudinal section of the DCH.

at the back of the DCH. The operating voltage on the sense wires for the majority of the data-taking period was 1930V.

The leading edge of the signal is detected to provide a measurement of the drift time, which is converted into a measurement of the closest approach to the sense wire. A pattern-matching algorithm is then used to reconstruct the trajectory of the particle. The timing information is also used for providing the trigger to the other detector subsystems. A truncated mean of the lowest 80% of the total charge deposited by a particle along its trajectory is used to measure dE/dx.

The drift chamber provides transverse momentum resolution of

$$\sigma(p_T)/p_T = (0.13 \pm 0.01)\% \cdot p_T + (0.45 \pm 0.03)\%.$$

The rms dE/dx resolution has been measured to be 7.5%, providing reliable K/π separation at a level of 3 standard deviations up to a momentum of about $0.55 - 0.60\,\mathrm{GeV}/c$ (Fig 3.6).
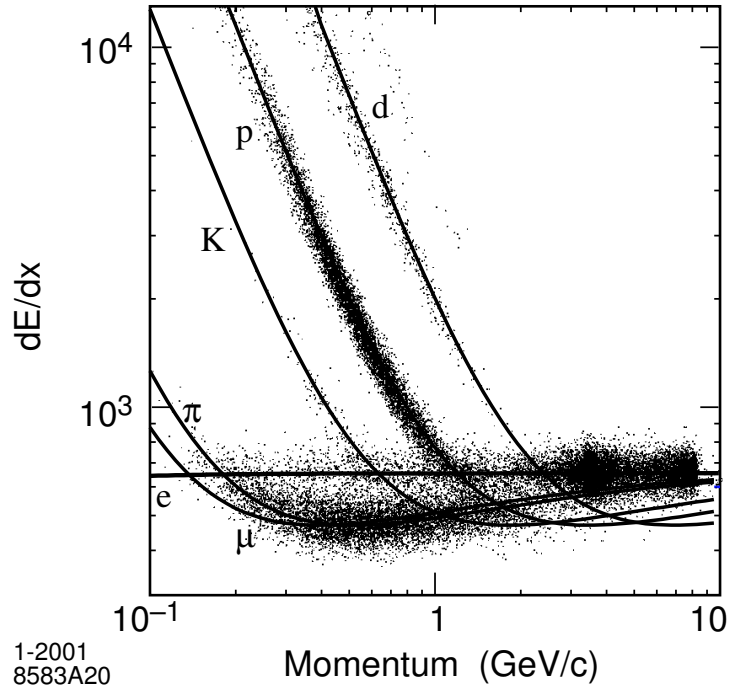
Figure 3.6: Drift chamber dE/dx measurements as a function of track momentum with superimposed Bethe-Bloch predictions.

3.5 The Cherenkov light detector

The DIRC is the main particle ID detector for charged particles with momenta over 0.7 GeV/c. It provides most of the K/π identification for the final state particles in this analysis.

DIRC design was motivated by the need to provide reliable K/π separation for charged particles with momenta larger than 0.7 GeV/c. Reliable identification of kaons with momenta of up to 2 GeV/c produced in $b \to c \to s$ cascade decays is essential for tagging the flavor of neutral B mesons in time-dependent analyses. The majority of final state mesons in charmless three-body decays have large momenta of up to ~ 4 GeV; good K/π separation is essential for assigning decay candidates to the correct final state. Similar to the drift chamber, the design requirements also include smallest possible amount of material in front of the EMC, smallest possible outer radius, fast signal response, and ability to operate in the presence of high backgrounds.

The DIRC (Fig. 3.7) is made of 144 quartz bars with refractive index $n = 1.473$ arranged in a 12-sided barrel. A charged particle traveling at a speed of $\beta c > c/n$ emits Cherenkov photons in a
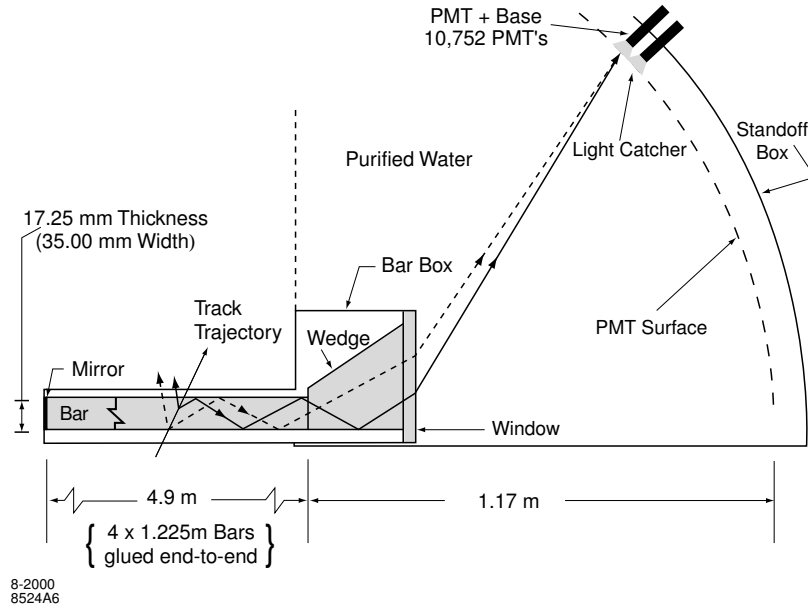
Figure 3.7: DIRC schematic.

cone with an opening Cherenkov angle given by $\cos\theta_c = 1/n\beta$. Some fraction of the photons are trapped inside the bar by total internal reflection and propagate towards the backward end of the bar, in the case of the photons initially propagating forward after being reflected by a mirror at the forward end of the bar. The photons are then allowed to expand in an expansion region filled with 6000 liters of purified water, whose refractive index matches well that of the quartz, toward an array of 10,752 photomultiplier tubes (PMTs) where the light is detected. A quartz wedge is used at the end of each bar to collimate the photons by reflecting the photons traveling inward toward the z axis outward and outward traveling photons at large angles inward, thus reducing the size of the region that needs to be instrumented. The image detected by the PMTs is a conical section from which the Cherenkov angle is inferred.

The arrival time of the signal is used to suppress background hits and to associate signal hits with charged tracks. Ambiguities introduced by photon reflections are resolved through the timing information and pattern matching.

The DIRC timing resolution and single photon Cherenkov angle resolution have been measured with di-muon events to be 1.7 ns and 10.2 mrad, respectively. K/π separation inferred from the
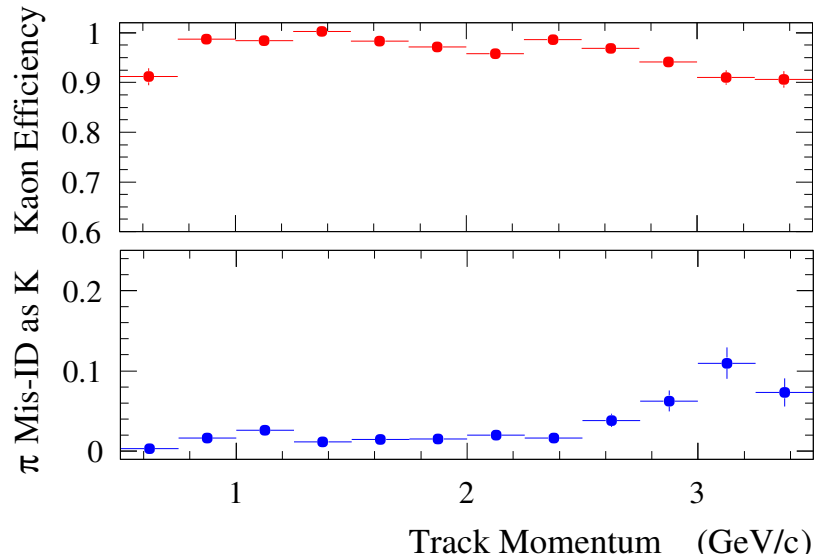
Figure 3.8: Kaon identification efficiency and pion-as-kaon misidentification rate as a function of track momentum.

di-muon measurements is better than four standard deviations up to 3 GeV/c track momentum.

Fig. 3.8 shows the efficiency of kaon identification and the pion-as-kaon misidentification rate as a function of track momentum determined from a control sample of $D \to K^{\pm}\pi^{\mp}$ decays.

3.6 The electromagnetic calorimeter

The EMC is a detector of electromagnetic showers produced by photons and electrons. It is not used extensively in this analysis, however, this system is critical for analyses that have π^0 and η mesons in the final state. The EMC also provides electron identification, which is critical for the tagging of neutral B mesons via semileptonic decays; the reconstruction of rare semileptonic decays of B and D mesons, and τ leptons; and the reconstruction of the leptonic decays of charmonium.

The EMC was designed to provide excellent resolution in energy and angle over a wide range of energies for incident particles. The lower bound of 20 MeV was set by the need for efficient reconstruction of low-energy π^0 and η produced in B decays; the higher bound by the need to measure the QED processes $e^+e^- \to e^+e^-(\gamma)$, and $e^+e^- \to \gamma\gamma$ needed for calibration and luminosity measurements.
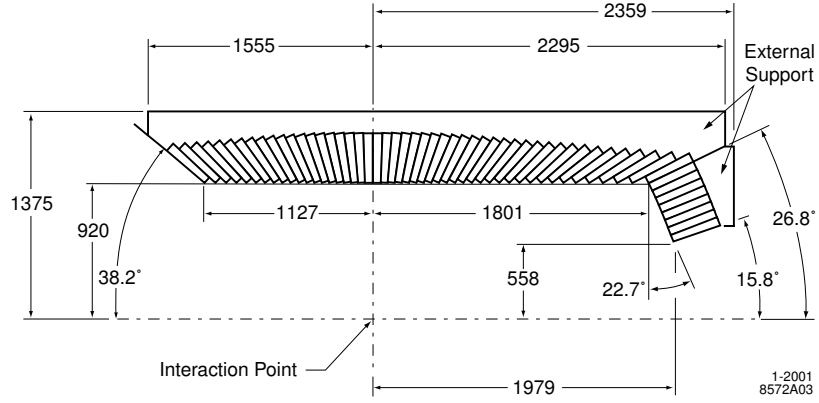
Figure 3.9: EMC schematic. The length unit is 1 mm.

The EMC is a hermetic total-absorption calorimeter which is composed of 6580 thallium-doped cesium iodide (CsI(Tl)) crystals, arranged projectively into a 5760 crystal barrel and an 820 crystal forward endcap (Fig. 3.9).

The crystal length varies from 16 radiation lengths (29.6 cm) in the backward direction to 17.5 radiation lengths in the forward direction of the higher energy electron beam. The face size of the crystals is about 5 cm × 5 cm, about the size of the Molière radius, providing a fine segmentation.

Electromagnetic showers produce scintillation light that propagates toward the back end of the crystal, possibly being reflected by diffuse reflective coating of the crystal wrapping. Each crystal is read out by two PIN diodes with quantum efficiency of 85%. The data from individual crystals are multiplexed and sent to a buffered pipeline. Sums of crystal blocks are formed and sent to the neutral hadware trigger logic. Upon receipt of a trigger, the data samples from the pipeline are read out and feature extraction is performed.

The response of individual crystals is calibrated using a light pulser system, the 6.13 MeV N^{16} gamma-ray line from an activated coolant fluid, and the Bhabha events. Neutral clusters are formed from sets of contiguous crystals. The energy and angular resolution of the calorimeter are parameterized as

$$\frac{\sigma_E}{E} = \frac{(2.32 \pm 0.30)\%}{\sqrt[4]{E(\,\mathrm{GeV})}} \oplus (1.85 \pm 0.12)\%,$$
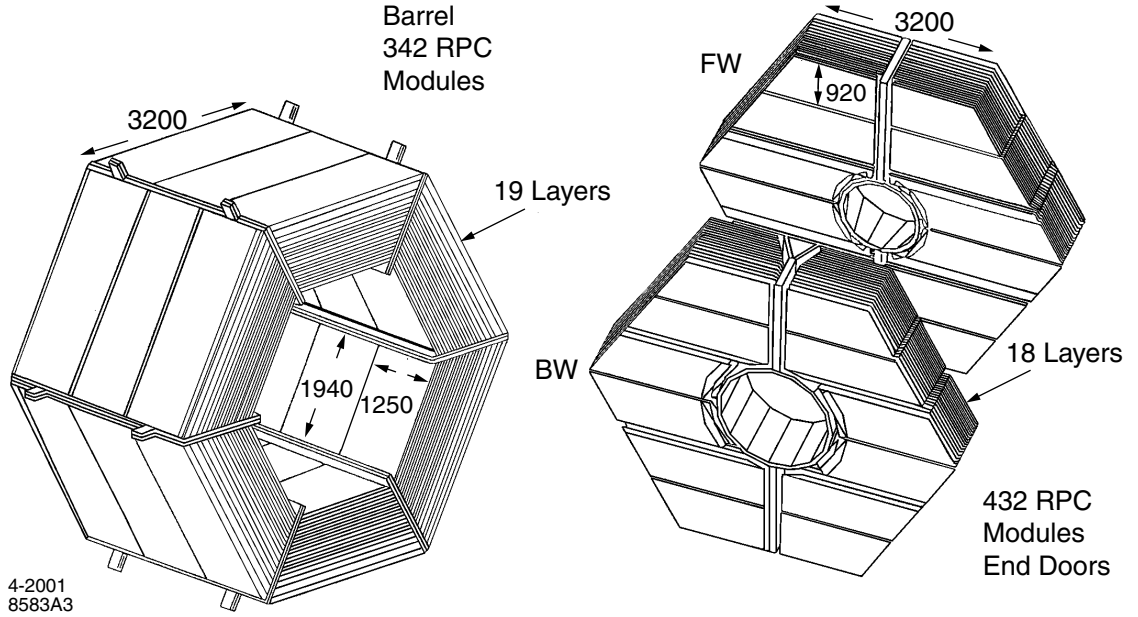
Figure 3.10: IFR schematic.

$$\sigma_\theta = \sigma_\phi = \left(\frac{3.87 \pm 0.07}{\sqrt{E(\,\text{GeV})}} + 0.00 \pm 0.04 \right) \text{ mrad},$$

respectively.

3.7   The instrumented flux return (IFR)

The IFR is the main detector for identifying muons and detecting neutral hadrons (K_L^0 and neutrons).

It also serves as a flux return of the 1.5 T magnetic field and a support structure for the rest of

the *BABAR* detector. The IFR information is not used extensively in this analysis, however, this

system is used for the tagging of neutral B mesons via semileptonic decays; the reconstruction of

rare semileptonic decays of B and D mesons, and τ leptons; the reconstruction of the leptonic decays

of charmonium; and analyses of exclusive final states with K_L^0 mesons.

The IFR is made up of resistive plate chambers (RPCs) interleaved between the steel layers of

the flux return. The detector arrangement is a hexagonal barrel with a forward and a backward

endcap as shown in Fig. 3.10.
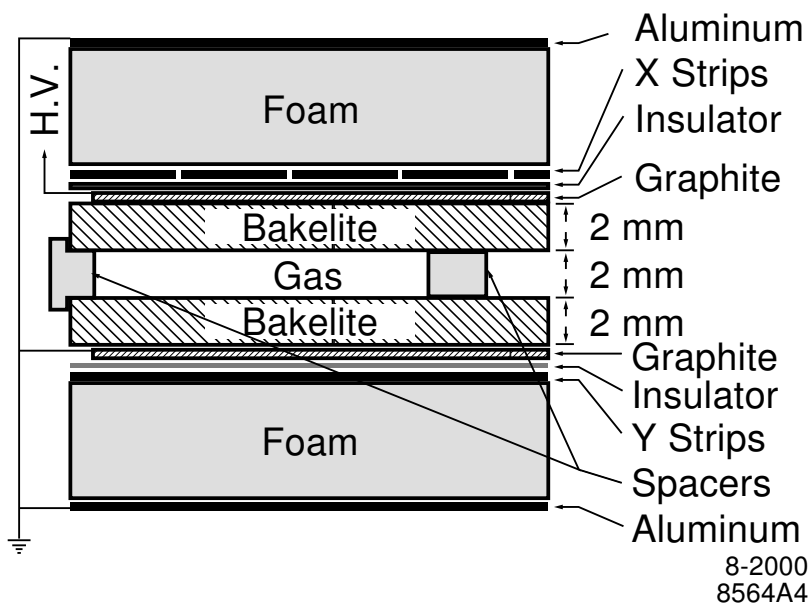
Figure 3.11: Cross section of a resistive plate chamber.

Individual RPCs (Fig. 3.11) detect the signal induced by streamers from ionizing particles on capacitive readout strips. An 8 kV voltage difference is applied to graphite-coated Bakelite electrodes. The gap is filled with a mixture of 57% argon, 39% freon-134a, and 4% isobutane. The aluminum readout strips are arranged orthogonally. The signals from the strips are read out and digitized. IFR hit information is also passed to the Level 1 Trigger.

The IFR system was comissioned and achieved muon efficiency of 90% and pion misidentification rate of less than 8% over the momentum range between 1.5 to 3.0 GeV/c. The muon detection efficiency degraded substantially during the Run 1–2 period dropping to around 65%. The problems may have been caused by the overheating of the RPCs, but the exact nature of the problem has never been conclusively established. The RPCs in the endcaps were replaced with limited streamer tubes (LSTs) during the post-Run 2 shutdown in summer 2002.

3.8 Trigger and data acquisition

The main design goal of the *BABAR* trigger is to select events of physics interest with a high and well-understood efficiency, while rejecting a large fraction of background events and keeping the total event logging rate under 120 Hz.

The trigger is implemented as a two-level system: a Level 1 hardware trigger and a Level 3 software trigger.

The hardware trigger receives input from the DCH and the EMC for efficient triggering on both charged tracks in the drift chamber and electromagnetic showers in the calorimeter. An input from the IFR is mainly used for diagnostic triggering on $\mu^+\mu^-$ and cosmic events.

For each subsystem there is a set of electronics boards that processes the input and emits trigger primitives. A DCH trigger (DCT) algorithm finds track segments based on the pattern of hits in the superlayers of the drift chamber. Track segments that can be linked together to reach superlayers 5 and 10 of the drift chamber form short and long DCT track primitives, respectively. A pattern of segments in the axial superlayers consistent with a track with $p_T > 0.8\,\mathrm{GeV}/c$ forms a high p_T track primitive. The EMC trigger (EMT) boards compute energy sums for predefined azimuthal segments of the calorimeter and emit a corresponding primitive if a predefined energy threshold is exceeded.

The DCT and EMT triggers provide highly efficient standalone triggering systems and can be used for detailed cross-validation studies. Azimuthal segments of DCT and EMT primitives are further shipped to the global trigger (GLT) where additional primitives are defined corresponding to azimuthally matched objects. Finally, if the primitives match any of a predefined set of configurations a Level 1 Trigger accept is issued. The typical output rate of the Level 1 trigger is 1 kHz.

A Level 1 Trigger accept decision causes all the detector subsystems to be read out into the data acquisition system that consists of special-purpose readout modules. The online dataflow system combines the data in individual modules into complete events that are made available to the Online Event Processing (OEP) system running on a farm of UNIX computers.

The OEP hosts a Level 3 software trigger that performs quick reconstruction of drift chamber helices and calorimeter clusters and selects events for logging. The output rate of the Level 3

trigger is limited to 120 Hz, which includes physics triggers, prescaled Bhabha event triggers for calibration, prescaled pass-through triggers, and diagnostic triggers. Selected events are sent to a logging manager and stored in temporary disk storage. Events from the disk storage are grouped into runs and are archived to tape storage where they become available for data quality checks, offline calibrations and eventual event reconstruction.

The OEP also hosts a real-time data quality monitoring system, and an online event display. Other subsystems of the DAQ implement detector control and calibrations.

Chapter 4

Event Selection

This chapter describes the event selection, whose main goal is to suppress copious backgrounds coming from the light-quark and charm $q\bar{q}$ continuum production, while retaining a high signal efficiency. The event selection proceeds in stages that follow closely the layout of the *BABAR* analysis environment.

4.1 Preselection

The first step of the analysis chain is event reconstruction. Five-parameter track candidate helices (Sec. 3.3) are fitted to the pattern of hits in the SVT and DCH. Track candidates are classified in the `ChargedTracks` category if they satisfy the following criteria:

- At least 12 hits in the DCH.

- Transverse momentum, $0.1 < p_T < 10 \, \mathrm{GeV}/c$.

- The point of closest approach coordinates satisfy $|z_0| < 10 \, \mathrm{cm}$ and $|d_0| < 1.5 \, \mathrm{cm}$.

If the number of DCH hits is greater than 20, the track candidate is upgraded to the `GoodTracksLoose` category.

The overall event shape is characterized using rotationally invariant Fox-Wolfram moments [42],

$$H_l \equiv \sum_{i,j} \frac{p_i p_j}{E_{vis}^2} P_l(\cos\theta_{ij}),$$

where the sum is over all charged and neutral decay products, p_i and p_j are the particle momenta, $P_l(\cos\theta_{ij})$ are the Legendre polynomials in the polar angle between particles i and j, and E_{vis} is the visible energy of the event. When operating at the $\Upsilon(4S)$ resonance, continuum $q\bar{q}$ events and $\Upsilon(4S)$ decays have very different event topologies. In the center-of-mass (CM) frame the momenta of the quarks in $e^+e^- \to q\bar{q}$ are high, whereas the B mesons in $\Upsilon(4S) \to B^+B^-$ are produced almost at rest. Accordingly, the decay products have a two-jet-like distribution for $q\bar{q}$ events, but are much more spherically distributed for $B\bar{B}$ events. The distribution of the ratio H_2/H_0 is highly peaked towards 1 for $q\bar{q}$ events, but it is flat for B decays. Events with at least three `GoodTracksLoose` tracks and $H_2/H_0 < 0.98$ are classified into the multihadron category. Essentially all of the produced $B\bar{B}$ pairs are preseved at this stage.

The second step is the *skim* stage, in which a loose selection of multihadron events for three-body charmless analyses is done. Track candidates from the `ChargedTracks` category are used to form $B^{\pm} \to K^{\pm}K^{\pm}K^{\mp}$ decay candidates.

Two nearly independent kinematic variables are used for identifying B decays [43, 44]. The first is

$$\Delta E \equiv E - \sqrt{s_0}/2,$$

the difference between the reconstructed B candidate energy and the beam energy measured in the CM frame. For signal events, the ΔE distribution peaks near zero with a resolution of $21\,\mathrm{MeV}/c$. The second is the energy-substituted mass:

$$m_{\mathrm{ES}} \equiv \sqrt{(s_0/2 + \boldsymbol{p}_0 \cdot \boldsymbol{p}_B)^2/E_0^2 - \boldsymbol{p}_B^2},$$

where $\boldsymbol{p}_B$ is the momentum of the B candidate and $(E_0, \boldsymbol{p}_0)$ is the four-momentum of the e^+e^- initial state, both in the laboratory frame. For signal events, the m_{ES} distribution peaks near the B mass with a resolution of $2.6\,\mathrm{MeV}/c^2$. Candidates with $|\Delta E| < 0.45\,\mathrm{GeV}$ and $|m_{\mathrm{ES}} - m_B| < 0.1\,\mathrm{GeV}/c^2$ are selected, where all possible combinations of K/π assignments of the three final state particles are considered.

Misreconstruction fractions for K⁺K⁺K⁻ simulated events.

Mean: 0.02

|ΔE|<0.1 5.27 < m_ES < 5.29
KaonLoose
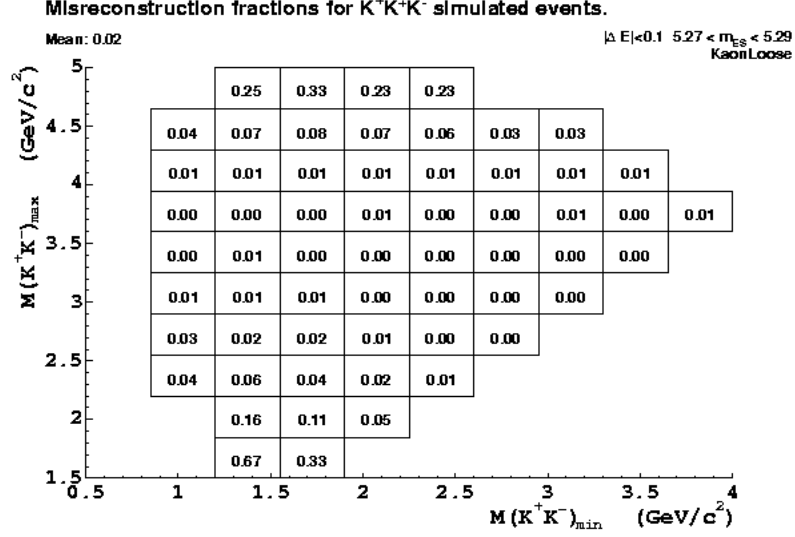
Figure 4.1: Average post-preselection fractions of misreconstructed simulated $B^{\pm} \to K^{\pm}K^{\pm}K^{\mp}$ signal events, shown for different regions of the di-kaon invariant mass scatter plot.

The third step is the analysis *n-tuple production* stage. N-tuples are two-dimensional tables, where each row represents an event and each column a specific analysis variable. The n-tuples are stored in `ROOT` [45] files and are shared between several analyses of three-body charmless B decays within *BABAR*. B candidates are formed again using track candidates from the `GoodTracksLoose` category. Candidates are required to have $E_{vis} < 20\,\text{GeV}$, $|m_{\text{ES}} - m_B| < 0.1\,\text{GeV}/c^2$, and $|\Delta E| < 0.15$ for data, or $|\Delta E| < 0.35\,\text{GeV}$ for simulated signal events. For a set of tracks the *thrust* is defined as

$$T \equiv \frac{\sum_i |\mathbf{p_i}\hat{\mathbf{T}}|}{\sum_i |\mathbf{p_i}|},$$

where the thrust axis $\hat{\mathbf{T}}$ is chosen such that T is maximized. In the CM frame, the distribution of the absolute value of the cosine of the angle between the thrust axis of the tracks forming the B candidate and the thrust axis of the remaining tracks, $|\cos\theta_T|$, is strongly peaked towards 1 for $q\bar{q}$ events. We require $|\cos\theta_T| < 0.95$.

We use a sample of 1.314 million Monte Carlo-simulated $B^{\pm} \to K^{\pm}K^{\pm}K^{\mp}$ events, generated with a uniform distribution over the phase space of the decay, to study the signal selection. The average preselection efficiency is evaluated to be 64.2%. Misreconstructed signal candidates are those
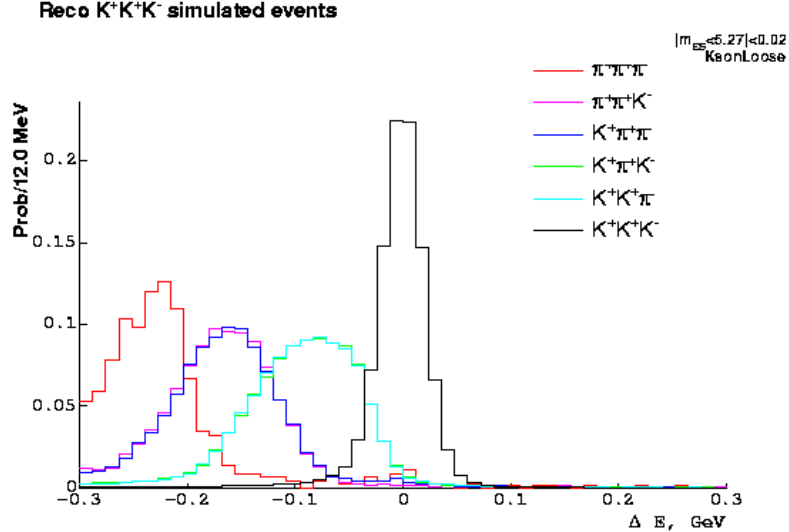
Figure 4.2: ΔE distributions for different K/π final state particle assignments for simulated signal $B^{\pm} \to K^{\pm}K^{\pm}K^{\mp}$ events.

for which one or more daughters used to form the B candidate are decay products of the recoil B. The fraction of misreconstructed events is on average 2% at this stage, but can be significantly larger in the corners of the decay phase space, where one of the B decay daughters is slow (Fig. 4.1).

To select a three-kaon final state we require that all the final state tracks are consistent with a kaon hypothesis using a likelihood-based kaon identification algorithm, which uses the information from the SVT, DCH, and the DIRC. Fig. 4.2 shows the ΔE distributions for properly reconstructed signal events satisfying $m_{\mathrm{ES}} \in (5.27, 5.29)\,\mathrm{GeV}/c^2$ for different K/π assignement of the final state particles. The distribution is shifted toward negative values when kaon-as-pion misidentification occurs and to positive values when pion-as-kaon misidentification occurs. Requiring events to be within a narrow ΔE signal window helps eliminate a significant fraction of events with particle misidentification.

We study the three-kaon final state selection efficiency using correctly reconstructed simulated signal events with $|\Delta E| < 0.1\,\mathrm{GeV}$ and $m_{\mathrm{ES}} \in (5.27, 5.29)\,\mathrm{GeV}/c^2$. The average particle identification efficiency for kaons is 94%, giving an average signal efficiency of 82% for $B^{\pm} \to K^{\pm}K^{\pm}K^{\mp}$, with little dependence on the di-kaon invariant mass values (Fig. 4.3). The average pion-as-kaon misidentification probability is 6%. Because of particle misidentification, there can be cross-feed

Fractions of events with correct PID
Simulated K⁺K⁺K⁻ events. KaonLoose selector.
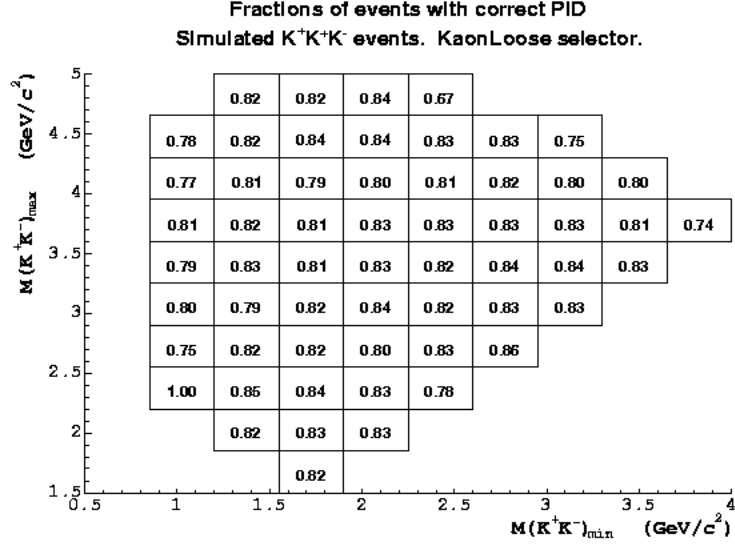
Figure 4.3: Average fractions of simulated $B^{\pm} \to K^{\pm}K^{\pm}K^{\mp}$ events, for which all final state kaons have been correctly identified, shown for different regions of the di-kaon invariant mass scatter plot.

between different charmless three-body final states, typically due to one particle being misidentified. The $B^{\pm} \to K^{\pm}\pi^{\pm}K^{\mp}$ mode is Cabibbo-suppressed and the upper limit of Ref. [16] implies that its cross-feed contribution to the $K^{\pm}K^{\pm}K^{\mp}$ final state is no more than 1.3%.

We suppress leptonic backgrounds using likelihood-based electron and muon identification algorithms. The average fraction of correctly reconstructed signal events with all final state particles identified as kaons by the kaon-identification algorithm, for which at least one of the daughter particles is identified as an electron or a muon is 0.2% and 1.8%, respectively. We reject B candidates if any daughter track is identified as an electron, or if two daughter tracks are identified as muons.

After the preselection is done, a kinematic fit is applied to the selected candidates, with the invariant mass of the three daughter particles constrained to the mass of the decaying $B^{\pm}$ meson. The kinematic fit improves the resolution of the di-kaon invariant masses for signal events, and forces the selected candidates to lie within the kinematic boundary of the $B^{\pm} \to K^{\pm}K^{\pm}K^{\mp}$ Dalitz plot.

Fig. 4.4 shows the average candidate multiplicity in different regions of the di-kaon invariant mass scatter plot after requiring $|\Delta E| < 0.1 \, \text{GeV}/c$ and $m_{\text{ES}} \in (5.27, 5.29) \, \text{GeV}/c^2$. The overall average candidate multiplicity is 1.04, but can be larger in the corners of the plot, where one of the daughter tracks is slow and can be easily substituted by a track from the rest of the event. If there
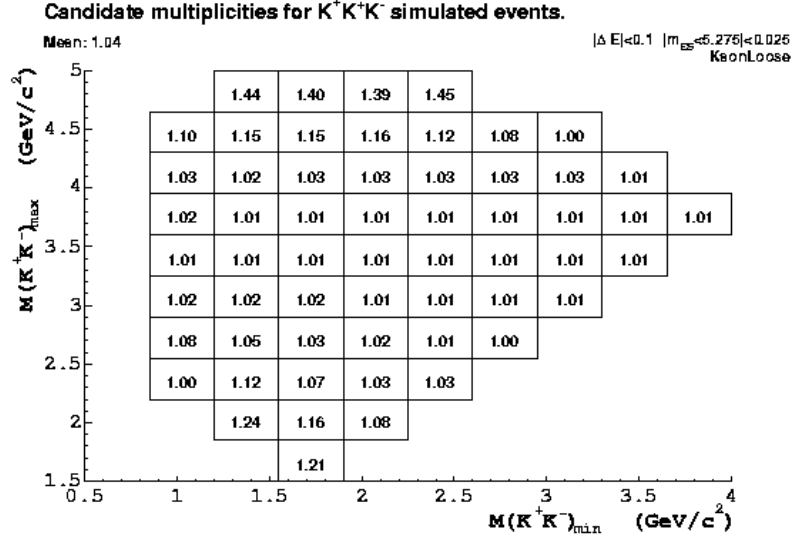
Figure 4.4: Post-preselection average candidate multiplicity for simulated $B^{\pm} \to K^{\pm}K^{\pm}K^{\mp}$ events, shown for different regions of the di-kaon invariant mass scatter plot.

are multiple candidates after all selection criteria are applied, a candidate is chosen at random.

4.2   Continuum background suppression

Continuum $q\bar{q}$ events are the dominant source of background. We study these events using two data samples:

- The off-peak data taken 40 MeV below the $\Upsilon(4S)$ resonance, for which we require $m_{ES} \in (5.18, 5.27) \, \text{GeV}/c^2$ and $|\Delta E| < 0.15 \, \text{GeV}$. Because of the lower beam energies, the m_{ES} distribution for off-peak events is shifted down by 20 MeV with respect to the distribution for on-peak events. Events in the off-peak dataset consist mostly of $q\bar{q}$ continuum events. The total number of off-peak events is small, since the integrated off-peak luminosity for the BABAR Runs 1–4 data period is only $21.6 \, \text{fb}^{-1}$, much smaller than $210.6 \, \text{fb}^{-1}$ collected on-peak.

- A sample of on-peak data events selected in the region $m_{ES} \in (5.20, 5.25) \, \text{GeV}/c^2$, $|\Delta E| < 0.15 \, \text{GeV}$. This m_{ES} sideband sample contains mostly $q\bar{q}$ events and a small fraction of candidates due to misreconstructed B decays. The sideband sample size is large, but an extrapolation into the signal region is required.
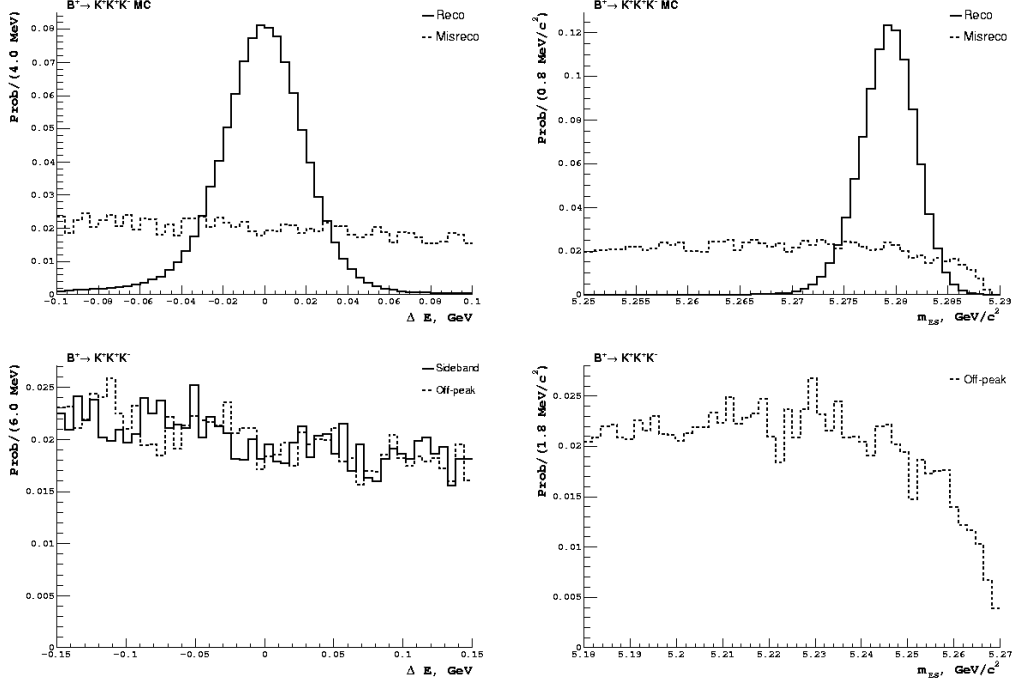
Figure 4.5: ΔE and m_{ES} distributions for simulated signal events (top), and sideband and off-peak events (bottom).

In both cases, a random candidate is chosen when multiple candidates are present.

Fig. 4.5 shows the m_{ES} and ΔE distributions for simulated signal events with $|\Delta E| < 0.1\,\mathrm{GeV}$ and $m_{\mathrm{ES}} \in (5.27, 5.29)\,\mathrm{GeV}/c^2$, sideband events with $|\Delta E| < 0.15\,\mathrm{GeV}$ and $m_{\mathrm{ES}} \in (5.20, 5.25)\,\mathrm{GeV}/c^2$, and off-peak events with $|\Delta E| < 0.15\,\mathrm{GeV}$ and $m_{\mathrm{ES}} \in (5.18, 5.27)\,\mathrm{GeV}/c^2$. Fig. 4.6 shows the di-kaon invariant mass scatter plots and their projections for sideband and off-peak events. The $q\bar{q}$ backgrounds are especially prominent near the boundary of the scatter plot and there is a significant contribution from continuum production of the $\phi(1020)$ resonance.

Following a previous charmless *BABAR* analysis [28], we further suppress the continuum background using the output of a multi-layer perceptron neural network with the following four inputs computed in the CM frame: the cosine of the angle between the direction of the B candidate and the beam direction, $\cos\theta_{B,z}$; the absolute value of the cosine of the angle between the candidate thrust axis and the beam direction, $|\cos\theta_{T,z}|$; and momentum-weighted sums over tracks and neutral clusters not belonging to the candidate, $L_0 = \sum_i p_i$ and $L_2 = \sum_i p_i \cos^2\theta_i$, where the angles θ_i
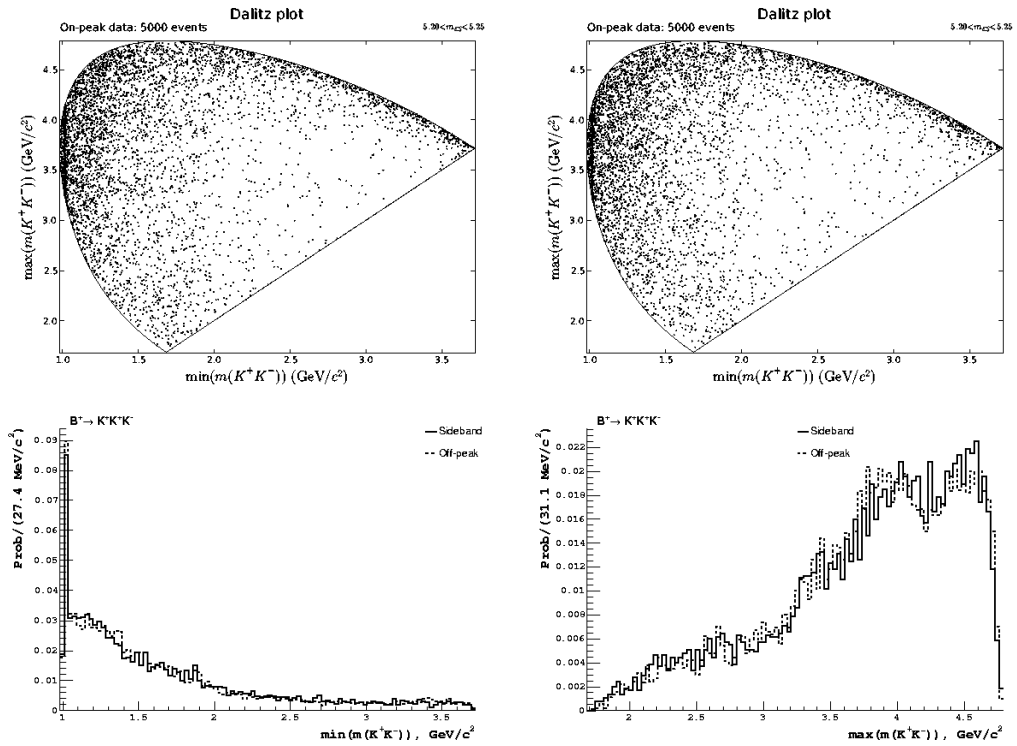
Figure 4.6: Di-kaon invariant mass scatter plots for sideband (top left) and off-peak events (top right). Invariant mass projections for sideband (bottom left) and off-peak events (bottom right).

are measured with respect to the candidate thrust axis.

Fig. 4.7 shows the distributions of the four neural network input variables for simulated signal events with $|\Delta E| < 0.1\,\mathrm{GeV}$ and $m_{\mathrm{ES}} \in (5.27, 5.29)\,\mathrm{GeV}/c^2$, sideband events with $|\Delta E| < 0.15\,\mathrm{GeV}$ and $m_{\mathrm{ES}} \in (5.20, 5.25)\,\mathrm{GeV}/c^2$, and off-peak events with $|\Delta E| < 0.15\,\mathrm{GeV}$ and $m_{\mathrm{ES}} \in (5.18, 5.27)\,\mathrm{GeV}/c^2$

The neural network has a four-neuron input layer, two hidden layers with 3 and 2 neurons, and two output neurons. The response of each neuron in layer $L + 1$ is modeled as

$$x^{L+1} = \frac{1 - \exp(-w_0 - \sum_i w_i x_i^L)}{1 + \exp(-w_0 - \sum_i w_i x_i^L)},$$

where the sum runs over all neurons in the preceding layer. The weights w are optimized to maximize the separatation between signal and background in a training sample consisting of 10^4 correctly reconstructed simulated signal events with $m_{\mathrm{ES}} \in (5.25, 5.29)\,\mathrm{GeV}/c^2$, $|\Delta E| < 0.1\,\mathrm{GeV}$ for the signal category and 10^4 sideband events with $m_{\mathrm{ES}} \in (5.20, 5.25)\,\mathrm{GeV}/c^2$, $|\Delta E| < 0.15\,\mathrm{GeV}$ for the background category. The response of the neural network, mapped on the interval $(-1, +1)$, is shown in Fig. 4.8.

We require $\Delta E \in (\Delta E_{\min}, \Delta E_{\max})$, and $\mathrm{NN} > \mathrm{NN}_0$, where the interval $(\Delta E_{\min}, \Delta E_{\max})$ and NN_0 are found via joint optimization. Different $(\Delta E_{\min}, \Delta E_{\max})$ intervals and NN_0 values are tried in the range $(-0.1\,\mathrm{GeV}, 0.15\,\mathrm{GeV})$ with a $10\,\mathrm{MeV}$ step and in the range $(-1, 1)$ with a 0.05 step, respectively. For each point, we evaluate the signal efficiency, ϵ, using properly reconstructed simulated signal events in a region $m_{\mathrm{ES}} \in (5.274, 5.284)\,\mathrm{GeV}/c^2$, an interval about two standard deviations wide around the m_{ES} signal peak. We also use the events from the $m_{\mathrm{ES}} \in (5.20, 5.25)\,\mathrm{GeV}/c^2$ kinematic sideband to evaluate the fraction of eliminated background events, f.

The pairs of values (ϵ, f) thus determined form a scatter plot whose boundary (Fig. 4.9) corresponds to the set of possible optimum selection choices. Making a direct connection between a pair of values $(\epsilon, f(\epsilon))$ and the eventual sensitivity of the amplitude fit is difficult. We choose to maximize
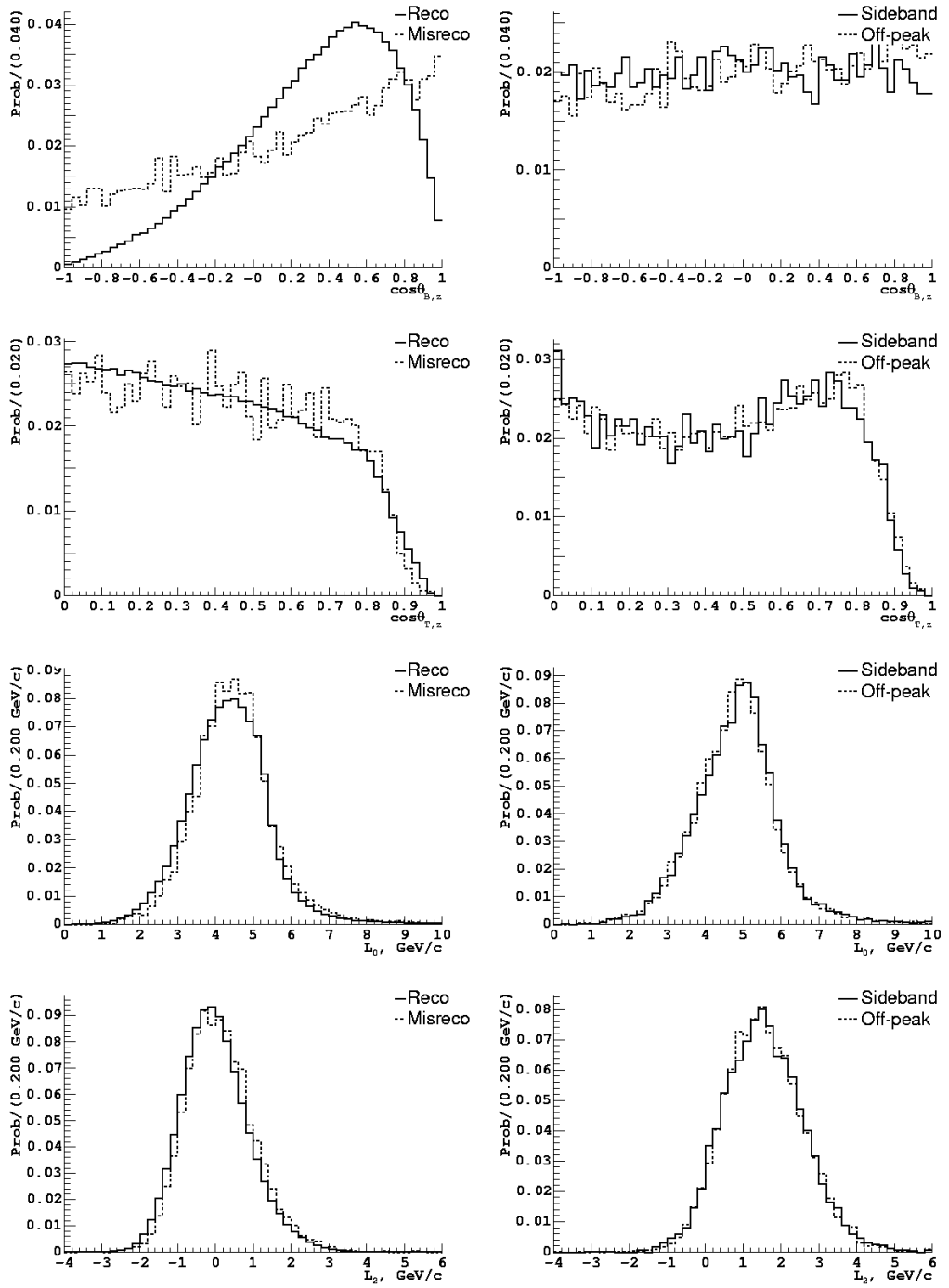
Figure 4.7: Distributions of the neural network input variables for simulated signal events (left), and sideband and off-peak events (right).
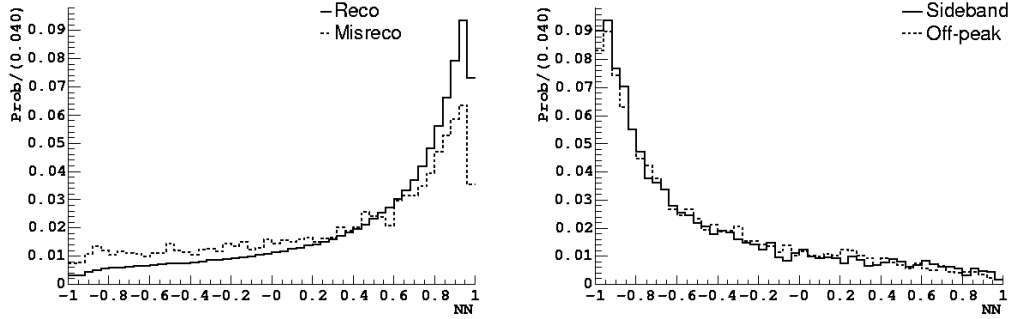
Figure 4.8: Distributions of neural network output for simulated signal events (left), and sideband and off-peak events (right).
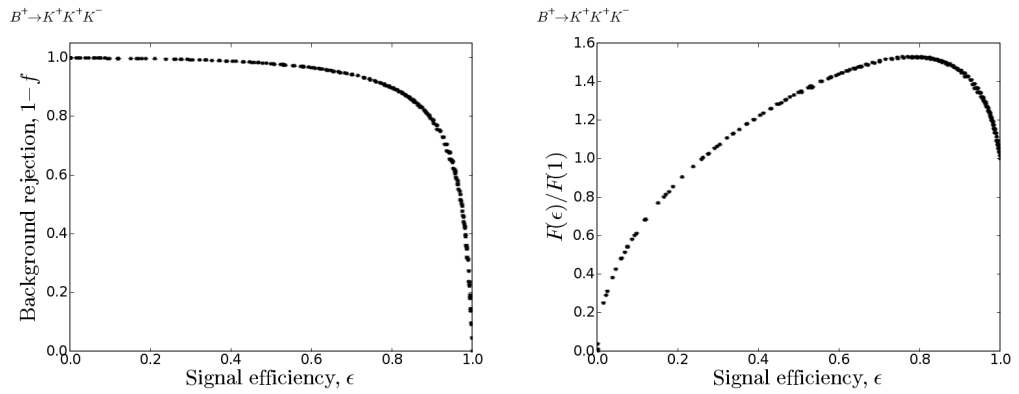
Figure 4.9: Optimum selection boundary in the (ϵ, f) plane (left) and the normalized figure-of-merit of Eq. (4.1) as a function of the selection efficiency for points on the optimum selection boundary (right).

the figure-of-merit often used for selection optimization in branching fraction measurements:

$$F(\epsilon) = \frac{S}{\sqrt{S+B}} = \frac{\epsilon S_0}{\sqrt{\epsilon S_0 + (1 - f(\epsilon))B_0}}, \tag{4.1}$$

where S_0 (S) and B_0 (B) are the expected numbers of signal and background events in the signal region *before* (*after*) applying the final selection. We estimate $S_0 = 2.5 \times 10^3$, using the preselection efficiency and the *BABAR* measurement of the total branching fraction [16], and $B_0 = 7.6 \times 10^3$ by extrapolating the number of events from the $m_{\mathrm{ES}} \in (5.20, 5.25)\,\mathrm{GeV}/c^2$, $\Delta E \in (-0.1, 0.15)\,\mathrm{GeV}$ sideband, giving $F(1) = 24.9$. The figure-of-merit is maximized at $F(\epsilon)/F(1) = 1.6$ for $(\epsilon, f) = (0.81, 0.916)$, corresponding to $\Delta E \in (-40, 40)\,\mathrm{MeV}$ and $\mathrm{NN} > -0.2$.

4.3   Continuum background extrapolation

Figure 4.10 shows the m_{ES} distribution of the 9870 events selected in the region $m_{\mathrm{ES}} \in (5.20, 5.29)$, fitted with a sum of a Gaussian distribution and a background function having a probability density:

$$p(x) \propto x\sqrt{1 - x^2} \exp\left(-\xi(1 - x^2)\right),$$

where $x = 2m_{\mathrm{ES}}/\sqrt{s_0}$ and ξ is a shape parameter [46]. The fit gives 2394 ± 63 events in the Gaussian peak, having the mean, $m_0 = 5.280 \pm 0.001\,\mathrm{GeV}/c^2$, and a standard deviation, $\sigma = 2.64 \pm 0.07\,\mathrm{MeV}/c^2$. We define a signal region (SR) with $m_{\mathrm{ES}} \in (5.27, 5.29)\,\mathrm{GeV}/c^2$ and a sideband (SB) with $m_{\mathrm{ES}} \in (5.20, 5.25)\,\mathrm{GeV}/c^2$. The ratio of the integrals of the background function over the signal region and the sideband yields an extrapolation coefficient,

$$R_{q\bar{q}} \equiv \frac{\int_{\mathrm{SR}} p(x)dx}{\int_{\mathrm{SB}} p(x)dx},$$

shown as a function of the shape parameter ξ in Fig. 4.11. The fit gives $\xi = 21.1 \pm 1.5$; the corresponding extrapolation coefficient is $R_{q\bar{q}} = 0.231 \pm 0.007$. We use it to estimate the expected number of $q\bar{q}$ background events in the signal region, $n_{q\bar{q}}^{\mathrm{SR}} = R_{q\bar{q}}(n^{\mathrm{SB}} - n_{B\bar{B}}^{\mathrm{SB}}) = 977 \pm 34$, where
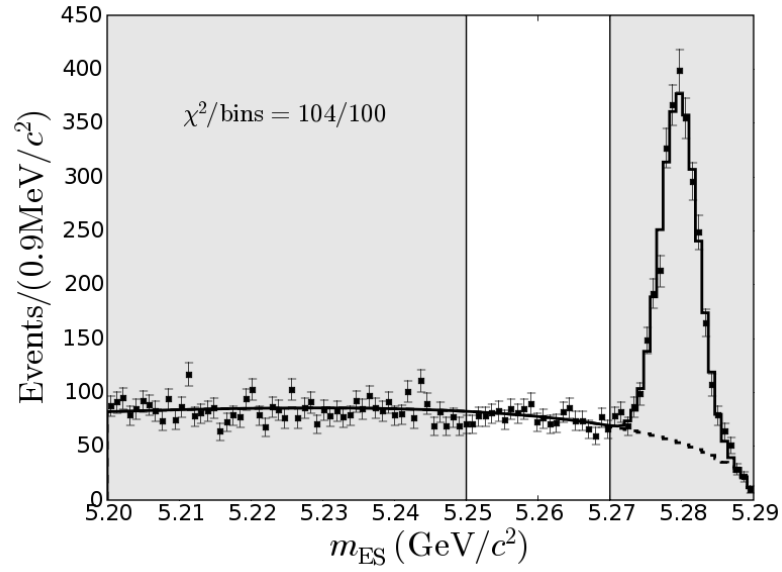
Figure 4.10: The m_{ES} distribution of the 9870 selected events. The solid histogram shows a fit with a sum of a Gaussian distribution ($m_0 = 5.280 \pm 0.001\,\mathrm{GeV}/c^2$, $\sigma = 2.64 \pm 0.07\,\mathrm{MeV}/c^2$, $N = 2394 \pm 63$) and an ARGUS background function (dashed histogram, $\xi = 21.1 \pm 1.5$). The shaded regions correspond to the signal region and the m_{ES} sideband defined in the text.
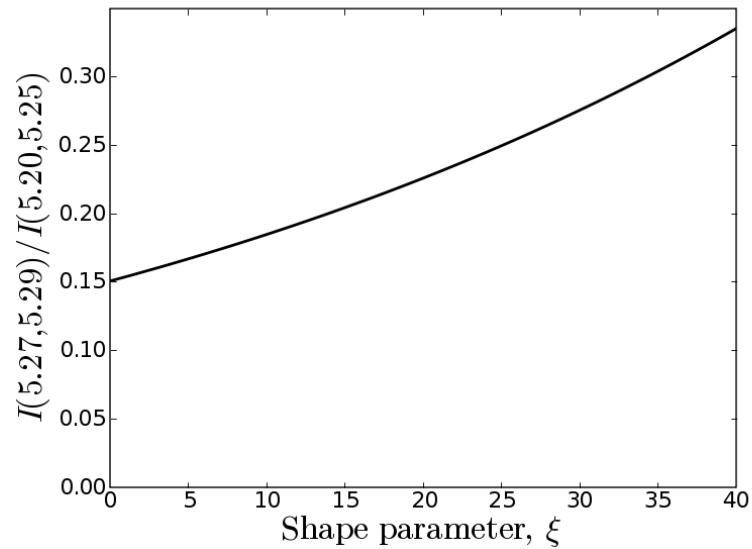
Figure 4.11: The $q\bar{q}$ backgrounds extrapolation factor $R_{q\bar{q}}$ as a function of the background function shape parameter ξ.
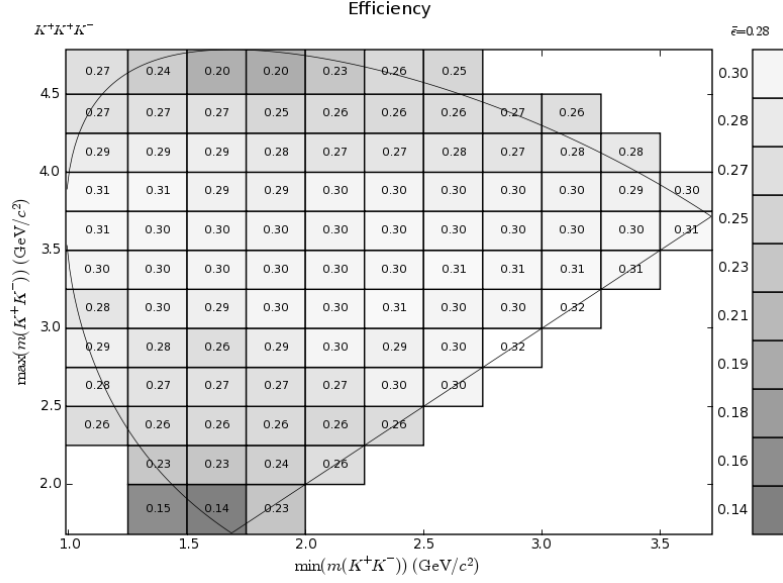
Figure 4.12: Efficiency for properly reconstructed signal $B^{\pm} \rightarrow K^{\pm}K^{\pm}K^{\mp}$ events in $0.25 \times 0.25\,\mathrm{GeV}^2/c^4$ bins across the di-kaon invariant mass scatter plot.

$n^{\mathrm{SB}} = 4659$ is the number of events in the sideband, from which we subtract the number of non-signal $B\bar{B}$ background events, $n^{\mathrm{SB}}_{B\bar{B}} = 431 \pm 19$, estimated using a large number of simulated exclusive B decays as described in Chapter 5.

4.4 Signal efficiency

We determine the final signal selection efficiency using properly reconstructed simulated signal events generated with a uniform phase-space density. The efficiency is adjusted to account for the observed descrepancies between the tracking and particle identification efficiencies in data and simulation, by applying correction factors derived from data control samples [47, 48]. The efficiency distribution in $0.25 \times 0.25\,\mathrm{GeV}^2/c^4$ bins across the di-kaon invariant mass scatter plot is shown in Fig. 4.12. It is rather uniform, except near the corners of the plot, where the momentum of one of the particles is small.

Misreconstructed events are effectively an undesirable background. Fortunately, their contribution is very small. We determine the overall fraction of misreconstructed events to be $1.38 \pm 0.02\%$,

with only $0.34 \pm 0.02\%$ for the signal m_{ES} bin.

Chapter 5

Modeling of B Backgrounds

Backgrounds coming from non-signal B decays are studied using Monte Carlo-simulated events. Constructing an adequate model of B backgrounds is a difficult task because many modes can contribute. We first look at simulated events for a number of individual B decay modes to get an understanding of which background modes are important. Our final model of B backgrounds is based on a generic cocktail of exclusive B decays.

5.1   Study of individual B background modes

Tables 5.1 and 5.2 show the exclusive B^+B^- and $B^0\overline{B}^0$ background modes considered, their branching fractions taken from Ref. [14], the number of events expected in a sample of 226.0×10^6 $B\overline{B}$ decays, and the sizes of the simulated datasets. We make reasonable assumptions for the values of the branching fractions where there are no measurements or where only upper limits are available. Tables 5.3 and 5.4 summarize the branching fractions used.

In the following, the final state particles likely to be used to form a B candidate that mimics the signal final state are set in boldface, and $\boldsymbol{h}$ stands for either a kaon or a pion. We consider the following sources of backgrounds:

- Charmless two-body decays, such as $B^0 \to \boldsymbol{h}^+\boldsymbol{h}^-$. Combining the two final state mesons with a charged track from the rest of the event can mimic a three-body final state. In the case of $B^\pm \to K_S^0\boldsymbol{h}^\pm$, $K_S^0 \to \boldsymbol{\pi}^+\boldsymbol{\pi}^-$ there is a direct contribution to the $\boldsymbol{h}^\pm\boldsymbol{\pi}^\pm\boldsymbol{\pi}^\mp$ charmless

Table 5.1: Exclusive $B^\pm$ decay modes considered (charge conjugation implied), their branching fractions, the number of events expected in a sample of 226.0×10^6 $B\overline{B}$ decays, and the sizes of simulated datasets. The first column (SP-Mode) is the *BABAR* simulation production unique mode identifier.

SP-Mode	Decay	$\mathcal{B}$	Expected	Generated
991	$B^+ \to K^0\pi^+, K^0 \to K_S^0, K_S^0 \to \pi^+\pi^-$	$(7.52 \pm 0.50) \times 10^{-6}$	1700	219000
1049	$B^+ \to K^+\overline{K}^0, \overline{K}^0 \to K_S^0, K_S^0 \to \pi^+\pi^-$	$(3.45 \pm 3.45) \times 10^{-7}$	80	182000
1215	$B^+ \to \overline{D}^0\pi^+, \overline{D}^0 \to K^+\pi^-$	$(1.87 \pm 0.12) \times 10^{-4}$	42000	216000
1216	$B^+ \to \overline{D}^0\pi^+, \overline{D}^0 \to K^+K^-$	$(1.91 \pm 0.14) \times 10^{-5}$	4300	114000
1217	$B^+ \to \overline{D}^0\pi^+, \overline{D}^0 \to \pi^+\pi^-$	$(6.78 \pm 0.54) \times 10^{-6}$	1500	182000
1453	$B^+ \to K_1(1270)^+\gamma$	$(1.00 \pm 1.00) \times 10^{-5}$	2000	234000
1454	$B^+ \to K_1(1400)^+\gamma$	$(1.00 \pm 1.00) \times 10^{-5}$	2000	234000
1508	$B^+ \to \eta'K^+, \eta' \to \rho^0\gamma$	$(2.30 \pm 0.23) \times 10^{-5}$	5200	145000
1509	$B^+ \to \eta'\pi^+, \eta' \to \rho^0\gamma$	$(1.03 \pm 1.07) \times 10^{-6}$	200	146000
1542	$B^+ \to \eta K^{*+}, \eta \to \pi^+\pi^-\pi^0, K^{*+} \to K^+\pi^0$	$(1.96 \pm 0.34) \times 10^{-6}$	440	121000
1765	$B^+ \to K_2^*(1430)^+\gamma$	$(1.40 \pm 0.40) \times 10^{-5}$	3200	182000
1940	$B^+ \to \overline{D}^{*0}e^+\overline{\nu}_e, \overline{D}^{*0} \to \overline{D}^0\gamma, \overline{D}^0 \to K^+\pi^-\pi^0$	$(3.27 \pm 0.75) \times 10^{-3}$	700000	283000
1970	$B^+ \to K^*(1410)^+\gamma$	$(1.00 \pm 1.00) \times 10^{-5}$	2000	290000
1972	$B^+ \to K^*(1680)^+\gamma$	$(1.00 \pm 1.00) \times 10^{-5}$	2000	290000
2355	$B^+ \to K^{*+}\rho^0 \parallel, K^{*+} \to K^+\pi^0$	$(1.83 \pm 0.67) \times 10^{-6}$	400	201000
2356	$B^+ \to K^{*+}\rho^0 \perp, K^{*+} \to K^+\pi^0$	$(1.83 \pm 0.67) \times 10^{-6}$	400	178000
2390	$B^+ \to \rho^+\rho^0$	$(2.60 \pm 0.60) \times 10^{-5}$	6000	352000
2392	$B^+ \to K^{*+}K^{*0} \parallel, K^{*+} \to K^+\pi^0, K^{*0} \to K^+\pi^-$	$(3.89 \pm 3.89) \times 10^{-6}$	900	126000
2393	$B^+ \to K^{*+}K^{*0} \perp, K^{*+} \to K^+\pi^0, K^{*0} \to K^+\pi^-$	$(3.89 \pm 3.89) \times 10^{-6}$	900	126000
2394	$B^+ \to K^{*+}K^{*0} \parallel, K^{*+} \to K^0\pi^+, K^0 \to K_S^0, K^{*0} \to K^+\pi^-$	$(3.89 \pm 3.89) \times 10^{-6}$	900	122000
2395	$B^+ \to K^{*+}K^{*0} \perp, K^{*+} \to K^0\pi^+, K^0 \to K_S^0, K^{*0} \to K^+\pi^-$	$(3.89 \pm 3.89) \times 10^{-6}$	900	121000
2421	$B^+ \to \overline{D}^{*0}\pi^+, \overline{D}^{*0} \to \overline{D}^0\pi^0, \overline{D}^0 \to K^+\pi^-$	$(1.08 \pm 0.17) \times 10^{-4}$	25000	172000
2422	$B^+ \to \overline{D}^0\pi^+, \overline{D}^0 \to K^+\pi^-\pi^0$	$(6.48 \pm 0.77) \times 10^{-4}$	150000	249000
2423	$B^+ \to \overline{D}^{*0}\pi^+, \overline{D}^{*0} \to \overline{D}^0\pi^0, \overline{D}^0 \to K^+\pi^-\pi^0$	$(3.76 \pm 0.79) \times 10^{-4}$	80000	232000
2432	$B^+ \to \overline{D}^0K^+, \overline{D}^0 \to K^+\pi^-\pi^0$	$(4.88 \pm 1.16) \times 10^{-5}$	11000	134000
2435	$B^+ \to \overline{D}^0K^+, \overline{D}^0 \to K^+\pi^-$	$(1.41 \pm 0.26) \times 10^{-5}$	3200	362000
2436	$B^+ \to \overline{D}^0\rho^+, \overline{D}^0 \to K^+\pi^-$	$(5.11 \pm 0.81) \times 10^{-4}$	120000	108494
2441	$B^+ \to \overline{D}^0\rho^+, \overline{D}^0 \to K^+\pi^-\pi^0$	$(1.77 \pm 0.37) \times 10^{-3}$	400000	294000
2626	$B^+ \to \overline{D}^{*0}K^+, \overline{D}^{*0} \to \overline{D}^0\gamma, \overline{D}^0 \to K^+\pi^-$	$(5.23 \pm 1.97) \times 10^{-6}$	1200	259500
2627	$B^+ \to \overline{D}^{*0}K^+, \overline{D}^{*0} \to \overline{D}^0\gamma, \overline{D}^0 \to K^+\pi^-\pi^0$	$(1.81 \pm 0.78) \times 10^{-5}$	4000	42000
2628	$B^+ \to \overline{D}^{*0}\pi^+, \overline{D}^{*0} \to \overline{D}^0\gamma, \overline{D}^0 \to K^+\pi^-\pi^0$	$(2.31 \pm 0.55) \times 10^{-4}$	50000	239000
2629	$B^+ \to \overline{D}^{*0}\pi^+, \overline{D}^{*0} \to \overline{D}^0\gamma, \overline{D}^0 \to K^+\pi^-$	$(6.68 \pm 1.25) \times 10^{-5}$	15000	192500
3018	$B^+ \to \overline{D}^0K^+, \overline{D}^0 \to K^+K^-$	$(1.44 \pm 0.28) \times 10^{-6}$	330	250000
3019	$B^+ \to \overline{D}^0K^+, \overline{D}^0 \to \pi^+\pi^-$	$(5.11 \pm 1.01) \times 10^{-7}$	120	20000
3135	$B^+ \to K^{*+}\gamma$	$(4.03 \pm 0.26) \times 10^{-5}$	9100	436000
3172	$B^+ \to \overline{D}^{*0}K^+, \overline{D}^{*0} \to \overline{D}^0\gamma, \overline{D}^0 \to K^+K^-$	$(5.35 \pm 2.06) \times 10^{-7}$	120	250000
3173	$B^+ \to \overline{D}^{*0}K^+, \overline{D}^{*0} \to \overline{D}^0\gamma, \overline{D}^0 \to \pi^+\pi^-$	$(1.89 \pm 0.74) \times 10^{-7}$	40	30000
3174	$B^+ \to \overline{D}^{*0}\pi^+, \overline{D}^{*0} \to \overline{D}^0\gamma, \overline{D}^0 \to K^+K^-$	$(6.84 \pm 1.32) \times 10^{-6}$	1500	147000
3175	$B^+ \to \overline{D}^{*0}\pi^+, \overline{D}^{*0} \to \overline{D}^0\gamma, \overline{D}^0 \to \pi^+\pi^-$	$(2.42 \pm 0.48) \times 10^{-6}$	500	30000
4731	$B^+ \to \overline{D}^0e^+\overline{\nu}_e, \overline{D}^0 \to K^+\pi^-$	$(8.19 \pm 1.03) \times 10^{-4}$	190000	294000
4732	$B^+ \to \overline{D}^0e^+\overline{\nu}_e, \overline{D}^0 \to K^+\pi^-\pi^0$	$(2.84 \pm 0.51) \times 10^{-3}$	600000	294000
4733	$B^+ \to \overline{D}^0\mu^+\overline{\nu}_\mu, \overline{D}^0 \to K^+\pi^-$	$(8.19 \pm 1.03) \times 10^{-4}$	190000	294000
4734	$B^+ \to \overline{D}^0\mu^+\overline{\nu}_\mu, \overline{D}^0 \to K^+\pi^-\pi^0$	$(2.84 \pm 0.51) \times 10^{-3}$	600000	292000
4735	$B^+ \to \overline{D}^{*0}e^+\overline{\nu}_e, \overline{D}^{*0} \to \overline{D}^0\pi^0, \overline{D}^0 \to K^+\pi^-$	$(1.53 \pm 0.23) \times 10^{-3}$	350000	294000
4736	$B^+ \to \overline{D}^{*0}e^+\overline{\nu}_e, \overline{D}^{*0} \to \overline{D}^0\pi^0, \overline{D}^0 \to K^+\pi^-\pi^0$	$(5.31 \pm 1.06) \times 10^{-3}$	1200000	294000
4737	$B^+ \to \overline{D}^{*0}\mu^+\overline{\nu}_\mu, \overline{D}^{*0} \to \overline{D}^0\pi^0, \overline{D}^0 \to K^+\pi^-$	$(1.53 \pm 0.23) \times 10^{-3}$	350000	294000
4738	$B^+ \to \overline{D}^{*0}\mu^+\overline{\nu}_\mu, \overline{D}^{*0} \to \overline{D}^0\pi^0, \overline{D}^0 \to K^+\pi^-\pi^0$	$(5.31 \pm 1.06) \times 10^{-3}$	1200000	294000
4750	$B^+ \to \overline{D}^{*0}e^+\overline{\nu}_e, \overline{D}^{*0} \to \overline{D}^0\gamma, \overline{D}^0 \to K^+\pi^-$	$(9.44 \pm 1.67) \times 10^{-4}$	210000	289000
4751	$B^+ \to \overline{D}^{*0}\mu^+\overline{\nu}_\mu, \overline{D}^{*0} \to \overline{D}^0\gamma, \overline{D}^0 \to K^+\pi^-$	$(9.44 \pm 1.67) \times 10^{-4}$	210000	288000
4752	$B^+ \to \overline{D}^{*0}\mu^+\overline{\nu}_\mu, \overline{D}^{*0} \to \overline{D}^0\gamma, \overline{D}^0 \to K^+\pi^-\pi^0$	$(3.27 \pm 0.75) \times 10^{-3}$	700000	294000

Table 5.2: Exclusive B^0 decay modes considered, their branching fractions, the number of events expected in a sample of 226.0×10^6 $B\overline{B}$ decays, and the sizes of simulated datasets.

SP-Mode	Decay	$\mathcal{B}$	Expected	Generated
1028	$B^0 \to K^+\pi^-$	$(1.82 \pm 0.08) \times 10^{-5}$	4100	1873500
1042	$B^0 \to \pi^+\pi^-$	$(4.60 \pm 0.40) \times 10^{-6}$	1040	2595000
1123	$B^0 \to D^{*-}\pi^+, D^{*-} \to \overline{D}^0\pi^-$	$(1.87 \pm 0.16) \times 10^{-3}$	420000	4226000
1159	$B^0 \to D^-\rho^+$	$(7.70 \pm 1.30) \times 10^{-3}$	1700000	112000
1452	$B^0 \to K_1(1270)^0\gamma$	$(1.00 \pm 1.00) \times 10^{-5}$	2000	234000
1455	$B^0 \to K_1(1400)^0\gamma$	$(1.00 \pm 1.00) \times 10^{-5}$	2000	234000
1568	$B^0 \to D^{*-}\rho^+, D^{*-} \to \overline{D}^0\pi^-$	$(4.60 \pm 0.64) \times 10^{-3}$	1000000	1052000
1766	$B^0 \to K_2^*(1430)^0\gamma$	$(1.24 \pm 0.24) \times 10^{-5}$	2800	184000
1971	$B^0 \to K^*(1410)^0\gamma$	$(1.00 \pm 1.00) \times 10^{-5}$	2000	288000
1973	$B^0 \to K^*(1680)^0\gamma$	$(1.00 \pm 1.00) \times 10^{-5}$	2000	286000
2128	$B^0 \to \overline{D}^{*0}\gamma, \overline{D}^{*0} \to \overline{D}^0\gamma, \overline{D}^0 \to K^+\pi^-$	$(3.63 \pm 3.99) \times 10^{-7}$	80	183000
2359	$B^0 \to K^{*0}\rho^0 \parallel, K^{*0} \to K^+\pi^-$	$(3.34 \pm 3.34) \times 10^{-6}$	800	202000
2360	$B^0 \to K^{*0}\rho^0 \perp, K^{*0} \to K^+\pi^-$	$(3.34 \pm 3.34) \times 10^{-6}$	800	182000
2396	$B^0 \to \rho^0\rho^0$	$(1.00 \pm 1.00) \times 10^{-6}$	200	203000
2398	$B^0 \to K^{*0}\overline{K}^{*0}, K^{*0} \to K^+\pi^-, \overline{K}^{*0} \to K^-\pi^+$	$(4.45 \pm 4.45) \times 10^{-6}$	1000	122000
2498	$B^0 \to \rho^+\rho^-$	$(2.60 \pm 0.60) \times 10^{-5}$	6000	4383000
2979	$B^0 \to \overline{D}^0\pi^0, \overline{D}^0 \to K^+\pi^-$	$(1.11 \pm 0.13) \times 10^{-5}$	2500	154000
2981	$B^0 \to \overline{D}^0\pi^0, \overline{D}^0 \to K^+\pi^-\pi^0$	$(3.84 \pm 0.66) \times 10^{-5}$	9000	70000
2982	$B^0 \to \overline{D}^{*0}\pi^0, \overline{D}^{*0} \to \overline{D}^0\pi^0/\gamma, \overline{D}^0 \to K^+\pi^-$	$(1.03 \pm 0.21) \times 10^{-5}$	2300	140000
2984	$B^0 \to \overline{D}^{*0}\pi^0, \overline{D}^{*0} \to \overline{D}^0\pi^0/\gamma, \overline{D}^0 \to K^+\pi^-\pi^0$	$(3.56 \pm 0.93) \times 10^{-5}$	8000	140000
2992	$B^0 \to \overline{D}^0\rho^0, \overline{D}^0 \to K^+\pi^-$	$(1.10 \pm 0.45) \times 10^{-5}$	2000	70000
2995	$B^0 \to \overline{D}^{*0}\rho^0, \overline{D}^{*0} \to \overline{D}^0\pi^0/\gamma, \overline{D}^0 \to K^+\pi^-$	$(9.53 \pm 9.75) \times 10^{-6}$	2000	140000
3134	$B^0 \to K^{*0}\gamma$	$(4.01 \pm 0.20) \times 10^{-5}$	9100	392000
4209	$B^0 \to K^{*+}\rho^-, K^{*+} \to K^+\pi^0$	$(3.66 \pm 1.33) \times 10^{-6}$	800	12000
4635	$B^0 \to D^-K^+, D^- \to \pi^-\pi^0$	$(2.66 \pm 1.24) \times 10^{-7}$	60	295000

three-body final state.

- Charmless decays with a photon in the final state, such as $B^\pm \to K^{*\pm}\gamma$. Some of these can produce a charmless three-body final state with an extra photon, e.g., $B^\pm \to \eta' \boldsymbol{K^\pm}$, $\eta' \to \rho^0\gamma$, $\rho^0 \to \boldsymbol{\pi^+\pi^-}$.

- Charmless four-body decays, such as $B^\pm \to K^{*\pm}K^{*0}, K^{*\pm} \to \boldsymbol{K^\pm}\pi^0, K^{*0} \to \boldsymbol{K^\pm\pi^\mp}$ can mimic a charmless three-body final state when the π^0 is soft.

- Semileptonic decays, e.g., $B^+ \to \overline{D}^0\ell^+\overline{\nu}_\ell, \overline{D}^0 \to \boldsymbol{K^+\pi^-}$, can mimic a charmless three-body final state due to lepton-as-kaon misidentification. Lepton vetoes described in Section 4.1 suppress these backgrounds.

- Numerous multibody decays with charm proceeding through intermediate D^0 or D^{*0} mesons. These modes can be an important source of backgrounds because of their high branching fractions.

The expected numbers of events in the signal region due to individual non-three-body $B^\pm$ and

Table 5.3: $B^{\pm}$ decay branching fractions from Ref. [14] (charge conjugation implied), the values used in the generation of the *BABAR* generic cocktail of $B^{\pm}$ decays, and the branching fractions used in the study of individual B background modes.

B^+ decays	Mode	$\mathcal{B}$ PDG	$\mathcal{B}$ cocktail	$\mathcal{B}$ used
Γ_2	$B^+ \to \overline{D}^0 e^+ \overline{\nu}_e$	$(2.15 \pm 0.22)\%$	2.10%	$(2.15 \pm 0.22)\%$
Γ_2	$B^+ \to \overline{D}^0 \mu^+ \overline{\nu}_\mu$	$(2.15 \pm 0.22)\%$	2.10%	$(2.15 \pm 0.22)\%$
Γ_3	$B^+ \to \overline{D}^{*0} e^+ \overline{\nu}_e$	$(6.50 \pm 0.50)\%$	5.60%	$(6.50 \pm 0.50)\%$
Γ_3	$B^+ \to \overline{D}^{*0} \mu^+ \overline{\nu}_\mu$	$(6.50 \pm 0.50)\%$	5.60%	$(6.50 \pm 0.50)\%$
Γ_{28}	$B^+ \to \overline{D}^0 \pi^+$	$(4.91 \pm 0.21) \times 10^{-3}$	5.30×10^{-3}	$(4.91 \pm 0.21) \times 10^{-3}$
Γ_{31}	$B^+ \to \overline{D}^0 \rho^+$	$(1.34 \pm 0.18)\%$	1.34%	$(1.34 \pm 0.18)\%$
Γ_{32}	$B^+ \to \overline{D}^0 K^+$	$(3.70 \pm 0.60) \times 10^{-4}$	4.40×10^{-4}	$(3.70 \pm 0.60) \times 10^{-4}$
Γ_{52}	$B^+ \to \overline{D}^{*0} \pi^+$	$(4.60 \pm 0.40) \times 10^{-3}$	4.60×10^{-3}	$(4.60 \pm 0.40) \times 10^{-3}$
Γ_{54}	$B^+ \to \overline{D}^{*0} \rho^+$	$(9.80 \pm 1.70) \times 10^{-3}$	1.55%	$(9.80 \pm 1.70) \times 10^{-3}$
Γ_{55}	$B^+ \to \overline{D}^{*0} K^+$	$(3.60 \pm 1.00) \times 10^{-4}$	$-$	$(3.60 \pm 1.00) \times 10^{-4}$
Γ_{152}	$B^+ \to K^0 \pi^+$	$(2.18 \pm 0.14) \times 10^{-5}$	1.80×10^{-5}	$(2.18 \pm 0.14) \times 10^{-5}$
Γ_{154}	$B^+ \to \eta' K^+$	$(7.80 \pm 0.50) \times 10^{-5}$	7.50×10^{-5}	$(7.80 \pm 0.50) \times 10^{-5}$
Γ_{157}	$B^+ \to \eta K^{*+}$	$(2.60 \pm 0.40) \times 10^{-5}$	2.60×10^{-5}	$(2.60 \pm 0.40) \times 10^{-5}$
$-$	$B^+ \to K^{*0} \rho^+$	$-$	1.00×10^{-5}	$(1.00 \pm 1.00) \times 10^{-5}$
Γ_{175}	$B^+ \to K^{*+} \rho^0$	$(1.10 \pm 0.40) \times 10^{-5}$	1.00×10^{-5}	$(1.10 \pm 0.40) \times 10^{-5}$
Γ_{176}	$B^+ \to K^{*+} K^{*0}$	$< 7.10 \times 10^{-5}$ CL $= 90\%$	1.00×10^{-6}	$(3.50 \pm 3.50) \times 10^{-5}$
Γ_{179}	$B^+ \to K^+ \overline{K}^0$	$< 2.50 \times 10^{-6}$ CL $= 90\%$	1.40×10^{-6}	$(1.00 \pm 1.00) \times 10^{-6}$
Γ_{197}	$B^+ \to K^{*+} \gamma$	$(4.03 \pm 0.26) \times 10^{-5}$	4.50×10^{-5}	$(4.03 \pm 0.26) \times 10^{-5}$
Γ_{198}	$B^+ \to K_1(1270)^+ \gamma$	$< 9.90 \times 10^{-5}$ CL $= 90\%$	$-$	$(1.00 \pm 1.00) \times 10^{-5}$
Γ_{204}	$B^+ \to K_1(1400)^+ \gamma$	$< 5.00 \times 10^{-5}$ CL $= 90\%$	$-$	$(1.00 \pm 1.00) \times 10^{-5}$
$-$	$B^+ \to K^*(1410)^+ \gamma$	$-$	$-$	$(1.00 \pm 1.00) \times 10^{-5}$
Γ_{205}	$B^+ \to K_2^*(1430)^+ \gamma$	$(1.40 \pm 0.40) \times 10^{-5}$	$-$	$(1.40 \pm 0.40) \times 10^{-5}$
Γ_{206}	$B^+ \to K^*(1680)^+ \gamma$	$< 1.90 \times 10^{-3}$ CL $= 90\%$	$-$	$(1.00 \pm 1.00) \times 10^{-5}$
Γ_{219}	$B^+ \to \rho^+ \rho^0$	$(2.60 \pm 0.60) \times 10^{-5}$	1.50×10^{-5}	$(2.60 \pm 0.60) \times 10^{-5}$
Γ_{225}	$B^+ \to \eta' \pi^+$	$< 4.50 \times 10^{-6}$ CL $= 90\%$	2.00×10^{-6}	$(3.50 \pm 3.50) \times 10^{-6}$

Table 5.4: B^0 decay branching fractions from Ref. [14], the values used in the generation of the *BABAR* generic cocktail of B^0 decays, and the branching fractions used in the study of individual B background modes.

B^0 decays	Mode	$\mathcal{B}$ PDG	$\mathcal{B}$ cocktail	$\mathcal{B}$ used
Γ_{20}	$B^0 \to D^-\rho^+$	$(7.70 \pm 1.30) \times 10^{-3}$	6.80×10^{-3}	$(7.70 \pm 1.30) \times 10^{-3}$
Γ_{23}	$B^0 \to D^-K^+$	$(2.00 \pm 0.60) \times 10^{-4}$	2.00×10^{-4}	$(2.00 \pm 0.60) \times 10^{-4}$
Γ_{27}	$B^0 \to D^{*-}\pi^+$	$(2.76 \pm 0.21) \times 10^{-3}$	2.70×10^{-3}	$(2.76 \pm 0.21) \times 10^{-3}$
Γ_{33}	$B^0 \to D^{*-}\rho^+$	$(6.80 \pm 0.90) \times 10^{-3}$	6.80×10^{-3}	$(6.80 \pm 0.90) \times 10^{-3}$
Γ_{84}	$B^0 \to \overline{D}^0\pi^0$	$(2.91 \pm 0.28) \times 10^{-4}$	2.40×10^{-4}	$(2.91 \pm 0.28) \times 10^{-4}$
Γ_{85}	$B^0 \to \overline{D}^0\rho^0$	$(2.90 \pm 1.10) \times 10^{-4}$	2.50×10^{-4}	$(2.90 \pm 1.10) \times 10^{-4}$
Γ_{90}	$B^0 \to \overline{D}^{*0}\gamma$	$< 5.00 \times 10^{-5}$ CL = 90%	$-$	$(2.50 \pm 2.50) \times 10^{-5}$
Γ_{91}	$B^0 \to \overline{D}^{*0}\pi^0$	$(2.70 \pm 0.50) \times 10^{-4}$	2.90×10^{-4}	$(2.70 \pm 0.50) \times 10^{-4}$
Γ_{92}	$B^0 \to \overline{D}^{*0}\rho^0$	$< 5.10 \times 10^{-4}$ CL = 90%	2.50×10^{-4}	$(2.50 \pm 2.50) \times 10^{-4}$
Γ_{143}	$B^0 \to K^+\pi^-$	$(1.82 \pm 0.08) \times 10^{-5}$	1.80×10^{-5}	$(1.82 \pm 0.08) \times 10^{-5}$
Γ_{158}	$B^0 \to K^+\rho^-$	$(8.50 \pm 2.80) \times 10^{-6}$	1.50×10^{-5}	$(8.50 \pm 2.80) \times 10^{-6}$
$-$	$B^0 \to K^{*+}\rho^-$	$-$	2.00×10^{-5}	$(1.10 \pm 0.40) \times 10^{-5}$
Γ_{174}	$B^0 \to K^{*0}\rho^0$	$< 3.40 \times 10^{-5}$ CL = 90%	8.00×10^{-7}	$(1.00 \pm 1.00) \times 10^{-5}$
Γ_{180}	$B^0 \to K^{*0}\overline{K}^{*0}$	$< 2.20 \times 10^{-5}$ CL = 90%	1.00×10^{-6}	$(1.00 \pm 1.00) \times 10^{-5}$
Γ_{188}	$B^0 \to K^{*0}\gamma$	$(4.01 \pm 0.20) \times 10^{-5}$	4.50×10^{-5}	$(4.01 \pm 0.20) \times 10^{-5}$
Γ_{193}	$B^0 \to K_1(1270)^0\gamma$	$< 7.00 \times 10^{-3}$ CL = 90%	$-$	$(1.00 \pm 1.00) \times 10^{-5}$
Γ_{194}	$B^0 \to K_1(1400)^0\gamma$	$< 4.30 \times 10^{-3}$ CL = 90%	$-$	$(1.00 \pm 1.00) \times 10^{-5}$
$-$	$B^0 \to K^*(1410)^0\gamma$	$-$	$-$	$(1.00 \pm 1.00) \times 10^{-5}$
Γ_{195}	$B^0 \to K_2^*(1430)^0\gamma$	$(1.24 \pm 0.24) \times 10^{-5}$	$-$	$(1.24 \pm 0.24) \times 10^{-5}$
Γ_{196}	$B^0 \to K^*(1680)^0\gamma$	$< 2.00 \times 10^{-3}$ CL = 90%	$-$	$(1.00 \pm 1.00) \times 10^{-5}$
Γ_{202}	$B^0 \to \pi^+\pi^-$	$(4.60 \pm 0.40) \times 10^{-6}$	4.70×10^{-6}	$(4.60 \pm 0.40) \times 10^{-6}$
Γ_{226}	$B^0 \to \rho^0\rho^0$	$< 2.10 \times 10^{-6}$ CL = 90%	2.00×10^{-6}	$(1.00 \pm 1.00) \times 10^{-6}$
Γ_{230}	$B^0 \to \rho^+\rho^-$	$(3.00 \pm 0.60) \times 10^{-5}$	3.00×10^{-5}	$(2.60 \pm 0.60) \times 10^{-5}$

Table 5.5: Expected contributions to the final $B^{\pm} \to K^{\pm}K^{\pm}K^{\mp}$ data sample for exclusive $B^{\pm}$ decay modes.

Mode	Decay	Expected
2436	$B^+ \to \overline{D}^0 \rho^+, \overline{D}^0 \to K^+\pi^-$	17 ± 5
2422	$B^+ \to \overline{D}^0 \pi^+, \overline{D}^0 \to K^+\pi^-\pi^0$	12 ± 3
2432	$B^+ \to \overline{D}^0 K^+, \overline{D}^0 \to K^+\pi^-\pi^0$	5 ± 1
4738	$B^+ \to \overline{D}^{*0}\mu^+\overline{\nu}_\mu, \overline{D}^{*0} \to \overline{D}^0\pi^0, \overline{D}^0 \to K^+\pi^-\pi^0$	4 ± 4
2629	$B^+ \to \overline{D}^{*0}\pi^+, \overline{D}^{*0} \to \overline{D}^0\gamma, \overline{D}^0 \to K^+\pi^-$	4 ± 1
2421	$B^+ \to \overline{D}^{*0}\pi^+, \overline{D}^{*0} \to \overline{D}^0\pi^0, \overline{D}^0 \to K^+\pi^-$	3 ± 1
2626	$B^+ \to \overline{D}^{*0}K^+, \overline{D}^{*0} \to \overline{D}^0\gamma, \overline{D}^0 \to K^+\pi^-$	2 ± 1
4732	$B^+ \to \overline{D}^0 e^+\overline{\nu}_e, \overline{D}^0 \to K^+\pi^-\pi^0$	2 ± 2
3174	$B^+ \to \overline{D}^{*0}\pi^+, \overline{D}^{*0} \to \overline{D}^0\gamma, \overline{D}^0 \to K^+K^-$	1 ± 0
2423	$B^+ \to \overline{D}^{*0}\pi^+, \overline{D}^{*0} \to \overline{D}^0\pi^0, \overline{D}^0 \to K^+\pi^-\pi^0$	1 ± 1
2441	$B^+ \to \overline{D}^0 \rho^+, \overline{D}^0 \to K^+\pi^-\pi^0$	1 ± 1
4733	$B^+ \to \overline{D}^0 \mu^+\overline{\nu}_\mu, \overline{D}^0 \to K^+\pi^-$	1 ± 1
2392	$B^+ \to K^{*+}K^{*0} \parallel, K^{*+} \to K^+\pi^0, K^{*0} \to K^+\pi^-$	1 ± 1
–	Non-three-body total	59.3 ± 8.1

Table 5.6: Expected contributions to the final $B^{\pm} \to K^{\pm}K^{\pm}K^{\mp}$ data sample for exclusive B^0 decay modes.

Mode	Decay	Expected
1123	$B^0 \to D^{*-}\pi^+, D^{*-} \to \overline{D}^0\pi^-$	4 ± 1
2398	$B^0 \to K^{*0}\overline{K}^{*0}, K^{*0} \to K^+\pi^-, \overline{K}^{*0} \to K^-\pi^+$	1 ± 1
–	Non-three-body total	6.7 ± 1.9

B^0 background modes after all selection requirements have been applied are shown in Tables 5.5–5.6.

5.2 Background cocktail study

The background model used in this analysis is based on a comprehensive cocktail of B^+B^- and $B^0\overline{B}^0$ generic decays composed according to the best available knowledge of the branching fractions and the decay dynamics of individual modes. Samples of 536.3 million B^+B^- and 541.3 million $B^0\overline{B}^0$ decays were used, about 4.8 times the number of $B\overline{B}$ pairs in the experimental dataset used in this analysis.

The original cocktail contains signal events coming from three-body charmless decays, possibly with one or more photons radiated from the charged quark lines in the Feynman diagrams. These events are removed by requiring that the final state of the generated decay be different from

Table 5.7: Expected contributions to the final $B^{\pm} \to K^{\pm}K^{\pm}K^{\mp}$ data sample for exclusive $B^{\pm}$ three-body decay modes with an intermediate D^0.

Mode	Decay	Expected
3018	$B^+ \to \overline{D}^0 K^+, \overline{D}^0 \to K^+ K^-$	87 ± 17
1216	$B^+ \to \overline{D}^0 \pi^+, \overline{D}^0 \to K^+ K^-$	37 ± 3
2435	$B^+ \to \overline{D}^0 K^+, \overline{D}^0 \to K^+ \pi^-$	13 ± 2
1215	$B^+ \to \overline{D}^0 \pi^+, \overline{D}^0 \to K^+ \pi^-$	3 ± 1
–	Charm three-body total	139.8 ± 17.2

$h^{\pm}h^{\pm}h^{\mp} + n\gamma$.

The di-kaon invariant mass scatter plots of events from the generic cocktail of $B^{\pm}$ and B^0 decays selected in the signal region are shown in Fig. 5.1. After adjusting by a luminosity scaling factor, the expected background contributions are 96 ± 6 events for the B^+B^- decays and 34 ± 4 for $B^0\overline{B}^0$ decays.

Three-body charmed decays $B^{\pm} \to \overline{D}^0 h^{\pm}, \overline{D}^0 \to h^+h^-$ contribute to the same final state as the signal charmless modes, but because of the long lifetime of the intermediate D^0 meson they can be added incoherently in the background model. These decays are initially in the original cocktail, but are removed by the requirement that the final state be different from $h^{\pm}h^{\pm}h^{\mp} + n\gamma$. They are studied individually as described in Section 5.1 and their contributions (Table 5.7) are added back to the final B background model. The same procedure is used for several modes with an $h^+h^+h^- + \gamma$ final state, such as $B^{\pm} \to \overline{D}^{*0} h^{\pm}, \overline{D}^{*0} \to \overline{D}^0 \gamma, \overline{D}^0 \to h^+h^-$.

We estimate the total expected number of $B\overline{B}$ background events in the signal region to be $n_{B\overline{B}}^{\mathrm{SR}} = 276 \pm 20$, with $B^{\pm} \to DK^{\pm}$ decays giving the largest contribution.
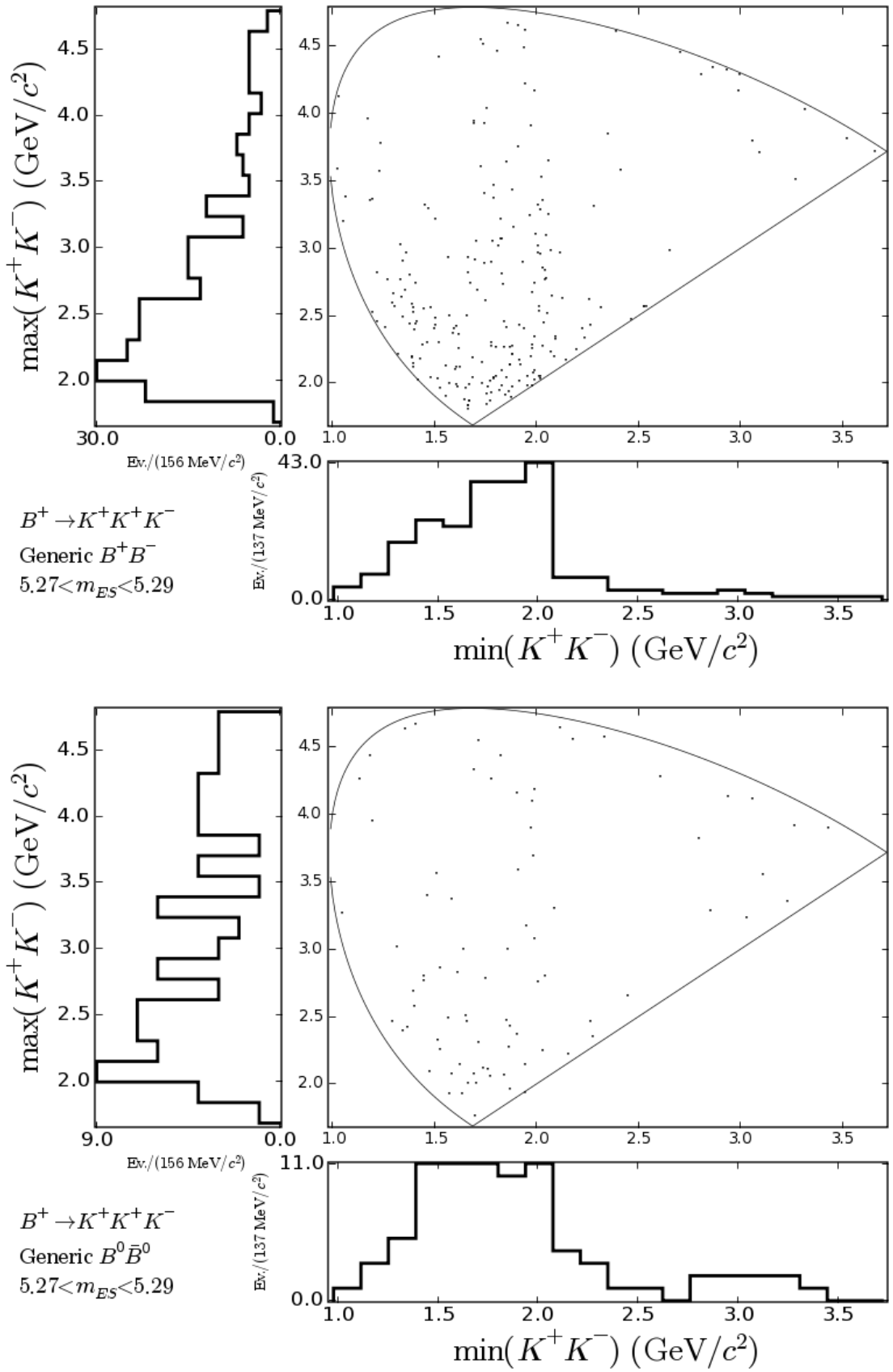
Figure 5.1: Di-kaon invariant mass scatter plots of events from a simulated cocktail of generic B^+B^- (top) and $B^0\overline{B}^0$ (bottom) decays selected in the signal region.

Chapter 6

Dalitz Plot Analysis Formalism

In this chapter we briefly review the three-body kinematics, the partial-wave analysis method, the isobar model, and amplitude parameterizations. The review is short; more detailed discussions can be found elsewhere [14, 49].

6.1 Three-body decay kinematics

For a decay of a particle having mass M into three particles having masses m_1, m_2, m_3, the three two-body invariant mass combinations (Mandelstam variables): $s_{12} \equiv m_{12}^2$, $s_{23} \equiv m_{23}^2$, and $s_{13} \equiv m_{13}^2$, are related by a kinematic constraint:

$$s_{12} + s_{23} + s_{13} = M^2 + m_1^2 + m_2^2 + m_3^2.$$

The decay kinematics is therefore completely specified by any pair of the invariant mass combinations; a two-dimensional plot of the event distribution in these variables is called a *Dalitz plot*. For $B^\pm$ decays into three charged mesons we use the two opposite-charge combinations, labeled (s_{23}, s_{13}).

The kinematically accessible range of values for the Mandelstam variables is

$$s_{23} \in [(m_2 + m_3)^2, (M - m_1)^2],$$
$$s_{13} \in [(m_1 + m_3)^2, (M - m_2)^2].$$

For a given value of s_{23},

$$s_{13} = s_{13}^{\min}(s_{23}) \left(\frac{1 + \cos\theta_{13}}{2} \right) + s_{13}^{\max}(s_{23}) \left(\frac{1 - \cos\theta_{13}}{2} \right),$$

where $s_{13} \in [s_{13}^{\min}, s_{13}^{\max}]$, and θ_{13} is the helicity angle. In the rest frame of particles $(2,3)$, θ_{13} is the angle between particles $(1,3)$ and

$$s_{13}^{\min} = (E_1 + E_3)^2 - (p_2 + p_3)^2,$$
$$s_{13}^{\max} = (E_1 + E_3)^2 - (p_2 - p_3)^2,$$

where E_1, E_3 and p_2, p_3 are the energies and momenta of respective particles.

The $B^\pm \to K^\pm K^\pm K^\mp$ Dalitz plot contour is shown in Fig. 6.1 (a). For modes with identical particles in the final state, we order the daughter particles such that $s_{23} \leq s_{13}$, giving a folded Dalitz plot shown in Fig. 6.1 (b). Finally to emphasize the regions of smaller invariant mass we use the di-kaon invariant mass scatter plot (m_{23}, m_{13}) shown in Fig. 6.1 (c).

For three-body decays the decay rate Γ is given by

$$d\Gamma = \frac{1}{(2\pi)^3} \frac{1}{32M^3} |\mathcal{M}|^2 ds_{23} ds_{13}. \tag{6.1}$$

The Dalitz plot thus gives a graphical representation of the variation of the square of the matrix element $|\mathcal{M}|^2$ over the kinematically accessible phase space of the process (s_{23}, s_{13}). Eq. 6.1 can be rewritten as

$$d\Gamma = \frac{1}{(2\pi)^3} \frac{1}{32M^3} |\mathcal{M}|^2 \mathcal{J} dm_{23} dm_{13},$$

where $\mathcal{J} = 8m_{23}m_{13}$ is the Jacobian of the transformation from the Dalitz plot of Fig. 6.1 (a) to the folded di-kaon invariant mass scatter plot of Fig. 6.1 (c).
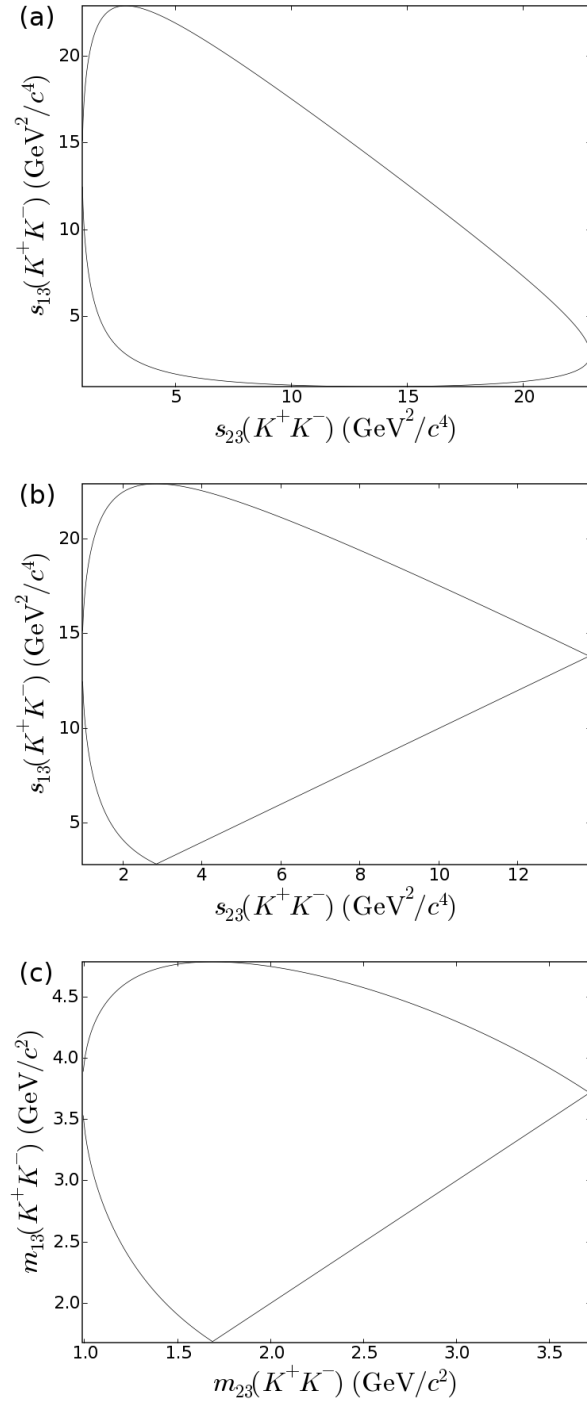
Figure 6.1: Countours of kinematic plots for $B^{\pm} \rightarrow K^{\pm}K^{\pm}K^{\mp}$: (a) Dalitz plot, (b) folded Dalitz plot, (c) di-kaon invariant mass plot.

6.2   Partial-wave expansion

Decay and scattering amplitudes are closely related [50]. In this analysis, we take the ansatz that the decay matrix element can be parameterized as a sum of two-body amplitudes in the (2,3) and (1,3) channels:

$$\mathcal{M} = \mathcal{M}_{23} + \mathcal{M}_{13}. \tag{6.2}$$

Possible interactions between same-sign particles in the (1,2) channel or three-body interactions, beyond a constant term that can be accommodated in Eq. (6.2), are neglected.

All particles involved in the decay are spinless and the two-body amplitudes can be written as a partial-wave expansion:

$$\mathcal{M}_{23} = \sum_{J=0}^{J_{\max}} \rho_J(s_{23}) e^{i\phi_J(s_{23})} P_J(\cos\theta_{13}), \tag{6.3}$$

$$\mathcal{M}_{13} = \sum_{J=0}^{J_{\max}} \rho_J(s_{13}) e^{i\phi_J(s_{13})} P_J(\cos\theta_{23}), \tag{6.4}$$

where ρ_J and ϕ_J are the mass-dependent magnitude and phase of the J-th partial wave and $P_J(\cos\theta)$ is an order-J Legendre polynomial. The sum is truncated at the partial wave $J_{\max}$ once a good fit is achieved.

For two-body scattering experiments the partial-wave analysis method is used to extract the individual scattering contributions in a model-independent way. A fit to the distribution allows the extraction of the magnitudes of the partial waves, and the phases relative to the phase of the reference wave. However, the variation of the phase of the reference wave as a function of the invariant mass cannot be determined, unless an additional constraint can be imposed, e.g., from unitarity.

In the context of a three-body decay the partial-wave analysis is complicated by the interference between the $\mathcal{M}_{23}$ and $\mathcal{M}_{13}$ amplitudes. However, if one of the amplitudes is known, e.g., determined from a fit to a model, the Dalitz plot can be used as an interferometer, and it is possible to perform a partial-wave analysis to extract the magnitudes and phases of the other amplitude.

6.3   Isobar model

A widely used approximation to the parameterization of the matrix element is the isobar model [51, 52]. Each of the two-body partial-wave amplitudes is decomposed into a sum of components:

$$\rho_J(s_{23})e^{i\phi_J(s_{23})} = \sum_k \rho_k e^{i\phi_k} T_k(s_{23}), \tag{6.5}$$

$$\rho_J(s_{13})e^{i\phi_J(s_{13})} = \sum_k \rho_k e^{i\phi_k} T_k(s_{13}), \tag{6.6}$$

where T_k is a two-body amplitude for the k-th component of the partial wave and $\rho_k e^{i\phi_k}$ is a complex production coefficient. In the isobar model, the individual terms are interpreted as complex production amplitudes for two-body resonances (isobars). The sum can also include terms describing the nonresonant component that cannot be easily identified with a dominant resonance. Combining the expansions of Eqs. (6.3-6.6),

$$\mathcal{M}_{23} = \sum_k \rho_k e^{i\phi_k} T_k(s_{23}) P_{J_k}(\cos\theta_{13}),$$

$$\mathcal{M}_{13} = \sum_k \rho_l e^{i\phi_k} T_k(s_{13}) P_{J_k}(\cos\theta_{23}),$$

and the isobar model matrix element is a sum of components:

$$\mathcal{M} = \sum_k \mathcal{M}_k = \sum_k \rho_k e^{i\phi_k} \mathcal{A}_k$$

The overall phase of the matrix element is arbitrary, only component phase differences $\phi_{kl} = \phi_l - \phi_k$ can be measured.

For $B^\pm \to K^\pm K^\pm K^\mp$ the matrix element must be symmetrized with respect to the $\{1 \leftrightarrow 2\}$ interchange of the identical kaons giving

$$\mathcal{M} = \sum_k \frac{\rho_k e^{i\phi_k}}{\sqrt{2}} \left(T_k(s_{23}) P_{J_k}(\cos\theta_{13}) + T_k(s_{13}) P_{J_k}(\cos\theta_{23}) \right). \tag{6.7}$$

We adopt a convenient normalization convention such that the expectation of the signal event

yield density in the Dalitz plot is given by the square of the matrix element multiplied by the experimental efficiency:

$$\frac{dY}{ds_{23}ds_{13}} = \epsilon(s_{23}, s_{13})|\mathcal{M}(s_{23}, s_{13})|^2, \tag{6.8}$$

$$Y = \int \epsilon(s_{23}, s_{13})|\mathcal{M}(s_{23}, s_{13})|^2 ds_{23}ds_{13} = \bar{\epsilon} \int |\mathcal{M}(s_{23}, s_{13})|^2 ds_{23}ds_{13}. \tag{6.9}$$

Here, because different regions of the Dalitz plot correspond to different event topologies, the efficiency, $\epsilon(s_{23}, s_{13})$, can be non-uniform across the Dalitz plot. The isobar-model average efficiency $\bar{\epsilon}$ is defined by Eq. (6.9).

As the experimental apparatus has a finite resolution, measurements of kinematic quantities will be different from their true values. In this analysis, we ignore the resolution effects in the fit. This approximation works well when the intrinsic scale of variation for component amplitudes is much larger than the experimental resolution. When this is not the case, we include the effect of neglecting the experimental resolution in the systematic error.

Normalization choices for the matrix element often vary between experiments, and normalization-independent component fractions,

$$F_k \equiv \frac{\int |\mathcal{M}_k|^2 ds_{23}ds_{13}}{\int |\mathcal{M}|^2 ds_{23}ds_{13}}, \tag{6.10}$$

are often reported to facilitate comparisons. Partial branching fractions,

$$\mathcal{B}_k \equiv F_k \mathcal{B}, \tag{6.11}$$

are defined as the product of the component fractions and the total branching fraction. Interference terms fractions are given by

$$F_{kl} \equiv 2\Re \frac{\int \mathcal{M}_k \mathcal{M}_l^* ds_{23}ds_{13}}{\int |\mathcal{M}|^2 ds_{23}ds_{13}}, \tag{6.12}$$

with

$$\sum_k F_k + \sum_{k<l} F_{kl} = 1. \tag{6.13}$$

It can be seen from Eq. (6.13) that, in general, $\sum_k \mathcal{B}_k \neq \mathcal{B}$ because of the interference between the components.

Direct CP asymmetry is accommodated by using two different isobar models for B^+ and B^- decays. Charge-dependent production coefficients are defined as

$$\rho_k^{\pm} e^{i\phi_k^{\pm}} = \rho_k \sqrt{\frac{1 \mp A_k}{2}} e^{i\phi_k} e^{\mp i\delta\phi_k/2}, \tag{6.14}$$

where A_k is the CP asymmetry in the k-th channel defined by

$$A_k = \frac{\rho_k^{2-} - \rho_k^{2+}}{\rho_k^{2+} + \rho_k^{2-}}, \tag{6.15}$$

and $\delta\phi_k = \phi_k^- - \phi_k^+$. A fit to the event distribution with respect to $\bigcup_{k=1}^{n}(\rho_k, A_k, \phi_k^+, \phi_k^-)$ gives a direct measurement of the CP asymmetry for each component. As before, the overall phase for each charge is arbitrary.

6.4   Resonant amplitudes

We consider a contribution to the matrix element from an isolated intermediate spin-J resonance with a mass m_0 and a total width Γ_0, corresponding to the decay chain $B^{\pm} \to K^{\pm}X$, $X \to K^{\pm}K^{\mp}$. It is convenient to work in the rest frame of the resonance. Denoting by s the invariant mass of the two kaons that form the resonance, their momentum is given by

$$q = |\boldsymbol{q}| = \frac{\sqrt{s - 4m_{K^{\pm}}^2}}{2};$$

the corresponding invariant phase space of the two-body decay $X \to K^{\pm}K^{\mp}$ is

$$\varrho = \frac{2q}{\sqrt{s}} = \sqrt{1 - \frac{4m_{K^{\pm}}^2}{s}};$$

and the momentum of the bachelor kaon is

$$p = |\boldsymbol{p}| = \frac{\sqrt{m_B^4 + s^2 + m_{K^\pm}^4 - 2m_B^2 s - 2m_B^2 m_{K^\pm}^2 - 2sm_{K^\pm}^2}}{2\sqrt{s}}.$$

The momentum of the bachelor kaon in the rest frame of the decaying B meson is

$$p^* = |\boldsymbol{p^*}| = \frac{\sqrt{s}}{m_B} p = \frac{\sqrt{m_B^4 + s^2 + m_{K^\pm}^4 - 2m_B^2 s - 2m_B^2 m_{K^\pm}^2 - 2sm_{K^\pm}^2}}{2m_B}.$$

The relativistic Breit-Wigner amplitude is given by

$$\mathcal{A}(s, \cos\theta) = \frac{F_J(p^* R_B) F_J(q R_X)}{m_0^2 - s - im_0(\Gamma_0 + \Delta\Gamma(s))} P_J(\cos\theta), \tag{6.16}$$

where F_J are centrifugal barrier factors for two spinless particles in a state of angular momentum J undergoing scattering with an interaction range R with an asymptotic behavior $F_J(x) \propto x^J$ for $x \ll 1$, and $F_J(x) \sim 1$ for $x \gg 1$. We use Blatt-Weisskopf barrier factors [53]: $F_0(x) = 1$, $F_1(x) = x/\sqrt{1 + x^2}$, $F_2(x) = x^2/\sqrt{(x^2 - 3)^2 + 9x^2}$, etc.

The expression in Eq. (6.16) is equivalent to the Zemach angular-momentum tensor formalism [54, 55]. The first three Zemach tensors are given by $Z_0(\boldsymbol{p}, \boldsymbol{q}) = 1$, $Z_1(\boldsymbol{p}, \boldsymbol{q}) = -2\boldsymbol{p} \cdot \boldsymbol{q}$, $Z_2(\boldsymbol{p}, \boldsymbol{q}) = \frac{4}{3}\left(3(\boldsymbol{p} \cdot \boldsymbol{q})^2 - |\boldsymbol{p}|^2|\boldsymbol{q}|^2\right)$, and in general

$$Z_J(\boldsymbol{p}, \boldsymbol{q}) \propto p^J q^J P_J(\cos\theta).$$

The expression in Eq. 6.16 can therefore be rewritten up to a multiplicative constant as

$$\mathcal{A}(s, \cos\theta) = \frac{\tilde{F}_J(p^* R_B) \tilde{F}_J(q R_X)}{m_0^2 - s - im_0(\Gamma_0 + \Delta\Gamma(s))} Z_J(\vec{p}, \vec{q}) \left(\frac{\sqrt{s}}{m_B}\right)^J, \tag{6.17}$$

where the modified Blatt-Weisskopf barrier factors are: $\tilde{F}_0(x) = 1$, $\tilde{F}_1(x) = 1/\sqrt{1 + x^2}$, $\tilde{F}_2(x) = 1/\sqrt{(x^2 - 3)^2 + 9x^2}$, etc. The last term $(\sqrt{s}/m_B)^J = (p^*/p)^J$ appears because the Zemach tensors are defined in terms of the bachelor kaon momentum in the rest frame of the resonance, while the

Blatt-Weisskopf barrier factor for the $B^\pm \to K^\pm X$ decay is defined in terms of the bachelor kaon momentum in the rest frame of the decaying B meson.

The term $\Delta\Gamma(s)$ appearing in the denominator parameterizes the mass dependence of the total width and can be important near kinematic thresholds. In general, the total width of the resonance is given by $\Gamma_0 = \sum_k \Gamma_k$, $\Delta\Gamma_k(s) = \sum_k \Delta\Gamma_k(s)$, where the sums are over all of the decay channels of the resonance. The mass dependence of the partial width of the decay into two pseudoscalars, such as $X \to K^+K^-$, can be parameterized as

$$\Delta\Gamma_k(s) = \Gamma_k \left(\frac{\varrho}{\varrho_0} \frac{F_j^2(qR_X)}{F_j^2(q_0R_X)} - 1 \right), \tag{6.18}$$

where ϱ_0 and q_0 are evaluated for $s = m_0^2$. For three-body decays of the X resonance or decays to a final state containing higher-spin particles the expression will be more complicated. Resonance partial decay widths can often be taken to be constant ($\Delta\Gamma_k(s) = 0$) if the resonance is narrow, and far away from the corresponding decay thresholds.

When the resonance is close to, but below the threshold the relativistic Breit-Wigner amplitude can be replaced by the parameterization originally due to Flatté [56]. In this analysis, it is applied to the scalar $f_0(980)$ resonance that can couple to $K\overline{K}$ and $\pi\pi$ final states. The amplitude is given by

$$\mathcal{A}(s) = \frac{1}{m_0^2 - s - im_0 \left(\varrho_\pi g_\pi + \varrho_K g_K \right)}, \tag{6.19}$$

where g_π and g_K are the $f_0(980)$ couplings to $K\overline{K}$ and $\pi\pi$ final states and

$$\varrho_\pi = 2/3\sqrt{1 - 4m_{\pi^\pm}^2/s} + 1/3\sqrt{1 - 4m_{\pi^0}^2/s},$$

$$\varrho_K = 1/2\sqrt{1 - 4m_{K^\pm}^2/s} + 1/2\sqrt{1 - 4m_{K^0}^2/s}.$$

6.5 Nonresonant amplitude

Three-body decays of D mesons have been studied extensively. These decays are typically dominated by light-meson resonances. The nonresonant amplitude contribution is typically small and it can be to a good approximation taken to be constant over the Dalitz plot [57, 58]. This approximation is essentially a zeroth order term in the Taylor expansion of the S-wave scattering:

$$\mathcal{A}_{\mathrm{NR}}(s_{23}, s_{13}) = \rho_{23}(s_{23})e^{i\phi_{23}(s_{23})} + \rho_{13}(s_{13})e^{i\phi_{13}(s_{13})}. \tag{6.20}$$

The phase space available to the decay of the B meson is larger by a factor of order m_B^4/m_D^4 and treating the nonresonant component as a constant is not likely to be a good approximation. A better fit can be obtained by continuing the Taylor expansion to include a term linear in s_{23} and s_{13}. To ensure that the magnitudes stay positive, we exponentiate and expand the logarithm:

$$\log \rho(s) \approx \log \rho + \frac{1}{\rho}\frac{\partial \rho}{\partial s}\delta s, \tag{6.21}$$

$$\phi(s) \approx \phi + \frac{\partial \phi}{\partial s}\delta s, \tag{6.22}$$

giving after appropriate redefinitions:

$$\mathcal{A}_{\mathrm{NR}}(s_{23}, s_{13}) = \rho_{23}e^{i\phi_{23}}e^{(-\alpha_{23}+i\beta_{23})s_{23}} + \rho_{13}e^{i\phi_{13}}e^{(-\alpha_{13}+i\beta_{13})s_{13}}, \tag{6.23}$$

or for $B^{\pm} \to K^{\pm}K^{\pm}K^{\mp}$, after symmetrization with respect to $\{1 \leftrightarrow 2\}$,

$$\mathcal{A}_{\mathrm{NR}}(s_{23}, s_{13}) = \frac{\rho e^{i\phi}}{\sqrt{2}}\left(e^{(\alpha+i\beta)s_{23}} + e^{(\alpha+i\beta)s_{13}}\right). \tag{6.24}$$

In general, we expect that the nonresonant amplitude will not have much phase variation and that its magnitude will be a slowly decreasing function of energy as the particles have less time to interact. A similar ansatz has been made in the $B^{\pm} \to K^{\pm}K^{\pm}K^{\mp}$ analysis by the Belle collaboration [59]
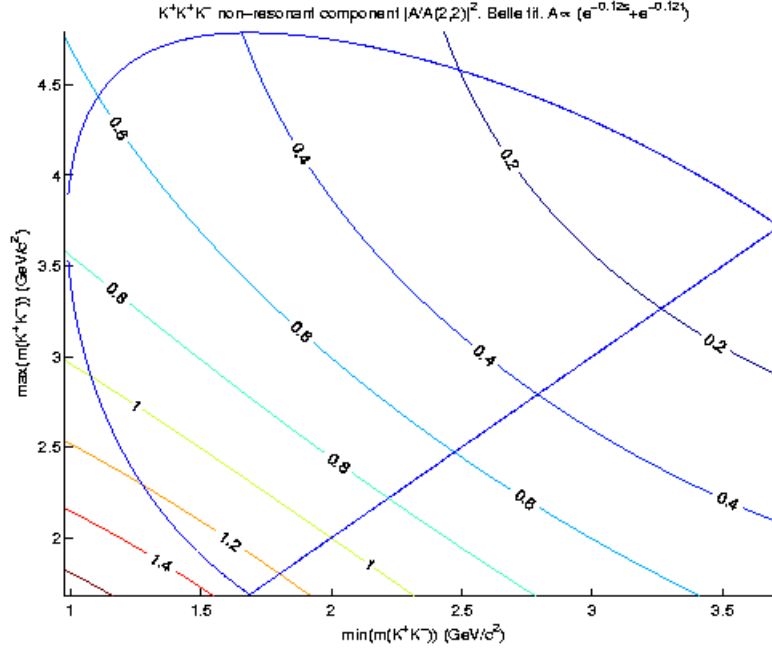
Figure 6.2: Functional dependence of the square of the nonresonant component used by the Belle collaboration analysis of $B^{\pm} \to K^{\pm}K^{\pm}K^{\mp}$.

where the nonresonant amplitude is parameterized as

$$\mathcal{A}_{\mathrm{NR}}(s_{23}, s_{13}) = \frac{\rho e^{i\phi}}{\sqrt{2}} \left(e^{-\alpha s_{23}} + e^{-\alpha s_{13}} \right), \qquad (6.25)$$

and the best fit gives $\alpha = (0.121 \pm 0.014)\,\mathrm{GeV}^{-2}c^4$. The nonresonant component branching fraction (Eq. (6.11)) is evaluated to be $\mathcal{B}_{\mathrm{NR}} = (24.0 \pm 1.5 \pm 1.8) \times 10^{-6}$, or $(74.8 \pm 3.6)\%$ of the total $B^{\pm} \to K^{\pm}K^{\pm}K^{\mp}$ branching fraction. A contour plot of $|\mathcal{A}_{\mathrm{NR}}/\mathcal{A}_0|^2$ is shown in Fig. 6.2, where $\mathcal{A}_0$ is the value of the amplitude evaluated at $m_{23} = 2\,\mathrm{GeV}/c^2$, $m_{13} = 2\,\mathrm{GeV}/c^2$.

We have also investigated two theoretical models of the nonresonant component [60, 61], which we will briefly review here. Both models are based on the naive factorization approach of Section 2.5 applied to the operator product expansion effective Hamiltonian of Section 2.2, giving real-valued nonresonant amplitude parameterizations with no phase variation over the Dalitz plot.

In the Fajfer, Pham, and Prapotnik model of Ref. [60] the leading contributions to the nonreso-
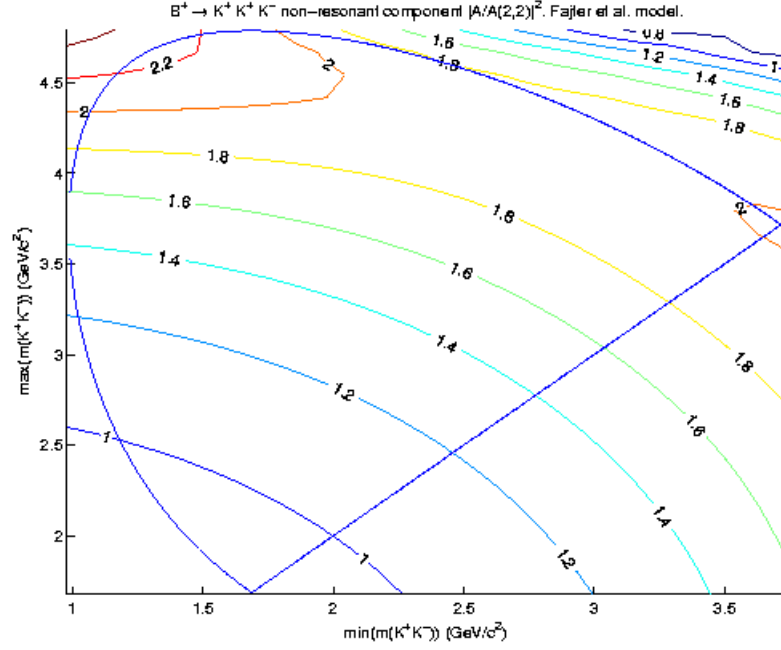
Figure 6.3: Functional dependence of the square of the nonresonant component parameterized according to the model of Fajfer, Pham, and Prapotnik [60].

nant amplitude is

$$\mathcal{A}_{\mathrm{NR}}(s_{23}, s_{13}) \quad \propto \quad \{w_+(s_{23}, s_{13})(m_B^2 - m_K^2 - s_{23})/2 +$$

$$w_-(s_{23}, s_{13})(s_{23} + 2s_{13} - m_B^2 - 3m_K^2)/2\} +$$

$$\{1 \leftrightarrow 2\},$$

where $w_\pm$ are form factors. The form factors, calculated by applying the Heavy Quark Chiral Perturbation Theory (HQChPT) to both the weak and strong interaction vertices, receive contributions from three-body contact terms and B^* pole diagrams. The nonresonant component branching fraction is evaluated to be $\mathcal{B}_{\mathrm{NR}} = 9 \times 10^{-6}$, significantly smaller than the value reported by the Belle collaboration. A contour plot of $|\mathcal{A}_{\mathrm{NR}}/\mathcal{A}_0|^2$ is shown in Fig. 6.3, where $\mathcal{A}_0$ is the value of the amplitude evaluated at $m_{23} = 2\,\mathrm{GeV}/c^2$, $m_{13} = 2\,\mathrm{GeV}/c^2$.

The approach of Ref. [60] has been criticized by Cheng and Yang in Ref. [61]. For three-body B decays the momentum of the final state mesons is comparable to or larger than the chiral symmetry
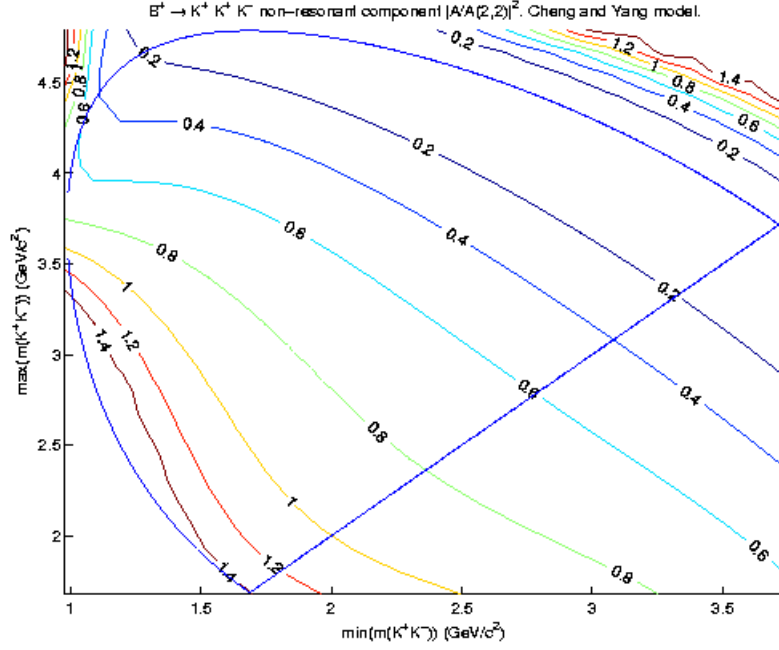
Figure 6.4: Functional dependence of the square of the nonresonant component parameterized according to the model of Cheng and Yang [61].

breaking scale, $\Lambda_\chi \sim 830\,\text{MeV}$, over much of the Dalitz plot, and in the calculation of form factors $w_\pm$ in Ref [60] the HQChPT theory may have been applied twice beyond the range of its validity. The problem is made manifest by a numeric example; when applied to the $B^\pm \to K^\pm \pi^\pm K^\mp$ decay, the approach of Ref. [60] gives a branching fraction prediction that is much larger than the current experimental upper limit.

In the alternative model proposed by Cheng and Yang, the HQChPT is applied to the strong vertex only, and the invariant mass dependence of the weak vertex is parameterized using form factors. The functional dependence of form factors is not known *a priori*; Fig. 6.4 shows a contour plot of the square of the amplitude parameterized according to the model of Cheng and Yang using an ad hoc parameterization of the form factors suggested in the paper. While the amplitude shape is qualitatively similar to that used by the Belle collaboration [59], this choice of form factors leads to an estimate of $\mathcal{B}_{\text{NR}}/\mathcal{B}(B^\pm \to K^\pm K^\pm K^\mp) = 3\%$ for the nonresonant component fraction — much smaller than the value reported by the Belle collaboration.

After surveying the theoretical models and comparing them with the experimental results from the Belle collaboration, we conclude that the proposed theoretical models are in disagreement with the data and no successful physics-based parameterization of the nonresonant component in charmless three-body B decays exists to date. In this analysis, we therefore follow the approach used by the Belle collaboration and use an ad hoc parameterization of the nonresonant component, which is motivated by an expansion of the amplitude beyond the usual constant term.

6.6   Discrete ambiguities

In certain cases, the production coefficients in an isobar model fit can only be determined up to a discrete ambiguity. As an example, we consider a region of the Dalitz plot where a narrow scalar resonance is interfering with a nonresonant component. The matrix element is modeled as

$$\mathcal{M} \propto \rho_{\mathrm{NR}} e^{i\phi_{\mathrm{NR}}} + \rho e^{i\phi} \frac{1}{m_0^2 - s - im_0\Gamma_0},$$

where the nonresonant component is taken to be constant across the narrow resonance and the resonant amplitude is parameterized as a relativistic Breit-Wigner for which the possible mass dependence of the width has been neglected. Introducing the resonant phase shift δ defined by

$$\tan\delta \equiv \frac{m_0\Gamma_0}{m_0^2 - s},$$

after appropriate redefinitions

$$\mathcal{M} \propto 1 + \rho e^{i\phi}\sin\delta\, e^{i\delta},$$

where $\rho e^{i\phi}$ is the resonance production coefficient relative to the nonresonant component. The density of observed signal events is proportional to the square of the amplitude:

$$|\mathcal{M}|^2 \propto 1 + (\rho^2 - 2\rho\sin\phi)\sin^2\delta + 2\rho\cos\phi\sin\delta\cos\delta. \tag{6.26}$$

Identical event distributions will be observed for two different production coefficients, $\rho_1 e^{i\phi_1}$ and $\rho_2 e^{i\phi_2}$, as long as the following system of equations is satisfied:

$$\rho_1^2 - 2\rho_1 \sin\phi_1 = \rho_2^2 - 2\rho_2 \sin\phi_2,$$
$$\rho_1 \cos\phi_1 = \rho_2 \cos\phi_2. \tag{6.27}$$

Given one solution with the production coefficient $\rho_1 e^{i\phi_1}$, the conjugate solution is given by

$$\rho_2 = \sqrt{(\rho_1 - 2\sin\phi_1)^2 + 4\cos^2\phi_1},$$
$$\cos\phi_2 = \rho_1/\rho_2 \cos\phi_1. \tag{6.28}$$

Fig. 6.5 is a graphical illustration of this type of degeneracy for the case of $\rho_1 e^{i\phi_1} = 2e^{-i\pi/6}$, $\rho_2 e^{i\phi_2} = 2\sqrt{3}e^{i\pi/3}$. While the circles traced in the Argand diagram are different for the two generated amplitudes, the square of the amplitude as a function of the phase shift δ is the same in both cases. Another (extreme) example of this degeneracy is the fact that a flat density generated when no resonance is present, $\rho_1 e^{i\phi_1} = 0$, can also be a result of the interference between the nonresonant component and a resonance with $\rho_2 e^{i\phi_2} = 2e^{i\pi/2}$. The condition for the resonance to be clearly observed is $\rho_{1,2} \gg 1$, in which case Eq. (6.28) simplifies to

$$\rho_2 \approx \rho_1 - 2\sin\phi_1,$$
$$\phi_2 \approx -\phi_1. \tag{6.29}$$

We finally note that this type of degeneracy is lifted if the resonance has non-zero spin, if it interferes with another non-constant amplitude in the orthogonal channel, or if the nonresonant amplitude has significant variation across the resonance. Even when the exact degeneracy is lifted by one of the mechanisms mentioned above, finite experimental resolution and limited statistics can conspire to produce approximate discrete ambiguities of this type.
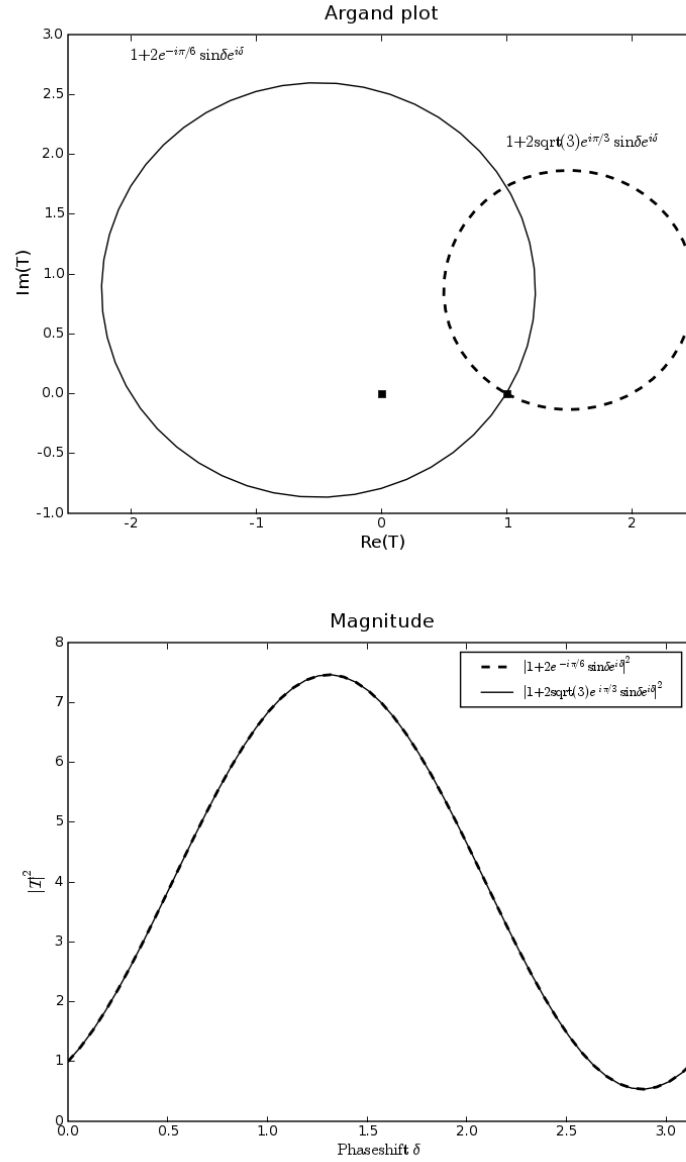
Figure 6.5: Discrete ambiguity example for the matrix element of Eq. (6.26). The Argand plot diagram (top), and amplitude squared as a function of the phase shift (bottom) for two conjugate solutions with production coefficients, $\rho_1 e^{i\phi_1} = 2e^{-i\pi/6}$ and $\rho_2 e^{i\phi_2} = 2\sqrt{3}e^{i\pi/3}$.

6.7 Binned maximum likelihood fit

In this analysis we use the method of binned maximum likelihood for estimating the parameters of the isobar model. The loss of statistical precision due to binning is minimal if the bin sizes are smaller than either the typical experimental resolution or the typical size of the Dalitz plot features. The unique advantages of a binned fit approach are:

- Computing the expected number of background events in a binned approach is much easier than constructing functional parameterizations of backgrounds whose rates and composition vary non-trivially over the Dalitz plot.

- In a binned fit, there is a close connection between the minimized value and goodness-of-fit, which is lacking for unbinned maximum likelihood fits.

- With a large number of events, computing unbinned likelihood becomes computationally expensive.

The probability (likelihood) of the observed distribution is given by the product of Poisson likelihoods for individual bins:

$$\mathcal{L} = \prod_{i=1}^{N} \frac{\mu_i^{n_i} e^{-\mu_i}}{n_i!},$$

where μ_i is the expected number of events in the i-th bin as a function of the estimated parameters and n_i is the number of events observed in the i-th bin. Parameter estimates are obtained by maximizing the likelihood; equivalently, we minimize the log of the likelihood-ratio statistic:

$$\chi^2_{\text{LLR}}/2 = \sum_{i=1}^{N} \mu_i - n_i + n_i \log \frac{n_i}{\mu_i}.$$

The variable χ^2_{LLR} is asymptotically distributed as a χ^2 variate for $\mu_i, n_i \gg 1$ with a number of degrees of freedom equal to the number of Dalitz plot bins minus the number of evaluated model parameters. The properties of the χ^2_{LLR} for bins with small numbers of events are discussed in [62].

For *CP* asymmetry fits the statistic is extended to:

$$\chi^2_{\mathrm{LLR}}/2 = \sum_{i=1}^{N} \mu_i^+ - n_i^+ + n_i^+ \log \frac{n_i^+}{\mu_i^+} + \sum_{i=1}^{N} \mu_i^- - n_i^- + n_i^- \log \frac{n_i^-}{\mu_i^-}. \tag{6.30}$$

We choose a non-uniform binning designed to capture the structure of the observed distribution of events. The expected number of events in each bin μ_i is the sum of signal and background contributions:

$$\mu_i = s_i + b_i + q_i,$$

where the expected number of properly reconstructed signal events s_i is evaluated by integrating the yield density of Eq. (6.8) over the bin,

$$s_i = \int_i \epsilon(s_{23}, s_{13}) |\mathcal{M}(s_{23}, s_{13})|^2 ds_{23} ds_{13};$$

the expected contribution arising from non-signal B decays b_i is evaluated using simulated samples of B decays as described in Chapter 5; and the expected contribution of $q\bar{q}$ backgrounds q_i is evaluated using extrapolation from the m_{ES} sideband:

$$q_i = R_{q\bar{q}}(n_i^{\mathrm{SB}} - b_i^{\mathrm{SB}}),$$

where n_i^{SB} is the number of events observed in the sideband bin, b_i^{SB} is the expected B background contribution in the sideband bin, and $R_{q\bar{q}}$ is the extrapolation coefficient described in Sec. 4.3. In order to have a well-defined Poisson likelihood, we require the total expectation μ_i to be non-negative in each bin.

We have neglected the contributions from misreconstructed signal events, which depend non-trivially on the signal model and the misreconstruction mechanism and are difficult to compute. Fortunately, their contributions are small and are largely absorbed in the q-term because of the similar m_{ES} shapes for misreconstructed signal events and $q\bar{q}$ continuum backgrounds. We have also neglected intermode cross-feeds between three-body charmless final states due to particle misidenti-

fication because they are small for the Cabibbo-favored $B^{\pm} \to K^{\pm}K^{\pm}K^{\mp}$ mode.

As an important technical note, in the isobar model,

$$s_i = \sum_{k,l} \rho_k \rho_l e^{i(\phi_k - \phi_l)} \int_i \epsilon(s_{23}, s_{13}) \mathcal{A}_k \mathcal{A}_l^* ds_{23} ds_{13}. \tag{6.31}$$

When fitting for parameters ρ and ϕ only, the bin integrals in Eq. (6.31) need only be computed once; at each iteration of the fitting process the expectations s_i can be computed by simply recalculating the sum. This is not the case when fitting for amplitude shape parameters; the expectations s_i in that case need to be recalculated at each minimization iteration by numeric integration, which is computationally expensive. Approximations and iterative fitting techniques can be used to mitigate against this problem.

The overall branching fraction is given by

$$\mathcal{B} = \frac{n - b - q}{\bar{\epsilon}}, \tag{6.32}$$

where $n = \sum_{i=1}^N n_i$, $b = \sum_{i=1}^N b_i$, $q = \sum_{i=1}^N q_i$, and $\bar{\epsilon}$ is the average efficiency of Eq. (6.9). The overall CP asymmetry is given by

$$A = \frac{n^- - n^+}{n - b - q}, \tag{6.33}$$

where $n^{\pm} = \sum_{i=1}^N n_i^{\pm}$ and an assumption has been made that there is no asymmetry for the backgrounds.

6.8 Statistical errors and error propagation

We briefly discuss the evaluation of statistical errors arising from the intrinsic randomness of the observed processes.

For efficiency determination, the number of events n selected from a sample of N events and satisfying a certain selection criterion is distributed according to a binomial distribution with probability equal to the selection efficiency ϵ. For a binomial distribution, an unbiased estimator of the

efficiency is $\hat{\epsilon} = n/N$ and its variance is $\sigma_{\hat{\epsilon}}^2 = \epsilon(1-\epsilon)/N$. The efficiency and its statistical uncertainty are therefore estimated as

$$\epsilon = \frac{n}{N} \pm \sqrt{\frac{n/N(1 - n/N)}{N}}.$$

When the distribution of an estimator is not readily computed, we use error propagation. For a function $X(\theta_i)$, which depends on a vector of parameters θ_i, evaluated with an uncertainty given by a covariance matrix Σ_{kl}, assuming that the parameter errors are small we can write an estimator:

$$\hat{X}(\theta_i) = X(\hat{\theta}_i),$$

and its variance:

$$\sigma_{\hat{X}}^2 = \sum_{kl} \frac{\partial X}{\partial \theta_k} \frac{\partial X}{\partial \theta_l} \Sigma_{kl}. \tag{6.34}$$

We consider, as an example, a CP asymmetry estimator:

$$\hat{A}(n_+, n_-) \equiv \frac{n_- - n_+}{N}, \tag{6.35}$$

where $n_\pm$ are the numbers of selected $B^\pm$ events, respectively, and $N = n_+ + n_-$. The derivatives are given by

$$\frac{\partial \hat{A}}{\partial n_\pm} = \pm \frac{2n_\mp}{N^2}. \tag{6.36}$$

The covariance matrix assuming independent Poisson processes for $n_\pm$ is

$$\Sigma_{+-} = \begin{pmatrix} n_+ & 0 \\ 0 & n_- \end{pmatrix}, \tag{6.37}$$

giving

$$\sigma_{\hat{A}}^2 = \frac{4n_+ n_-}{N^3} = \frac{1 - \hat{A}^2}{N}. \tag{6.38}$$

The asymmetry and its statistical uncertainty are therefore estimated as

$$A = \frac{n_- - n_+}{N} \pm \frac{1}{\sqrt{N}} \frac{\sqrt{4 n_+ n_-}}{N}. \tag{6.39}$$

In our maximum likelihood fits we use the MINUIT [63] package for numeric minimization of χ^2_{LLR}. The covariance matrix of the parameter estimates is asymptotically related to the Hessian of the log-likelihood evaluated at the minimum:

$$\Sigma^{-1}_{kl} = H_{kl} = \frac{1}{2} \frac{\partial^2 \chi^2_{\mathrm{LLR}}}{\partial \theta_k \partial \theta_l}. \tag{6.40}$$

Derived quantities are estimated via error propagation of Eq. (6.34).

Chapter 7

$B^{\pm} \to K^{\pm}K^{\pm}K^{\mp}$ fit

In this chapter we apply the analysis formalism developed in Chapter 6 to the data sample selected in the $B^{\pm} \to K^{\pm}K^{\pm}K^{\mp}$ final state. We perform an isobar-model Dalitz plot fit in Section 7.1 and then a partial-wave analysis in Section 7.2.

7.1 Isobar-model fit

The Dalitz plot of the 1769 B^{+} and 1730 B^{-} candidates selected in the signal region is shown in Fig. 7.1. We divide it into 292 non-uniform rectangular bins as shown in Fig. 7.2 and perform a binned maximum likelihood fit using the isobar-model formalism described in Chapter 6. The efficiency is parameterized as a two-dimensional histogram (Fig. 4.12); the expected B backgrounds are determined as described in Chapter 5; and the expected $q\bar{q}$ backgrounds are extrapolated from the m_{ES} sideband as described in Section 4.3.

The isobar-model matrix element, parameterized as in Eq. (6.7), includes the following components:

- $B^{\pm} \to K^{\pm}\phi(1020)$

  The contribution from the vector $\phi(1020)$ resonance is clearly visible in the Dalitz plot of Fig. 7.1. We model the amplitude using the relativistic Breit-Wigner amplitude parameterization of Eq. (6.16). Because $m_{K^{\pm}} + m_{\phi} \ll m_B$, the B decay is far from the kinematic threshold and we approximate the B vertex barrier factor as $F_J(p^* R_B) \approx 1$. The interac-
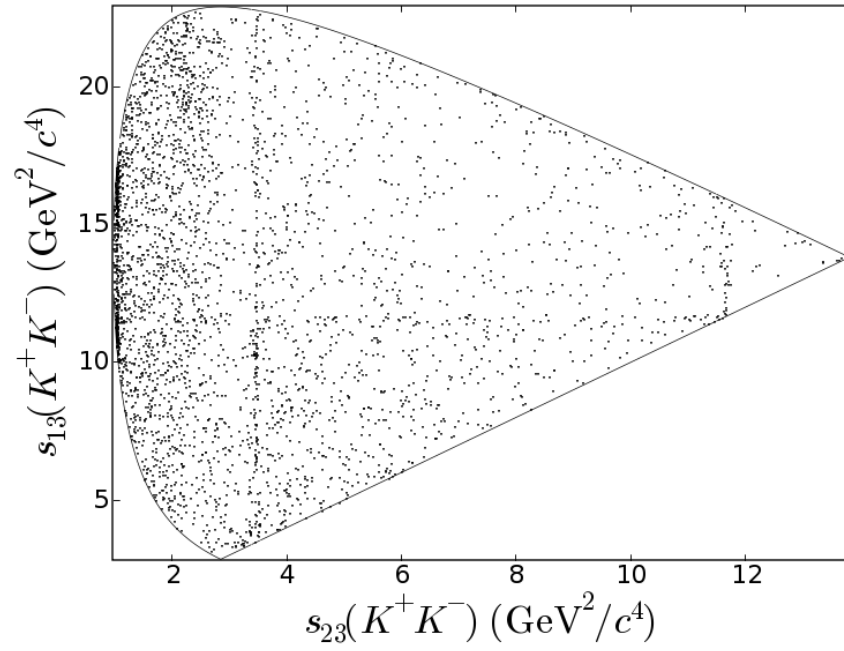
Figure 7.1: The Dalitz plot of the 1769 B^+ and 1730 B^- candidates selected in the signal m_{ES} region.
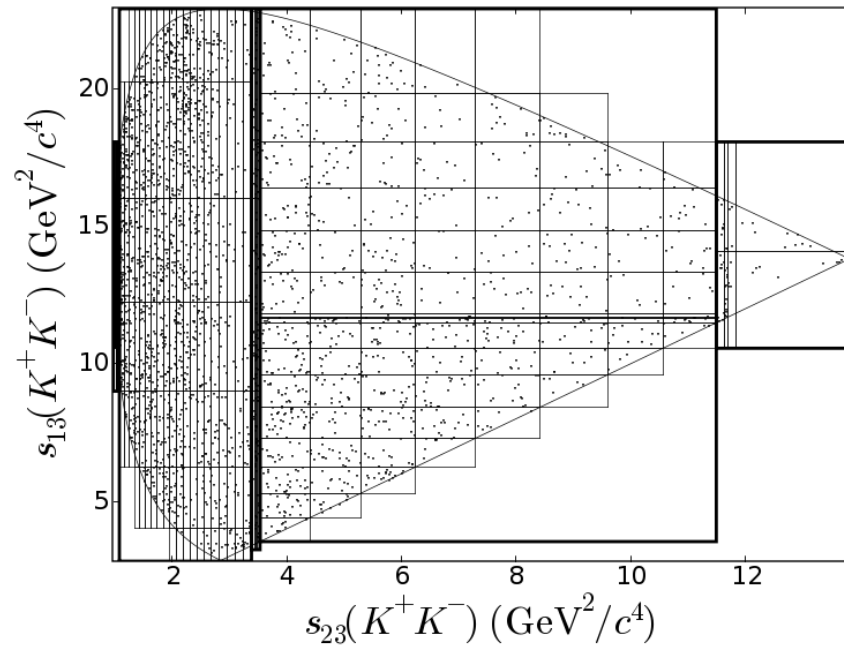
Figure 7.2: Non-uniform binning of the Dalitz plot used in the isobar-model fit. Finer binning is used around the ϕ, D^0, and χ_{c0} resonances, and for smaller values of s_{23}.

tion range R_ϕ has not been measured, and for the Blatt-Weisskopf barrier factor $F_J(qR_\phi)$ we use $R_\phi = 4.0\,\mathrm{GeV}^{-1}$, motivated by the recent FOCUS collaboration measurement of $R_{K^*} = 3.96 \pm 0.54^{+1.31}_{-0.90}\,\mathrm{GeV}^{-1}$ [64]. The $\phi(1020)$ is near the $K\overline{K}$ threshold and we use a mass-dependent width with $\Delta\Gamma(s) = \Delta\Gamma_1(s) + \Delta\Gamma_2(s)$, where $\Gamma_1 = \Gamma_0\mathcal{B}(\phi \to K^+K^-)$, $\Gamma_2 = \Gamma_0\mathcal{B}(\phi \to K^0\overline{K}^0)$, and $\Delta\Gamma_{1,2}$ are given by Eq. 6.18.

- $B^\pm \to K^\pm f_0(980)$.

  A large $B^\pm \to K^\pm f_0(980)$ signal measured in $B^\pm \to K^\pm\pi^\pm\pi^\mp$ [19, 28], and a recent measurement of the ratio of the $f_0(980)$ coupling constants to $K\overline{K}$ and $\pi\pi$ [65], motivate us to include an $f_0(980)$ contribution using the amplitude parameterization of Eq. (6.19).

  Define I_K/I_π to be the ratio of the integrals of the square of the $f_0(980)$ amplitude given by Eq. (6.19) over the $B \to KKK$ and $B \to K\pi\pi$ Dalitz plots. The partial branching fractions for $B^\pm \to K^\pm f_0(980)$ measured in the $K^\pm K^\pm K^\mp$ and $K^\pm\pi^\pm\pi^\mp$ final states are then related by the ratio

  $$R \equiv \frac{\mathcal{B}(B^\pm \to K^\pm f_0(980), f_0(980) \to K^+K^-)}{\mathcal{B}(B^\pm \to K^\pm f_0(980), f_0(980) \to \pi^+\pi^-)} = \frac{3}{4}\frac{I_K}{I_\pi}\frac{g_K}{g_\pi}, \tag{7.1}$$

  where 3/4 is an isospin factor. Experimental measurements of g_K/g_π [65–68] have significant uncertainties. The contribution of the $f_0(980)$ resonance was taken to be negligible in the Belle collaboration analysis of $B^\pm \to K^\pm K^\pm K^\mp$ [59] motivated by the small g_K/g_π value reported by the E791 collaboration, based on an analysis of the $D_s^\pm \to \pi^\pm\pi^\pm\pi^\mp$ decay with no direct observation of the $f_0(980) \to K\overline{K}$ coupling [68]. We consider the more recent BES collaboration measurement from a joint analysis of $J/\psi \to \phi\pi^+\pi^-$ and $J/\psi \to \phi K^+K^-$ to be superior, and in the following adopt their values: $m_0 = 0.965 \pm 0.008 \pm 0.006$, $g_\pi = 0.165 \pm 0.010 \pm 0.015\,\mathrm{GeV}/c^2$, and $g_K/g_\pi = 4.21 \pm 0.25 \pm 0.21$ [65]. For this choice of parameters, we compute $I_K/I_\pi = 0.29$, and $R = 0.92 \pm 0.07$ for the right-hand side of Eq. (7.1), where we have combined the statistical and systematic errors in quadrature. This suggests that the $B^\pm \to K^\pm f_0(980)$ contribution to $B^\pm \to K^\pm K^\pm K^\mp$ may be large.

- $B^\pm \to K^\pm X_0(1550)$.

Following Ref. [19], we introduce a broad scalar resonance, whose interference with a slowly varying nonresonant component is used to describe the rapid decrease in event density around $m(K^+K^-) = 1.6\,\mathrm{GeV}/c^2$. Evidence of a possible resonant S-wave contribution in this region has been reported previously [69, 70], however its attribution is uncertain: the $f_0(1370)$ and $f_0(1500)$ resonances are known to couple to $\pi\pi$ more strongly than to $K\overline{K}$ [14] and possible interpretations in terms of those states [13] must account for the fact that no strong $B^\pm \to K^\pm f_0(1370)$ or $B^\pm \to K^\pm f_0(1500)$ signal is observed in $B^\pm \to K^\pm \pi^\pm \pi^\mp$ [19, 28]; the contribution of the $f_0(1710)$ resonance is included in the fit as a separate component and is found to be small. In the following, we designate the broad scalar resonance $X_0(1550)$ and determine its mass and width directly from the fit. The amplitude is modeled using the relativistic Breit-Wigner amplitude parameterization of Eq. (6.16). As the $X_0(1550)$ resonance is speculative and its decay modes are unknown, we take its width to be constant.

- $B^\pm \to K^\pm f_0(1710)$.

  We include a potential contribution from the $f_0(1710)$ resonance, which has been measured to couple more strongly to $K\overline{K}$ than to $\pi\pi$ [71], and could potentially contribute to $B^\pm \to K^\pm K^\pm K^\mp$ without being observed in $B^\pm \to K^\pm \pi^\pm \pi^\mp$. The amplitude is modeled using the relativistic Breit-Wigner amplitude parameterization of Eq. (6.16). As the decay modes of the $f_0(1710)$ resonance are not well established, we take its width to be constant.

- $B^\pm \to K^+ \chi_{c0}$

  The contribution from the χ_{c0} resonance arising from the rescattering diagrams shown in Fig. 2.8 is clearly visible in the Dalitz plot of Fig. 7.1. The amplitude is modeled using the relativistic Breit-Wigner amplitude parameterization of Eq. (6.16). The χ_{c0} resonance has many decay modes. For simplicity we take its width to be constant.

- Nonresonant $B^\pm \to K^\pm K^\pm K^\mp$.

  In Section 6.5 we have surveyed the two published theoretical models [60, 61] for the $B^\pm \to K^\pm K^\pm K^\mp$ nonresonant component and concluded that both are in disagreement with the
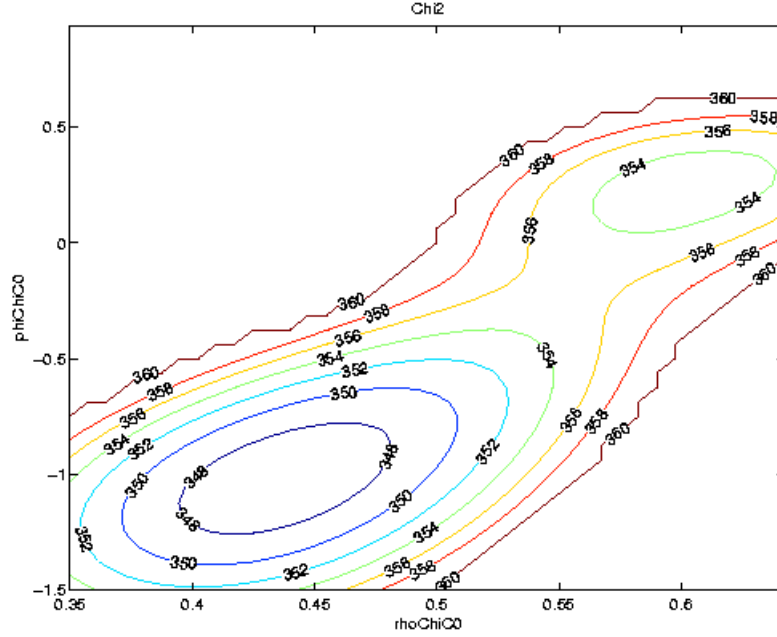
Figure 7.3: Scan of the χ^2_{LLR} function in the $(\rho_{\chi_{c0}}, \phi_{\chi_{c0}})$ plane, showing the two solutions from the best-fit doublet.

experimental data from the Belle collaboration [19]. We therefore adopt an ad hoc parameterization based on the expansion of Eq. (6.24). A fit to the $m_{23} > 2\,\mathrm{GeV}/c^2$ region dominated by the nonresonant component gives $\alpha = 0.140 \pm 0.019$, $\beta = -0.02 \pm 0.06$, consistent with no phase variation. In the following, we fix $\beta = 0$ and thus adopt the same parameterization as used by Belle [19].

We fit for the magnitudes and phases of the decay coefficients, the mass and width of the $X_0(1550)$, and the nonresonant component shape parameter α. As the overall complex phase of the isobar-model amplitude is arbitrary, we fix the phase of the nonresonant contribution to zero, leaving 14 free parameters in the fit. The number of degrees of freedom is $292 - 14 = 278$.

We perform multiple minimizations with different starting parameter values and cluster the fits using a Euclidean metric in the parameter space, with distance measured in units of expected uncertainty on the fit parameters. We find multiple solutions clustered in doublets, where the solutions within each doublet are very similar, except for the magnitude and phase of the χ_{c0}
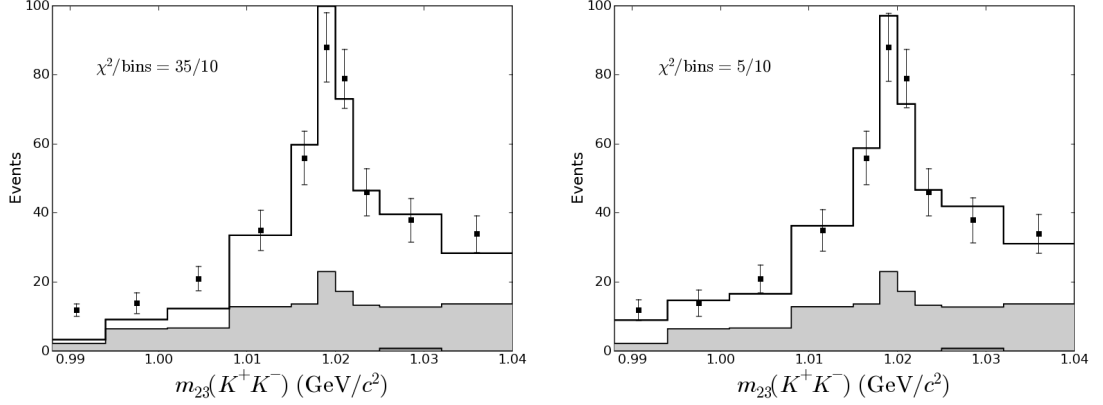
Figure 7.4: Mass projection of the fit without (left) and with (right) the $f_0(980)$ component near the K^+K^- threshold. The histogram shows the total expected number of events in each bin, with $B\bar{B}$ and $q\bar{q}$ background contributions shown in dark and light gray, respectively.

production coefficient. The twofold ambiguity arises from the interference between the narrow χ_{c0} and the nonresonant component that is approximately constant across the resonance, as discussed in Section 6.6. The highest-likelihood doublet has $\chi^2_{\rm LLR} = (346.6, 352.0)$; the second best doublet has $\chi^2_{\rm LLR} = (362.4, 368.7)$. A two-dimensional scan of $\chi^2_{\rm LLR}$ in the $(\rho_{\chi_{c0}}, \phi_{\chi_{c0}})$ plane while keeping all the other parameters fixed is shown in Fig. 7.3 for the highest-likelihood doublet.

The least significant components are the $f_0(980)$ and the $f_0(1710)$. The omission of the $f_0(980)$ component from the fit degrades the best fit from $\chi^2_{\rm LLR} = 346.6$ to 363.9 and the data distribution near the K^+K^- threshold is not described adequately as shown in Fig. 7.4. The omission of the $f_0(1710)$ degrades the fit to $\chi^2_{\rm LLR} = 360.7$.

The invariant mass projections of the best fit are shown in Fig. 7.5. The fit gives $\alpha = 0.152 \pm 0.011\,{\rm GeV}^{-2}c^4$, $m_0(X_0) = 1.539 \pm 0.020\,{\rm GeV}/c^2$, and $\Gamma_0(X_0) = 0.257 \pm 0.033\,{\rm GeV}/c^2$. The fitted values of the shape parameter α and the resonance mass are consistent with the values in Ref. [19], but our preferred value for the width is significantly larger than $\Gamma_0 = 0.14 \pm 0.02\,{\rm GeV}/c^2$, reported by the Belle collaboration [19].

The isobar-model weighted signal efficiency of Eq. (6.9) is $\bar{\varepsilon} = 0.282 \pm 0.011$, where the systematic error is evaluated in Chapter 8. Using Eqs. (6.32, 6.33), we calculate the total branching fraction and asymmetry to be $\mathcal{B}(B^\pm \to K^\pm K^\pm K^\mp) = (35.2 \pm 0.9) \times 10^{-6}$ and $A(B^\pm \to K^\pm K^\pm K^\mp) =$
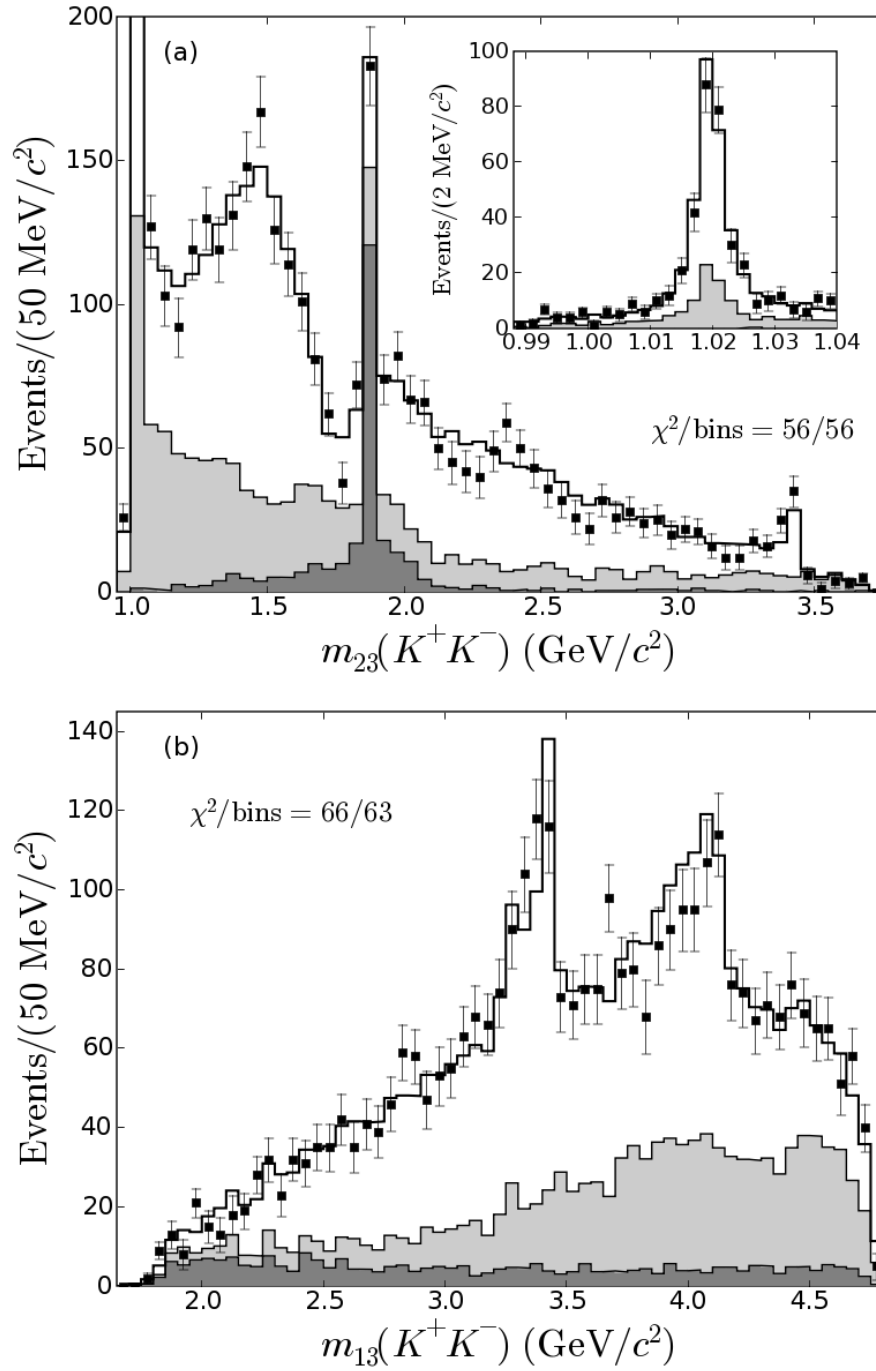
Figure 7.5: Mass projections of the best fit. The histogram shows the total expected number of events in each bin, with $B\bar{B}$ and $q\bar{q}$ background contributions shown in dark and light gray, respectively. The inset shows a fit projection near the ϕ resonance.

Table 7.1: Fit fractions of Eq. (6.10, 6.12) and phase differences of the best fit. In the top part of the table, the diagonal elements set in boldface correspond to the component fractions (Eq. (6.10)) and the elements above the diagonal correspond to the fractions of interference terms (Eq. (6.12)). The bottom part of the table gives the antisymmetric matrix of phase differences, $\phi_{ij} = \phi_j - \phi_i$.

F_{ij}	ϕ	$f_0(980)$	$X_0(1550)$	$f_0(1710)$	χ_{c0}	NR
ϕ	$\mathbf{11.8 \pm 0.9}$	-0.94 ± 0.18	-1.71 ± 0.36	0.01 ± 0.10	0.11 ± 0.02	3.54 ± 0.38
$f_0(980)$		$\mathbf{19 \pm 7}$	53 ± 12	-4.5 ± 2.9	-0.91 ± 0.19	-85 ± 21
$X_0(1550)$			$\mathbf{121 \pm 19}$	-30 ± 11	-1.10 ± 0.31	-140 ± 26
$f_0(1710)$				$\mathbf{4.8 \pm 2.7}$	-0.10 ± 0.07	4 ± 6
χ_{c0}					$\mathbf{3.1 \pm 0.6}$	3.87 ± 0.37
NR						$\mathbf{141 \pm 16}$
ϕ_{ij}	ϕ	$f_0(980)$	$X_0(1550)$	$f_0(1710)$	χ_{c0}	NR
ϕ	0	-2.51 ± 0.17	-1.70 ± 0.27	2.71 ± 0.35	2.27 ± 0.35	-2.99 ± 0.20
$f_0(980)$	2.51 ± 0.17	0	0.81 ± 0.25	-1.07 ± 0.36	-1.50 ± 0.33	-0.48 ± 0.16
$X_0(1550)$	1.70 ± 0.27	-0.81 ± 0.25	0	-1.88 ± 0.19	-2.32 ± 0.22	-1.29 ± 0.10
$f_0(1710)$	-2.71 ± 0.35	1.07 ± 0.36	1.88 ± 0.19	0	-0.44 ± 0.30	0.59 ± 0.25
χ_{c0}	-2.27 ± 0.35	1.50 ± 0.33	2.32 ± 0.22	0.44 ± 0.30	0	1.02 ± 0.23
NR	2.99 ± 0.20	0.48 ± 0.16	1.29 ± 0.10	-0.59 ± 0.25	-1.02 ± 0.23	0

Table 7.2: Means and standard deviations of the distributions of the residuals obtained in the fit bias study.

ϕ	$f_0(980)$		$X_0(1550)$			
ρ	ρ	ϕ	ρ	ϕ	m_0	Γ_0
(-0.01,1.00)	(0.08,1.06)	(-0.08,1.04)	(0.08,1.06)	(-0.11,1.10)	(-0.04,1.32)	(0.06,1.09)
$f_0(1710)$		χ_{c0}		NR		
ρ	ϕ	ρ	ϕ	ρ	ϕ	α
(0.11,1.03)	(-0.08,1.06)	(0.12,0.95)	(-0.11,1.16)	(0.06,1.03)	(-0.10,1.06)	(0.17,1.02)

$(-1.7 \pm 2.6)\%$.

The fit fractions of Eqs. (6.10, 6.12) and phase differences for the leading solution are shown in Table 7.1. In the top part of the table, the diagonal elements set in boldface correspond to the component fractions (Eq. (6.10)) and the elements above the diagonal correspond to the fractions of interference terms (Eq. (6.12)). Because of the large negative interference, in the scalar sector the sum of the diagonal fractions is substantially larger than 100%. The bottom part of the table gives the antisymmetric matrix of phase differences, $\phi_{ij} = \phi_j - \phi_i$. For the second solution in the leading doublet, the χ_{c0} fraction is increased to $6.0 \pm 0.7\%$, and the fraction of the term describing the interference with the nonresonant component is reduced to $1.4 \pm 1.0\%$. The χ_{c0} phase changes such that $\phi(\chi_{c0}) - \phi(\mathrm{NR}) = 0.29 \pm 0.20$.
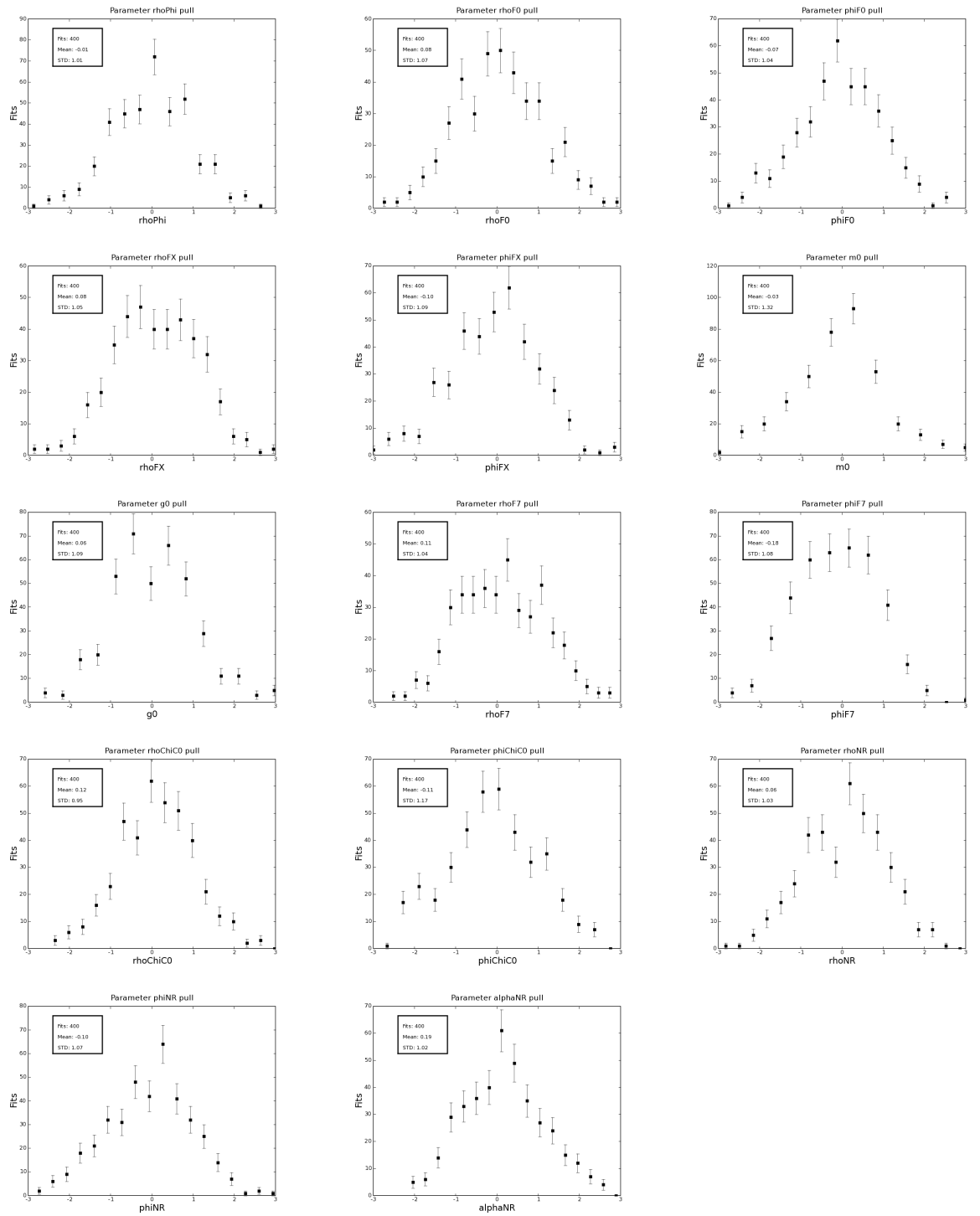
Figure 7.6: The distributions of the residuals obtained in the fit bias study.

Table 7.3: Fit results for CP violation parameters and symmetric 90%-confidence-level intervals for CP asymmetry.

	A	$(A_{\min}, A_{\max})_{90\%}$	$\phi^- - \phi^+$
ϕ	0.00 ± 0.08	$(-0.14, 0.14)$	-0.67 ± 0.28
$f_0(980)$	-0.31 ± 0.25	$(-0.72, 0.12)$	-0.20 ± 0.16
$X_0(1550)$	-0.04 ± 0.07	$(-0.17, 0.09)$	0.02 ± 0.15
$f_0(1710)$	0.0 ± 0.5	$(-0.66, 0.74)$	-0.07 ± 0.38
χ_{c0}^{I}	0.19 ± 0.18	$(-0.09, 0.47)$	0.7 ± 0.5
χ_{c0}^{II}	-0.03 ± 0.28	-	-0.4 ± 1.3
NR	0.02 ± 0.08	$(-0.14, 0.18)$	-

To check for possible fit bias, we fit 400 Monte Carlo–simulated data samples generated according to the nominal model of the best fit, and compute the residuals of the fit parameters defined as the difference between the value returned by the fit and the nominal value divided by the fit error. The distributions of the residuals are shown in Fig 7.6. In the limit or large statistics and parabolic Gaussian errors, the residuals are expected to have a normal distribution $N(0, 1)$. Table 7.2 gives the means and the standard deviations, (μ, σ), of the distributions of the residuals, which are all close to their nominal values.

To look for possible direct CP violation, we extend the isobar model by defining charge-dependent production coefficients as in Eq. (6.14) and use the log-likelihood of Eq. (6.30). As there is freedom to choose the overall phase for each component, we fixed the phases of the nonresonant contribution to zero for both charges. The results of the fits are summarized in Table 7.3. For the χ_{c0} component we give the results for both solutions from the leading doublet. Table 7.3 also gives symmetric 90%-confidence-level intervals around the nominal CP asymmetry value estimated by fitting Monte Carlo–simulated samples generated according to the parameterized model of the nominal asymmetry fit. All asymmetries A and phase differences $\phi^- - \phi^+$ are consistent with zero.

7.2 Partial-wave analysis

We further study the nature of the dominant S-wave component by considering the interference between the low-mass and the high-mass scattering amplitudes in the region $m_{23} \in (1.1, 1.8)\,\text{GeV}/c^2$,

$m_{13} > 2\,\mathrm{GeV}/c^2$. The matrix element is modeled as

$$\mathcal{M} = \frac{\rho_S(s_{23})}{\sqrt{2}}e^{i\phi_S(s_{23})} + \frac{\rho_{\mathrm{NR}}}{\sqrt{2}}e^{-\alpha s_{13}}, \tag{7.2}$$

where ρ_S and ϕ_S are taken to be constant within each bin of the s_{23} variable and the nonresonant amplitude parameterization is taken from the fit to the high-mass region. The partial-wave expansion truncated at the S-wave describes the data adequately; the magnitude of the S-wave in each bin is readily determined. Because of the mass dependence of the nonresonant component, the phase of the S-wave can also be determined, albeit with a sign ambiguity and rather large errors for bins with a small number of entries or small net variation of the nonresonant component.

The results are shown in Fig. 7.7, with the S-wave component of the isobar-model fit overlaid for comparison. Continuity requirements allow us to identify two possible solutions for the phase; the solution labeled by black squares is consistent with a rapid counterclockwise motion in the Argand plot around $m(K^+K^-) = 1.55\,\mathrm{GeV}/c^2$, which is accomodated in the isobar model as the contribution of the $X_0(1550)$.

Isospin symmetry relates the measurements in $B^\pm \to K^\pm K^\pm K^\mp$ and $B^0 \to K^+K^-K_S^0$ [72]. Our results for the K^+K^- S-wave can therefore be used to estimate a potentially significant source of uncertainty in the measurements of $\sin 2\beta$ in $B^0 \to \phi(1020)K_S^0$ [73, 74] due to the contribution of a CP-even S-wave amplitude. We perform a partial-wave analysis in the region $m_{23}(K^+K^-) \in (1.013, 1.027)\,\mathrm{GeV}/c^2$, modeling the matrix element as a sum of an S-wave and a P-wave:

$$\mathcal{M} = \frac{\rho_S}{\sqrt{2}} + \frac{\rho_P(s_{23})}{\sqrt{2}}e^{i\phi_P(s_{23})}\cos\theta_{13}, \tag{7.3}$$

where the S-wave is taken to be constant over the small region of phase space considered. The fit results for the P-wave are shown in Fig. 7.8. Because the phase of the S-wave is taken to be constant, there is a twofold ambiguity in the sign of the P-wave phase. We assign the data points in Fig. 7.8 to two solutions, one labeled by black squares and another labeled by white squares, using continuity requirements. The superimposed curve corresponds to a fit with a Breit-Wigner
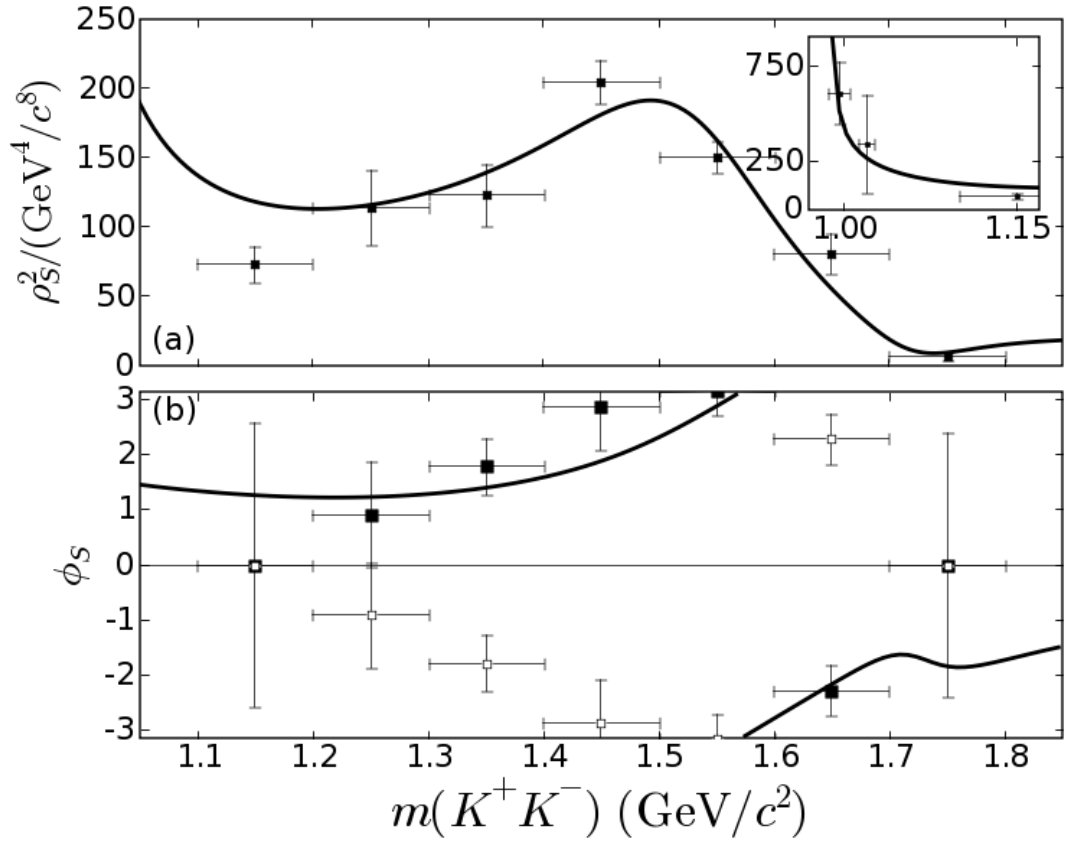
Figure 7.7: The results of the partial-wave analysis of the K^+K^- S-wave: (a) magnitude squared, (b) phase. The discrete ambiguities in the determination of the phase give rise to two possible solutions labeled by black and white squares. The curves correspond to the S-wave component from the isobar-model fit. The inset shows the evidence of a threshold enhancement from the fits of the S-wave in the vicinity of the K^+K^- threshold and in the region around the $\phi(1020)$ resonance.
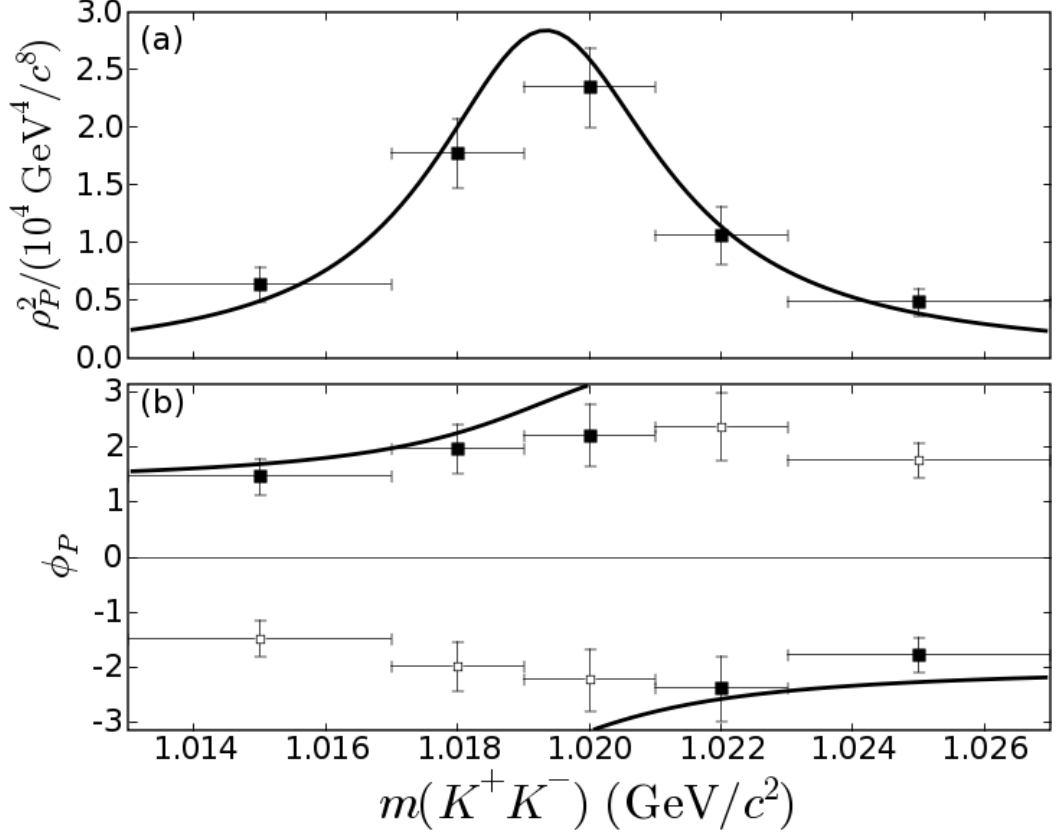
Figure 7.8: The results of the partial-wave analysis in the $\phi(1020)$ region for the P-wave: (a) magnitude squared, (b) phase. The discrete ambiguities in the determination of the phase give rise to two possible solutions labeled by black and white squares. The curve corresponds to a Breit-Wigner fit of the $\phi(1020)$ resonance.

parameterization of the ϕ resonance. For the S-wave we get $\rho_S^2 = (3.4 \pm 2.5) \times 10^2 \, \text{GeV}^{-4} c^8$ and compute its fraction in this region using Eq. (6.10) to be $(9 \pm 6)\%$.

We also consider the region $2m_{K^+} < m(K^+K^-) < 1.006 \, \text{GeV}/c^2$, in the immediate vicinity of the K^+K^- threshold. The contribution of the $\phi(1020)$ resonance tail in this region is suppressed by the centrifugal barrier and is estimated to be smaller than 10%. We fit $\rho_S^2 = (6.1 \pm 1.6) \times 10^2 \, \text{GeV}^{-4} c^8$ for the magnitude of the S-wave in this region. The fits in the vicinity of the K^+K^- threshold and in the region around the $\phi(1020)$ resonance indicate a threshold enhancement of the S-wave, which is accommodated in the isobar model by the contribution of the $f_0(980)$ resonance as shown in the inset of Fig. 7.7.

Chapter 8

Systematic Uncertainties

In this chapter we evaluate the systematic uncertainties for the overall braching fraction and asymmetry, and the fit fractions, phase differences, and direct CP violation parameters of the isobar-model fit.

8.1 Sources of systematic uncertainties

We use statistical inference to estimate the parameters of the underlying physics model from the observable quantities meausured by the subsystems of the *BABAR* detector. Our knowledge of the parameters of the signal model, our estimates of the background processes and our parameterization of the detector response have by necessity a limited precision, giving rise to systematic uncertainties on the values of the measured parameters. We consider the following sources of systematic uncertainty:

- **Tracking efficiency.**

  We determine the tracking efficiency using a Monte Carlo–simulation of the detector response adjusted by correction factors derived from data control samples. The correction factors have been evaluated by the *BABAR* Tracking Task Force [47] as functions of the measured track momentum vector and the event track multiplicity with an associated overall uncertainty of 0.8% per track. A conservative assumption of fully correlated tracking uncertainties gives a tracking efficiency uncertainty of 2.4%.

- **Particle identification efficiency.**

  We model the performance of the particle identification algorithms using a Monte Carlo simulation of the detector response adjusted by correction factors derived from data control samples. The correction factors have been evaluated by the *BABAR* Particle ID Group as functions of the measured track momentum. We determine the overall particle identifcation efficiency uncertainty independently using data control samples in Section 8.2.

- **Charge asymmetry in tracking and particle identification.**

  The overall efficiency and its associated uncertainty cancel out in the determination of CP asymmetries. In this analysis, we have assumed equal selection efficiencies for both charges. The tracking and particle identification efficiency can however be charge dependent, e.g., due to the difference in the strong-interaction cross-sections for charged kaons interacting with the detector material. Charge-dependent efficiencies can be defined as

$$\epsilon_\pm \equiv \epsilon(1 \mp A_\epsilon),$$

  where ϵ is the average efficiency, and A_ϵ is the efficiency charge asymmetry. A measurement of CP asymmetry is given by:

$$A = \frac{N_-\epsilon_- - N_+\epsilon_+}{N_+\epsilon_+ + N_-\epsilon_-}$$

  where $N_\pm$ be the number of $B^\pm$ decays produced, and A_0 is the CP asymmetry calculated assuming $A_\epsilon = 0$. For $A_0 A_\epsilon \ll 1$,

$$A \approx A_0 + A_\epsilon.$$

  We evaluate possible efficiency asymmetry using control samples in Section 8.2 and assign an appropriate systematic error.

- **Selection efficiency.**

  The efficiency of the applied selection is estimated using Monte Carlo–simulated signal events.

We use a control sample to check the selection efficiency of the ΔE requirement for data and simulated events. The systematic uncertainties due to the efficiency parameterization are evaluated in Section 8.3.

- **Background estimates.**

  The systematic uncertainties in evaluation of the backgrounds due to non-signal B decays and $q\bar{q}$ continuum events are discussed in Section 8.4.

- **Resonance lineshapes.**

  In this analysis, we have neglected the uncertainties on the Dalitz plot coordinates of the selected events due to detector resolution. This approximation is not expected to affect the components of the isobar model that have an intrinsic scale of variation larger than the detector resolution, but can be important for the narrow ϕ and χ_{c0} resonances.

  The fit fractions, phase differences, and CP asymmetries of the individual components of the isobar model, while not being sensitive to the overall efficiency, do depend on the component amplitude parameterization used in the fit. In the case of the $X_0(1550)$ and the nonresonant component, the amplitude shape parameters are determined directly from the fit and the associated uncertainties are included in the statistical error. The parameters of the $f_0(980)$, $\phi(1020)$, $f_0(1710)$, and χ_{c0} resonances are fixed in the fit and the uncertainty in their parameters is included in the systematic error.

  The systematic uncertainties due to resolution effects and uncertainties in resonance parameters are evaluated in Section 8.5.

8.2 Control sample studies

$B^{\pm} \to D\pi^{\pm}$, $D \to K^{\pm}\pi^{\mp}$ decays are produced via the charmed tree cascade of Fig. 8.1 and are observed in the $K^{\pm}\pi^{\pm}\pi^{\mp}$ final state. We perform a dedicated selection by considering triplets of charged tracks with net unit charge. One of the same-charge tracks is assigned a kaon hypothesis; the two other tracks are each assigned a pion hypothesis. The candidates with $m(K^{\pm}\pi^{\mp}) \in$
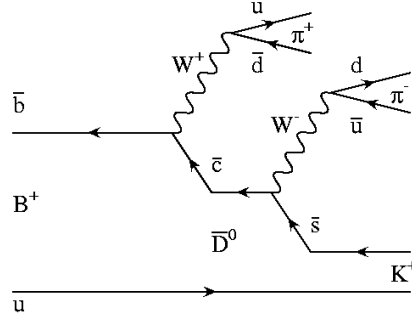
Figure 8.1: Charmed tree cascade.

Figure 8.2: The $m(K^{\pm}\pi^{\mp})$, m_{ES}, ΔE, and neural network output distributions for the selected $B^{\pm} \to D\pi^{\pm}$ control sample events.
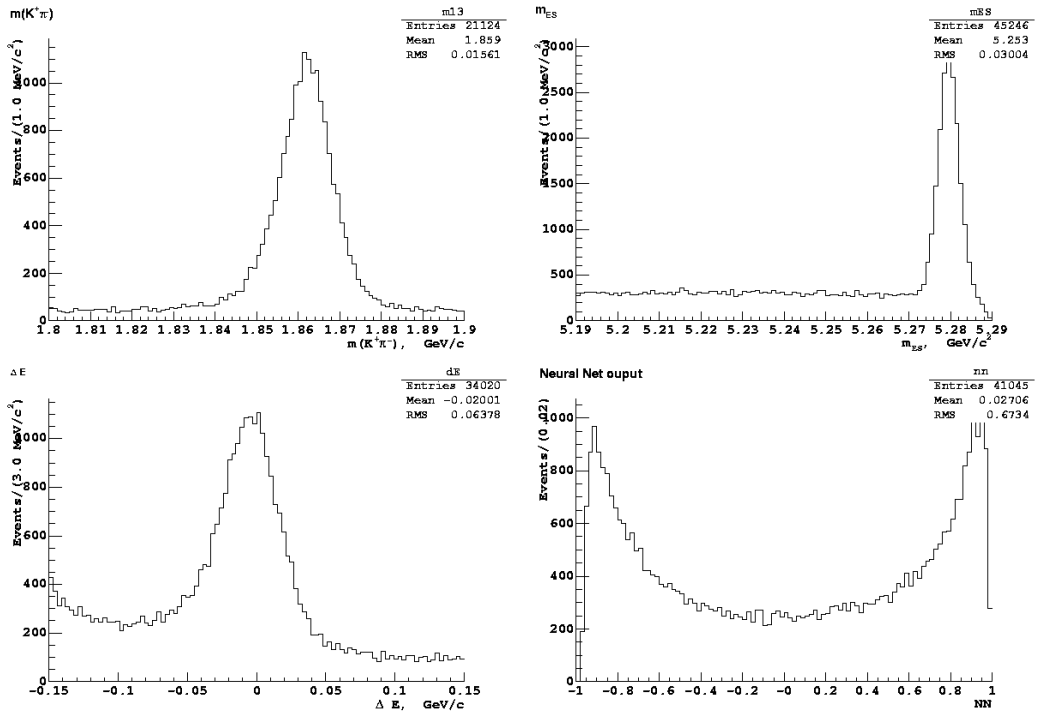
Figure 8.3: The ΔE distribution for $B^\pm \to D\pi^\pm$, $D \to K^\pm\pi^\mp$ control sample events in data (left); for simulated events (center); and a fit to the data using shifted histogram obtained from Monte Carlo simulation to model the signal peak (right).
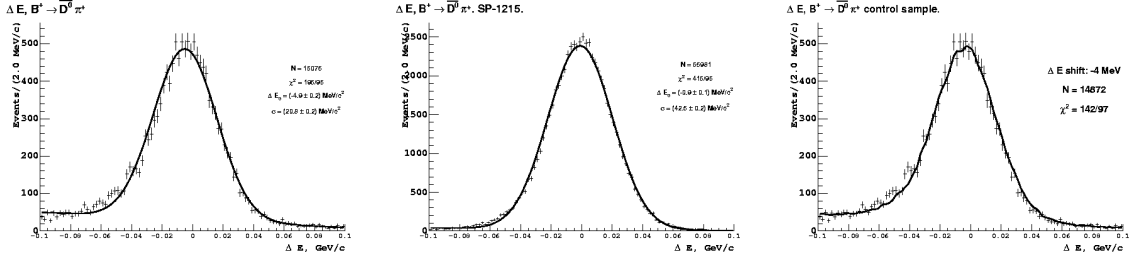
$(1.80, 1.90)\,\mathrm{GeV}/c^2$ are retained. No particle identification requirements are applied. The distributions of the $m(K^\pm\pi^\mp)$ invariant mass, m_{ES}, ΔE, and the output of the neural network in Fig. 8.2 all show a clear signal peak. To further improve the signal purity, we require $m(K^\pm\pi^\mp) \in (1.85, 1.88)\,\mathrm{GeV}/c^2$, $m_{\mathrm{ES}} > 5.27\,\mathrm{GeV}/c^2$, $|\Delta E| < 50\,\mathrm{MeV}$, the neural network output greater than 0.4, and remove the contribution from $B^\pm \to K^\pm J/\psi$ decays by vetoing the region $m(\pi^+\pi^-) \in (3.08, 3.12)\,\mathrm{GeV}/c^2$. The final sample purity is estimated to be 95%. The same selection is repeated for Monte Carlo–simulated $B^\pm \to D\pi^\pm$ events.

Backgrounds are estimated and subtracted by extrapolation from the m_{ES} sideband. After background subtraction, the number of $B^\pm$ candidates is $n_\pm = 6130/6277$; the number of kaon candidates that satisfy the kaon identification algorithm is $n_{K\pm} = 5316/5461$; and the number of pion candidates that fail the kaon identification is $n_{\pi\pm} = 11678/11663$.

We use the $B^\pm \to D\pi^\pm$ control sample to compare the shape of the ΔE distribution between data and simulated events (Fig. 8.3). We fit both distributions by a sum of a Gaussian, representing the signal, and a first-order polynomial, representing the background. In both cases the Gaussian does not describe the low side of the peak adequately. The width of the peak is similar in both cases, but the peak position for data is shifted by about $-5\,\mathrm{MeV}$. The fit is improved significantly when we use a histogram of the ΔE distribution of simulated events shifted by $-4\,\mathrm{MeV}$ to describe the signal peak. Using simulated events we evaluate that a $-5\,\mathrm{MeV}$ shift in the ΔE distribution would reduce the selection efficiency for the selection requirement $|\Delta E| < 40\,\mathrm{MeV}$ by 1%.

Figure 8.4: The $m(\pi^+\pi^-)$, m_{ES}, ΔE, and neural network output distributions for the selected $B^\pm \to K^\pm J/\psi$ control sample events.
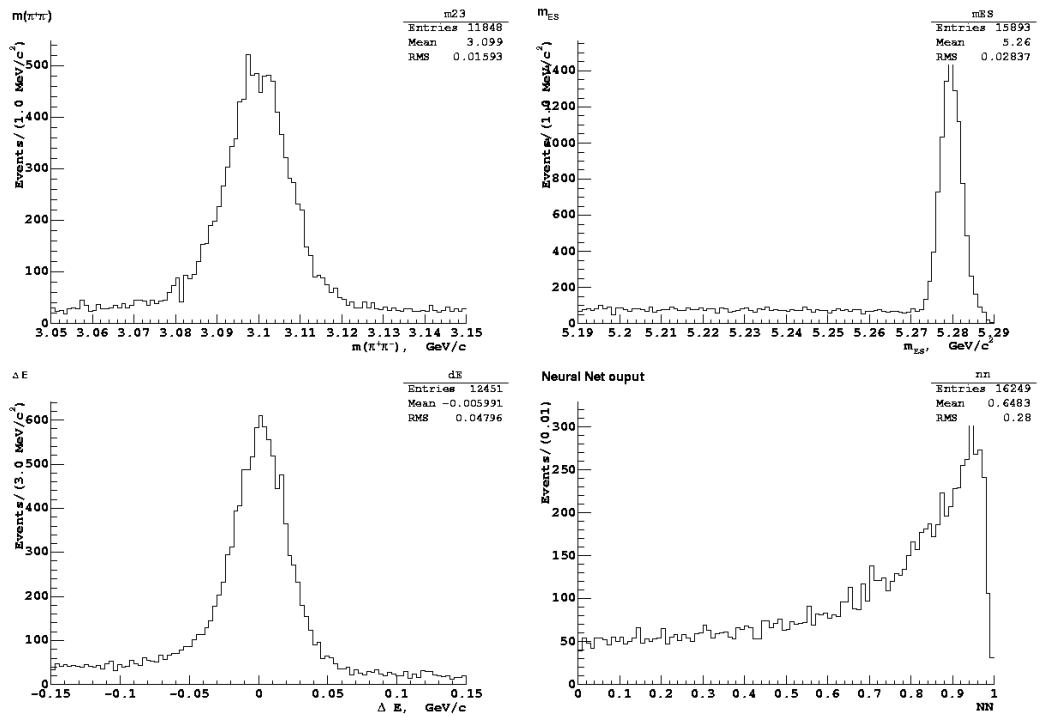
Table 8.1: Kaon and pion identification efficiencies and their ratios in control samples for data and Monte Carlo–simulated events.

Mode	ϵ_K	ϵ_K^{MC}	$\epsilon_K/\epsilon_K^{\mathrm{MC}}$	ϵ_π	$\epsilon_\pi^{\mathrm{MC}}$	$\epsilon_\pi/\epsilon_\pi^{\mathrm{MC}}$
$B^\pm \to DK^+$	0.869 ± 0.003	0.874	0.994 ± 0.003	0.941 ± 0.002	0.950	0.991 ± 0.002
$B^\pm \to K^+ J/\psi$	0.899 ± 0.003	0.904	0.994 ± 0.004	-	-	-

Table 8.2: Tracking and particle identification efficiency asymmetries in data control samples.

Mode	A	A_K	A_π
$B^\pm \to DK^+$	0.01 ± 0.01	0.001 ± 0.004	0.000 ± 0.002
$B^\pm \to K^+ J/\psi$	0.00 ± 0.01	0.001 ± 0.004	-

$B^\pm \to K^\pm J/\psi$, $J/\psi \to \ell^+\ell^-$ decays form another high-statistics control sample. We perform a dedicated selection by considering triplets of charged tracks with net unit charge. One of the same-charge tracks is assigned a kaon hypothesis, the two other tracks are each assigned a pion hypothesis. The candidates with $m(\pi^+\pi^-) \in (3.05, 3.15)\,\mathrm{GeV}/c^2$ are retained. No particle identification requirements are applied. The distributions of the $m(\pi^+\pi^-)$ invariant mass, m_{ES}, ΔE and the output of the neural network in Fig. 8.4 all show a clear signal peak. To further improve the signal purity we require $m(\pi^+\pi^-) \in (3.08, 3.12)\,\mathrm{GeV}/c^2$, $m_{\mathrm{ES}} > 5.27\,\mathrm{GeV}/c^2$, $|\Delta E| < 50\,\mathrm{MeV}$, the neural network output greater than 0.4, and remove the contribution from $B^\pm \to DK^\pm$ decays by vetoing the region $m(K^\pm\pi^\mp) \in (1.8, 1.9)\,\mathrm{GeV}/c^2$. The final sample purity is estimated to be 94%. The same selection is repeated for Monte Carlo–simulated $B^\pm \to K^\pm J/\psi$ events. Backgrounds are estimated and subtracted by extrapolating the event counts from the m_{ES} sideband. After background subtraction, the number of $B^\pm$ candidates is $n_\pm = 3612/3621$ and the number of kaon candidates that satisfy the kaon identification algorithm is $n_{K^\pm} = 3245/3259$.

Table 8.1 shows the kaon and pion identification efficiencies and their ratios in the control samples for data and simulated MC events. Table 8.2 shows the tracking and particle identification efficiency asymmetries in data control samples.

Based on the control sample studies described above, we assign a 0.5% systematic uncertainty per kaon and 1.0% per pion due to the uncertainty in the particle identification efficiency. For final states with an odd number of kaons, we assign a combined 1.5% systematic error due to possible

Table 8.3: Estimates of the systematic uncertainties for the fit fractions (upper triangle and diagonal), phase differences (lower triangle), and CP violation parameters due to the uncertainty in the signal efficiency parameterization.

	ϕ	$f_0(980)$	$X_0(1550)$	$f_0(1710)$	χ_{c0}	NR
ϕ	**0.1%**	0.0%	0.0%	0.0%	0.0%	0.0%
$f_0(980)$	0.01	**0.4%**	0.7%	0.1%	0.0%	1.2%
$X_0(1550)$	0.01	0.02	**0.9%**	0.4%	0.0%	1.5%
$f_0(1710)$	0.01	0.02	0.01	**0.1%**	0.0%	0.2%
χ_{c0}	0.02	0.02	0.01	0.01	**0.0%**	0.0%
NR	0.01	0.01	0.01	0.01	0.01	**1.0%**
A	0.0%	0.5%	0.1%	0.5%	0.3%	0.2%
$\phi^+ - \phi^-$	0.01	0.01	0.00	0.01	0.01	-

kaon charge asymmetries in kaon tracking and particle ID. We assign a 1% systematic uncertainty due to the $-5\,\mathrm{MeV}$ shift in the ΔE distribution of signal events observed in the data.

8.3 Systematic uncertainty in efficiency parameterization

Signal efficiency is parameterized as a binned histogram with efficiency in each bin determined based on the number of simulated signal events that pass the selection criteria. We fluctuate the efficiency according to its statistical error and rerun the fit. This procedure is repeated 100 times; we take the standard deviation of the fit results as an estimate of the systematic uncertainties (Table 8.3). The uncertainty on the overall branching fraction is 0.2%. No significant change in the overall CP asymmetry is observed.

8.4 Systematic uncertainty in background estimates

The uncertainty on the contribution of B backgrounds is evaluated by combining in quadrature the uncertainty on the values of branching fractions for individual decay modes with the statistical uncertainty due to limited sizes of simulated B background samples. We vary the bin contributions of the B backgrounds by their uncertainties and rerun the fit. This procedure is repeated 100 times; we take the standard deviation of the fit results as an estimate of the systematic uncertainties (Table 8.4). The uncertainty on the overall branching fraction is 0.6%. No significant change in the

Table 8.4: Estimates of the systematic uncertainties for the fit fractions (upper triangle and diagonal), phase differences (lower triangle), and CP violation parameters due to the uncertainty in the modeling of B backgrounds.

	ϕ	$f_0(980)$	$X_0(1550)$	$f_0(1710)$	χ_{c0}	NR
ϕ	**0.1%**	0.0%	0.0%	0.0%	0.0%	0.1%
$f_0(980)$	0.02	**1.1%**	1.7%	0.5%	0.0%	3.3%
$X_0(1550)$	0.04	0.04	**3.0%**	2.4%	0.0%	3.4%
$f_0(1710)$	0.07	0.07	0.04	**0.6%**	0.0%	1.2%
χ_{c0}	0.04	0.03	0.03	0.06	**0.0%**	0.0%
NR	0.03	0.02	0.02	0.06	0.02	**3.1%**
A	0.1%	1.8%	0.7%	4.8%	0.6%	0.6%
$\phi^+ - \phi^-$	0.01	0.01	0.01	0.05	0.02	-

Table 8.5: Estimates of the systematic uncertainties for the fit fractions (upper triangle and diagonal), phase differences (lower triangle), and CP violation parameters due to the uncertainty in the sideband extrapolation $q\bar{q}$ background subtraction.

	ϕ	$f_0(980)$	$X_0(1550)$	$f_0(1710)$	χ_{c0}	NR
ϕ	**0.0%**	0.0%	0.0%	0.0%	0.0%	0.0%
$f_0(980)$	0.01	**0.3%**	0.0%	0.1%	0.0%	1.0%
$X_0(1550)$	0.01	0.01	**0.5%**	0.0%	0.0%	0.2%
$f_0(1710)$	0.01	0.00	0.01	**0.1%**	0.0%	0.2%
χ_{c0}	0.00	0.01	0.01	0.01	**0.0%**	0.0%
NR	0.00	0.01	0.00	0.01	0.00	**1.1%**
A	0.1%	0.7%	0.1%	1.4%	0.7%	0.3%
$\phi^+ - \phi^-$	0.00	0.00	0.00	0.01	0.02	-

overall CP asymmetry is observed.

The estimates of $q\bar{q}$ continuum backgrounds have been obtained by sideband extrapolation as discussed in Section 4.3; we have used the central value of the background extrapolation coefficient, throughout. To evaluate the uncertainty in $q\bar{q}$ background subtraction, we vary the extrapolation coefficient by its uncertainty and take the changes in the values of the fit fractions, phase differences, and CP violation parameters as estimates of respective systematic uncertainties (Table 8.5).

8.5 Systematic uncertainty in resonance lineshapes

The observed width of narrow resonances can be significantly larger than the natural width due to detector resolution. Fig. 8.5 shows the distribution of the di-kaon invariant mass near the mass of the ϕ resonance for data and simulated $B^\pm \rightarrow K^\pm \phi$ events selected in the signal region. The
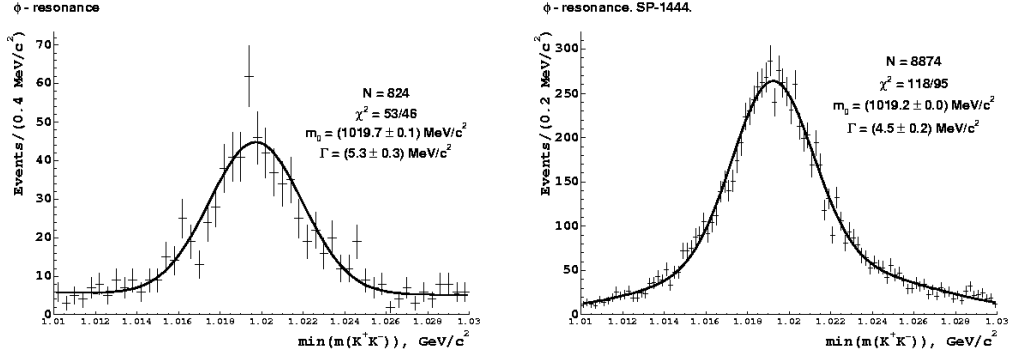
Figure 8.5: Di-kaon invariant mass distribution near the ϕ resonance for candidates selected in the signal region for data (left) and simulated $B^{\pm} \to K^{\pm}\phi$ events (right). Γ is the width of the Gaussian at half maximum.

Table 8.6: Estimates of the systematic uncertainties for the fit fractions (upper triangle and diagonal), phase differences (lower triangle), and CP violation parameters due to neglecting detector resolution effects and the uncertainty in the Blatt-Weisskopf interaction radius for the ϕ resonance.

	ϕ	$f_0(980)$	$X_0(1550)$	$f_0(1710)$	χ_{c0}	NR
ϕ	**0.8%**	0.1%	0.2%	0.0%	0.0%	0.4%
$f_0(980)$	0.05	**2.8%**	3.7%	0.2%	0.1%	8.1%
$X_0(1550)$	0.02	0.04	**2.4%**	0.7%	0.0%	1.6%
$f_0(1710)$	0.02	0.03	0.01	**0.1%**	0.0%	0.3%
χ_{c0}	0.02	0.04	0.00	0.01	**0.0%**	0.1%
NR	0.03	0.03	0.01	0.01	0.01	**5.0%**
A	0.9%	6.5%	0.3%	3.5%	1.3%	2.7%
$\phi^+ - \phi^-$	0.03	0.04	0.04	0.06	0.04	-

data distribution is fitted with a sum of a Gaussian and a first-order polynomial. The width of the distribution, estimated as the width of the Gaussian at half maximum, is $\Gamma = 5.3 \pm 0.3$ MeV. The simulated events distribution is fitted by a sum of two Gaussians. The width of the distribution, estimated as the width of the narrow Gaussian at half maximum, is $\Gamma = 4.5 \pm 0.2$ MeV. In both cases, the distribution widths are somewhat larger than the natural width of the resonance, $\Gamma(\phi) = 4.2$ MeV. To estimate the effect of neglecting the detector resolution, we change the width of the ϕ resonance to 5.2 MeV and rerun the fit.

In our nominal fit, we have used $R = 4\,\mathrm{GeV}^{-1}$ for the Blatt-Weisskopf interaction range parameter. When the interaction range is allowed to float in the fit, we get $R = 4.17 \pm 0.39\,\mathrm{GeV}^{-1}$, consistent with the value used in the nominal fit. To estimate the systematic uncertainty due to the choice of the interaction range, we repeat the fit with $R = 3.5\,\mathrm{GeV}^{-1}$.
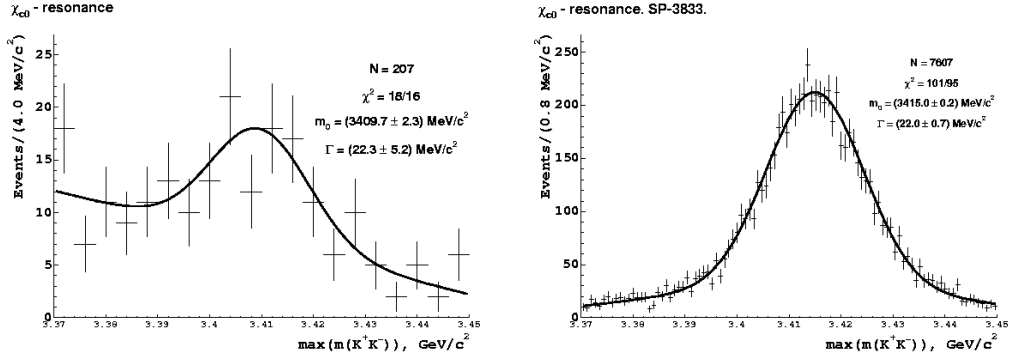
Figure 8.6: Di-kaon invariant mass distribution near the χ_{c0} resonance for candidates selected in the signal region for data (left) and simulated $B^{\pm} \to K^{\pm}\chi_{c0}$ events (right). Γ is the width of the Gaussian at half maximum.

Table 8.7: Estimates of the systematic uncertainties for the fit fractions (upper triangle and diagonal), phase differences (lower triangle), and CP violation parameters due to neglecting detector resolution effects for the χ_{c0} resonance.

	ϕ	$f_0(980)$	$X_0(1550)$	$f_0(1710)$	χ_{c0}	NR
ϕ	**0.0%**	0.0%	0.1%	0.0%	0.1%	0.0%
$f_0(980)$	0.01	**0.7%**	1.5%	0.4%	0.5%	1.4%
$X_0(1550)$	0.03	0.04	**2.9%**	1.1%	0.5%	3.2%
$f_0(1710)$	0.03	0.04	0.00	**0.2%**	0.1%	0.5%
χ_{c0}	0.11	0.12	0.08	0.08	**0.2%**	1.9%
NR	0.02	0.03	0.01	0.01	0.09	**0.8%**
A	0.0%	2.9%	0.2%	1.9%	3.8%	1.1%
$\phi^+ - \phi^-$	0.02	0.01	0.01	0.00	0.17	-

We combine the changes in the values of the fit fractions, phase differences, and CP violation parameters in quadrature to get estimates of respective systematic uncertainties (Table 8.6).

Fig 8.6 shows the distribution of the di-kaon invariant mass in the region near the mass of the χ_{c0} resonance for data and simulated $B^{\pm} \to K^{\pm}\chi_{c0}$ events selected in the signal region. The data distribution is fitted with a sum of a Gaussian and a first-order polynomial. The width of the distribution, estimated as the width of the Gaussian at half maximum, is $\Gamma = 22.3 \pm 5.2\,\text{MeV}$. The distribution of simulated events is fitted by a sum of two Gaussians. The width of the distribution, estimated as the width of the narrow Gaussian at half maximum, is $\Gamma = 22.0 \pm 0.7\,\text{MeV}$. In both cases due to resolution effects the distribution widths are considerably larger than the natural width of the resonance, $\Gamma(\chi_{c0}) = 10.1\,\text{MeV}$. To estimate the effect of neglecting the detector resolution we change the width of the χ_{c0} resonance to $22.\,\text{MeV}$ and rerun the fit. We take the changes in

Table 8.8: Estimates of the systematic uncertainties for the fit fractions (upper triangle and diagonal), phase differences (lower triangle), and CP violation parameters due to to the uncertainty in the $f_0(980)$ lineshape.

	ϕ	$f_0(980)$	$X_0(1550)$	$f_0(1710)$	χ_{c0}	NR
ϕ	**0.1%**	0.0%	0.0%	0.0%	0.0%	0.1%
$f_0(980)$	0.08	**3.2%**	5.5%	0.6%	0.1%	10.4%
$X_0(1550)$	0.03	0.09	**2.5%**	1.0%	0.0%	3.0%
$f_0(1710)$	0.04	0.09	0.01	**0.2%**	0.0%	0.5%
χ_{c0}	0.04	0.09	0.01	0.01	**0.0%**	0.1%
NR	0.03	0.07	0.02	0.02	0.02	**5.8%**
A	0.2%	2.8%	0.6%	4.8%	0.2%	0.4%
$\phi^+ - \phi^-$	0.01	0.01	0.02	0.01	0.01	-

Table 8.9: Estimates of the systematic uncertainties for the fit fractions (upper triangle and diagonal), phase differences (lower triangle), and CP violation parameters due to to the uncertainty in the $f_0(1710)$ lineshape.

	ϕ	$f_0(980)$	$X_0(1550)$	$f_0(1710)$	χ_{c0}	NR
ϕ	**0.0%**	0.0%	0.1%	0.1%	0.0%	0.1%
$f_0(980)$	0.01	**0.4%**	1.2%	0.8%	0.0%	1.6%
$X_0(1550)$	0.02	0.02	**2.9%**	3.0%	0.0%	3.5%
$f_0(1710)$	0.10	0.11	0.09	**0.4%**	0.0%	2.1%
χ_{c0}	0.01	0.01	0.01	0.10	**0.0%**	0.0%
NR	0.00	0.01	0.01	0.10	0.00	**1.9%**
A	0.1%	0.7%	0.1%	1.6%	0.4%	0.4%
$\phi^+ - \phi^-$	0.01	0.01	0.01	0.03	0.01	-

the values of fit fractions, phase differences, and CP violation parameters as estimates of respective systematic uncertainties (Table 8.7).

In this analysis we have used the parameters of the $f_0(980)$ resonance measured by the BES collaboration [65], the most reliable measurement to date. We vary the parameters individually by their combined statistical and systematic uncertainties added in quadrature and repeat the fit. We combine the changes in the values of the fit fractions, phase differences, and CP violation parameters in quadrature to get estimates of respective systematic uncertainties (Table 8.8).

The width of the $f_0(1710)$ resonance is $\Gamma(f_0(1710)) = 138 \pm 9\,\mathrm{MeV}$ [14]. To estimate the sensitivity of our results to this parameter we change it to $147\,\mathrm{MeV}$ and repeat the fit. We take the changes in the values of fit fractions, phase differences, and CP violation parameters as estimates of respective systematic uncertainties (Table 8.9).

Table 8.10: Sources of systematic uncertainty for the overall branching fraction and asymmetry.

	$\mathcal{B}$	A
Tracking efficiency	2.4%	1.0%
Particle ID efficiency	1.5%	0.5%
Tracking + PID	3.9%	1.5%
ΔE shift	1.0%	-
B backgrounds	0.7%	-
Sideband extrapolation	1.4%	-
Signal efficiency	0.2%	-
$N(B^+B^-)$	1.1%	-
Total	4.5%	1.5%

8.6 Tensor resonances $f_2(1270)$ and $f_2'(1525)$

We do not expect a large contribution from the tensor resonance $f_2(1270)$. It is known to cou-ple preferentially to $\pi\pi$ and the measured branching fraction $\mathcal{B}(B^\pm \rightarrow K^\pm f_2(1270), f_2(1270) \rightarrow \pi^+\pi^-) = (0.75 \pm 0.17 \pm 0.06) \times 10^{-6}$ [75] is small. The tensor resonance $f_2'(1525)$ is known to couple preferentially to $K\bar{K}$, and a strong $f_2'(1525) \rightarrow K\bar{K}$ signal has been observed in different production environments [65, 66, 76].

In this analysis we did not see any evidence of a low-mass D-wave in the partial-wave analysis of Section 7.2. We try including $f_2(1270)$ and $f_2'(1525)$ components in our isobar model, and get fit fractions $F(B^\pm \rightarrow K^\pm f_2(1270)) = (0.28 \pm 0.24)\%$ and $F(B^\pm \rightarrow K^\pm f_2'(1525)) = (0.08 \pm 0.10)\%$, consistent with zero. We thus do not observe a statistically significant contribution from the tensor resonances in $B^\pm \rightarrow K^\pm K^\pm K^\mp$.

8.7 Systematic uncertainty summary

Different sources of systematic uncertainty for the overall branching fraction and asymmetry are summarized in Table 8.10. As the uncertainties in the determination of the tracking and particle identification efficiencies may be correlated, we conservatively combine them linearly. All other uncertainties are added in quadrature. The systematic uncertainties for the overall branching fraction and asymmetry are dominated by the combined systematic uncertainty in tracking and particle

identification efficiencies.

For the fit fractions, phase differences, and CP violation parameters of the individual components of the isobar model, we combine all systematic uncertainties in quadrature, adding 2% in quadrature to all CP asymmetry uncertainties to account for possible charge asymmetry in tracking and particle identification for kaons.

Chapter 9

Results

Our final results for the total branching fraction is $\mathcal{B}(B^\pm \to K^\pm K^\pm K^\mp) = (35.2 \pm 0.9 \pm 1.6) \times 10^{-6}$, where the first error is statistical and the second is systematic. The fit fraction of the isobar-model terms that do not involve the χ_{c0} resonance is $(95.0 \pm 0.6 \pm 1.1)\%$ for the best fit, giving $\mathcal{B}(B^\pm \to K^\pm K^\pm K^\mp) = (33.5 \pm 0.9 \pm 1.6) \times 10^{-6}$ if intrinsic charm contributions are excluded. The total asymmetry is $A_{CP} = \frac{\mathcal{B}(B^- \to K^- K^- K^+) - \mathcal{B}(B^+ \to K^+ K^+ K^-)}{\mathcal{B}(B^\pm \to K^\pm K^\pm K^\mp)} = (-1.7 \pm 2.6 \pm 1.5)\%$. These results are in agreement with the Belle collaboration isobar-model Dalitz plot analysis result $\mathcal{B}(B^\pm \to K^\pm K^\pm K^\mp) = (30.6 \pm 1.2 \pm 2.3) \times 10^{-6}$ [19], and a previous inclusive *BABAR* measurement, $\mathcal{B}(B^\pm \to K^\pm K^\pm K^\mp) = (29.6 \pm 2.1 \pm 1.6) \times 10^{-6}$, $A_{CP}(B^\pm \to K^\pm K^\pm K^\mp) = 0.02 \pm 0.07 \pm 0.03$ [16]. In both cases, the branching fraction $\mathcal{B}(B^\pm \to K^\pm \chi_{c0}, \chi_{c0} \to K^+ K^-)$ was not included in the charmless total.

Table 9.1 gives the final results for the magnitudes of production coefficients, ρ; the matrix of the differences between the phases of the production coefficients, $\phi_{ij} = \phi_j - \phi_i$; the matrix of component fit fractions (Eq. 6.10) and interference term fractions (Eq. 6.12), F_{ij}; the component CP asymmetries, A, and their symmetric 90%-confidence-level intervals; the charge-dependent production coefficient phase differences for the individual components of the isobar model, $\delta\phi = \phi^- - \phi^+$; and the quasi-two-body branching fractions, $F_{ii} \times \mathcal{B}(B^\pm \to K^\pm K^\pm K^\mp)$.

Using $\mathcal{B}(\phi \to K^+ K^-) = 49.2 \pm 0.6\%$, we get $\mathcal{B}(B^\pm \to K^\pm \phi) = (8.4 \pm 0.7 \pm 0.7 \pm 0.1) \times 10^{-6}$, where the last error is due to the ϕ branching fraction uncertainty. The result is in good agreement with the Belle collaboration isobar-model Dalitz plot fit result, $\mathcal{B}(B^\pm \to K^\pm \phi) = (9.83 \pm 0.90 \pm 0.90) \times$

10^{-6} [19], and the result from a previous *BABAR* quasi-two-body analysis, $\mathcal{B}(B^\pm \to K^\pm \phi) = (10.0 \pm 0.9 \pm 0.5) \times 10^{-6}$ [17]. These measurements are in good agreement with the PQCD prediction and are on the higher side of the QCDF predictions in Table 2.1. Our asymmetry result for $\mathcal{B}(B^\pm \to K^\pm \phi)$ is in good agreement with the QCDF predictions.

The quasi-two-body branching fraction $\mathcal{B}(B^\pm \to K^\pm \chi_{c0}, \chi_{c0} \to K^+ K^-) = (1.10 \pm 0.20 \pm 0.09) \times 10^{-6}$ is in good agreement with the Belle collaboration isobar-model Dalitz plot fit result, $\mathcal{B}(B^\pm \to K^\pm \chi_{c0}, \chi_{c0} \to K^+ K^-) = (0.86 \pm 0.26 \pm 0.06) \times 10^{-6}$ [19], and the result from a previous *BABAR* quasi-two-body analysis, $\mathcal{B}(B^\pm \to K^\pm \chi_{c0}, \chi_{c0} \to K^+ K^-) = (1.1 \pm 0.2 \pm 0.1) \times 10^{-6}$ [18]. Using $\mathcal{B}(\chi_{c0} \to K^+ K^-) = (6.0 \pm 0.9) \times 10^{-3}$, we get $\mathcal{B}(B^\pm \to K^\pm \chi_{c0}) = (1.84 \pm 0.32 \pm 0.14 \pm 0.28) \times 10^{-4}$, where the last error is due to the χ_{c0} branching fraction uncertainty. This is in good agreement with the prediction based on intrinsic charm rescattering [6].

We combine our result, $\mathcal{B}(B^\pm \to K^\pm f_0(980), f_0(980) \to K^+ K^-) = (6.5 \pm 2.5 \pm 1.6)$, with the *BABAR* measurement, $\mathcal{B}(B^\pm \to K^\pm f_0(980), f_0(980) \to \pi^+ \pi^-) = (9.47 \pm 0.97 \pm 0.46) \times 10^{-6}$ and estimate $\mathcal{B}(B^\pm \to K^\pm f_0(980)) = (27 \pm 5 \pm 3) \times 10^{-6}$, where we have used isospin symmetry and combined statistical and systematic errors in quadrature. This value is significantly larger than the theoretical prediction of Ref. [5], where $f_0(980)$ was considered as a two-quark state. The discrepancy, mostly due to the large branching fraction of $f_0(980) \to K\bar{K}$, suggests that this simple quark model may not describe very well the structure of the $f_0(980)$ resonance. For the ratio of the partial branching fractions we get:

$$\frac{\mathcal{B}(B^\pm \to K^\pm f_0(980), f_0(980) \to K^+ K^-)}{\mathcal{B}(B^\pm \to K^\pm f_0(980), f_0(980) \to \pi^+ \pi^-)} = 0.69 \pm 0.32,$$

where we have combined the statistical and systematic errors in quadrature. This is consistent with 0.92 ± 0.07, the prediction that we obtain by evaluating the right-hand side of Eq. (7.1) using the $f_0(980)$ parameters measured by the BES collaboration [65].

In conclusion, we have measured the total branching fraction and the *CP* asymmetry in $B^\pm \to K^\pm K^\pm K^\mp$, which is in agreement with previous measurements. An isobar-model Dalitz plot fit

Table 9.1: Production coefficient magnitudes, phase differences, fit fractions, quasi-two-body branching fractions, and *CP* violation parameters of the individual components of the isobar model for the leading fit. The first error is statistical, the second is combined systematic.

	ρ	f₀(980)	X₀(1550)	f₀(1710)	χc0	NR
	1.66 ± 0.06	5.2 ± 1.0	8.2 ± 1.1	1.22 ± 0.34	0.437 ± 0.039	13.2 ± 1.4

ϕ_{ij} (rad.)	φ	φ	φ	φ	χc0	NR
φ	0	−2.51 ± 0.17 ± 0.11	−1.70 ± 0.27 ± 0.07	2.71 ± 0.35 ± 0.13	2.27 ± 0.35 ± 0.12	−2.99 ± 0.20 ± 0.06
f₀(980)	2.51 ± 0.17 ± 0.11	0	0.81 ± 0.25 ± 0.12	−1.07 ± 0.36 ± 0.17	−1.50 ± 0.33 ± 0.17	−0.48 ± 0.16 ± 0.08
X₀(1550)	1.70 ± 0.27 ± 0.07	−0.81 ± 0.25 ± 0.12	0	−1.88 ± 0.19 ± 0.09	−2.32 ± 0.22 ± 0.09	−1.29 ± 0.10 ± 0.04
f₀(1710)	−2.71 ± 0.35 ± 0.13	1.07 ± 0.36 ± 0.17	1.88 ± 0.19 ± 0.09	0	−0.44 ± 0.30 ± 0.13	0.59 ± 0.25 ± 0.11
χc0	−2.27 ± 0.35 ± 0.12	1.50 ± 0.33 ± 0.17	2.32 ± 0.22 ± 0.09	0.44 ± 0.30 ± 0.13	0	1.02 ± 0.23 ± 0.10
NR	2.99 ± 0.20 ± 0.06	0.48 ± 0.16 ± 0.08	1.29 ± 0.10 ± 0.04	−0.59 ± 0.25 ± 0.11	−1.02 ± 0.23 ± 0.10	0

F_{ij} × 100%	φ	φ	φ	φ	χc0	NR
φ	**11.8 ± 0.9 ± 0.8**	−0.94 ± 0.18 ± 0.11	−1.71 ± 0.36 ± 0.24	0.01 ± 0.10 ± 0.03	0.11 ± 0.02 ± 0.05	3.54 ± 0.38 ± 0.40
f₀(980)		**19 ± 7 ± 4**	53 ± 12 ± 7	−4.5 ± 2.9 ± 1.2	−0.9 ± 0.2 ± 0.5	−85 ± 21 ± 14
X₀(1550)			**121 ± 19 ± 6**	−30 ± 11 ± 4	−1.1 ± 0.3 ± 0.5	−140 ± 26 ± 7
f₀(1710)				**4.8 ± 2.7 ± 0.8**	−0.10 ± 0.07 ± 0.07	4 ± 6 ± 3
χc0					**3.1 ± 0.6 ± 0.2**	3.9 ± 0.4 ± 1.9
NR						**141 ± 16 ± 9**

Two-body $\mathcal{B}$	φ	φ	φ	φ	χc0	NR
$\mathcal{F} \times \mathcal{B} \times 10^6$	4.14 ± 0.32 ± 0.33	6.5 ± 2.5 ± 1.6	43 ± 6 ± 3	1.7 ± 1.0 ± 0.3	1.10 ± 0.20 ± 0.09	50 ± 6 ± 4

CP	φ	φ	φ	φ	χc0	NR
$\mathcal{A}$	0.00 ± 0.08 ± 0.02	−0.31 ± 0.25 ± 0.08	−0.04 ± 0.07 ± 0.02	0.0 ± 0.5 ± 0.1	0.19 ± 0.18 ± 0.05	0.02 ± 0.08 ± 0.04
$(\mathcal{A}_{min}, \mathcal{A}_{max})_{90\%}$	(−0.14, 0.14)	(−0.72, 0.12)	(−0.17, 0.09)	(−0.66, 0.74)	(−0.09, 0.47)	(−0.09, 0.18)
$\phi^- - \phi^+$	−0.67 ± 0.28 ± 0.05	−0.20 ± 0.16 ± 0.04	0.02 ± 0.15 ± 0.05	−0.07 ± 0.38 ± 0.08	0.7 ± 0.5 ± 0.2	-

and a partial-wave analysis of the K^+K^- S-wave show evidence of large contributions from a broad $X_0(1550)$ scalar resonance, a mass-dependent nonresonant component, and the $f_0(980)$ resonance. The quasi-two-body branching fractions for $\mathcal{B}(B^\pm \to K^\pm\phi, \ \phi \to K^+K^-)$ and $\mathcal{B}(B^\pm \to K^\pm\chi_{c0}, \ \chi_{c0} \to K^+K^-)$ are consistent with the previous measurements and with the theoretical expectations. We see evidence of a large $B^\pm \to K^\pm f_0(980)$ component in the $K^\pm K^\pm K^\mp$ final state and combined *BABAR* results for $B^\pm \to K^\pm f_0(980)$ are consistent, albeit with large errors, with the measurement of the ratio of the $f_0(980)$ coupling constants, g_K/g_π, by the BES collaboration [65]. We see no evidence of direct *CP* violation for the individual components of the isobar model.

One of the main highlights of this analysis is the complicated S-wave model that had to be used to fit the observed event distribution. The identification of the lowest-mass quark model pseudo-scalar meson nonet is still a subject of controversy. In addition to the usual di-quark states, speculative four-quark and glueball [13] interpretations have been suggested. Even the attribution of the well-known resonance $f_0(980)$ is uncertain, even less is known about the speculative σ resonance and other low-mass scalars: $f_0(1300)$, $f_0(1500)$, and $f_0(1710)$. In this analysis, as well as in the preceding analysis by the Belle collaboration [19], a broad scalar resonance, which we label $X_0(1550)$, had to be introduced to describe the observed event distribution. Evidence of a possible resonant S-wave contribution around $m(KK) = 1.5 - 1.6\,\text{GeV}$ has been reported previously [69, 70], but the attribution of the $X_0(1550)$ at this point is uncertain.

Finally, we had to use an ad hoc parameterization of the mass-dependent nonresonant component to achieve a good fit. A physics-based model successfully describing the data is clearly desirable, especially in view of the possibility of performing a partial-wave analysis by considering the interference between the low-mass K^+K^- S-wave and the mass-dependent nonresonant component. The published theoretical models [60, 61], surveyed in Section 6.5, have been found to be in disagreement with the experimental data.

Bibliography

[1] H.-Y. Cheng and K.-C. Yang, Phys. Rev. **D64**, 074004 (2001).

[2] D. Du, H. Gong, J. Sun, D. Yang, and G. Zhu, Phys. Rev. **D65**, 094025 (2002).

[3] M. Beneke and M. Neubert, Nucl. Phys. **B675**, 333 (2003).

[4] C. Chen, Y. Keum, and H. Li, Phys. Rev. **D64**, 112002 (2001).

[5] H.-Y. Cheng and K.-C. Yang, Phys. Rev. **D71**, 054020 (2005).

[6] P. Colangelo, F. de Fazio, and T. Pham, Phys. Lett. **B542**, 71 (2002).

[7] D. Du, J. Sun, D. Yang, and G. Zhu, Phys. Rev. **D67**, 014023 (2003).

[8] R. Aleksan, P.-F. Giraud, V. Morénas, O. Pène, and A. Safir, Phys. Rev. **D67**, 094019 (2003).

[9] N. de Groot, W. Cottingham, and I. Wittingham, Phys. Rev. **D68**, 113005 (2003).

[10] H. Lipkin, Y. Nir, H. Quinn, and A. Snyder, Phys. Rev. **D44**, 1454 (1991).

[11] A. Snyder and H. Quinn, Phys. Rev. **D48**, 2139 (1993).

[12] Y. Grossman, Z. Ligeti, Y. Nir, and H. Quinn, Phys. Rev. **D68**, 015004 (2003).

[13] P. Minkowski and W. Ochs, Eur. Phys. Journal. **C39**, 71 (2005).

[14] S. Eidelman et al., Phys. Lett. **B592** (2004), and 2005 partial update for the 2006 edition available on the PDG WWW pages, URL `http://pdg.lbl.gov/`.

[15] R. Briere et al. (CLEO Collaboration), Phys. Rev. Lett. **86**, 3718 (2001).

[16] B. Aubert et al. (*BABAR* Collaboration), Phys. Rev. Lett. **91**, 051801 (2003).

[17] B. Aubert et al. (*BABAR* Collaboration), Phys. Rev. **D69**, 011102 (2004).

[18] B. Aubert et al. (*BABAR* Collaboration), Phys. Rev. **D69**, 071103 (2004).

[19] A. Garmash et al. (Belle Collaboration), Phys. Rev. **D71**, 092003 (2005).

[20] M. Kobayashi and T. Maskawa, Prog. Theor. Phys. **49**, 652 (1973).

[21] L. Wolfenstein, Phys. Rev. Lett. **51**, 1945 (1983).

[22] N. Cabibbo, Phys. Rev. Lett. **10**, 531 (1963).

[23] M. Bander, D. Silverman, and A. Soni, Phys. Rev. Lett. **43**, 242 (1979).

[24] C.-W. Chiang, M. Gronau, Z. Luo, J. Rosner, and D. Suprun, Phys. Rev. **D69**, 034001 (2004).

[25] M. Bauer, B. Stech, and M. Wirbel, Z. Phys. **C34**, 103 (1987).

[26] M. Neubert and B. Stech, Adv. Ser. Direct. High Energy Phys. **15**, 294 (1998).

[27] D. Melikhov and B. Stech, Phys. Rev. **D62**, 014006 (2000).

[28] B. Aubert et al. (*BABAR* Collaboration), Phys. Rev. **D72**, 072003 (2005).

[29] M. Beneke, G. Buchalla, M. Neubert, and C. T. Sachrajda, Phys. Rev. Lett. **83**, 1914 (1999).

[30] M. Beneke, G. Buchalla, M. Neubert, and C. T. Sachrajda, Nucl. Phys. **B591**, 313 (2000).

[31] Y. Keum, H. Li, and A. Sanda, Phys. Rev. **D63**, 054008 (2001).

[32] M. Ciuchini, E. Franco, G. Martinelli, and L. Silvestrini, Nucl. Phys. **B501**, 271 (1997).

[33] C. Isola, M. Ladisa, T. Pham, and P. Santorelli, Phys. Rev. **D64**, 014029 (2001).

[34] S. Brodsky and S. Garnder, Phys. Rev. **D65**, 054016 (2002).

[35] M. Ciuchini, E. Franco, G. Martinelli, M. Pierini, and L. Silvestrini, Phys. Lett. **B515**, 33 (2001).

[36] Y.-H. Chen, H.-Y. Cheng, B. Tseng, and K.-C. Yang, Phys. Rev. **D60**, 094014 (1999).

[37] D. Du, H. Gong, J. Sun, D. Yang, and G. Zhu, Phys. Rev. **D66**, 079904 (2002).

[38] W. Kozanecki, Nucl. Instrum. Meth. **A446**, 59 (2000).

[39] *Slac report 504, "the BABAR physics book. physics at an asymmetric b factory."* (1998).

[40] B. Aubert et al. (*BABAR* Collaboration), Phys. Rev. Lett **89**, 201802 (2002).

[41] B. Aubert et al. (*BABAR* Collaboration), Nucl. Instrum. Meth. **A479**, 1 (2002).

[42] G. Fox and S. Wolfram, Phys. Rev. Lett. **41**, 1581 (1978).

[43] W. Dunwoodie, private communication.

http://www.slac.stanford.edu/~wmd/bbkinematics/kinematics.note.

[44] W. Ford, *BABAR* Analysis Document #53.

[45] ROOT. An Object-Oriented Data Analysis Framework. http://root.cern.ch/.

[46] H. Albrecht et al. (ARGUS Collaboration), Z. Phys. **C48**, 543 (1990).

[47] T. Allmendinger et al., *BABAR* Analysis Document #867.

[48] S. Mclachlin, *BABAR* Analysis Document #1056.

[49] S. Spanier, *BABAR* Analysis Document #303.

[50] K. M. Watson, Phys. Rev. **95**, 228 (1954).

[51] G. Fleming, Phys. Rev. **135**, B551 (1964).

[52] D. Morgan, Phys. Rev. **166**, 1731 (1968).

[53] J. Blatt and V. Weisskopf, *Theoretical Nuclear Physics* (New York, J. Wiley, 1952).

[54] C. Zemach, Phys. Rev. **133**, B1201 (1964).

[55] C. Zemach, Phys. Rev. **140**, B97 (1965).

[56] S. Flatté, Phys. Lett. **B63**, 224 (1976).

[57] E. Aitala et al. (E791 Collaboration), Phys. Rev. Lett. **89**, 121801 (2002).

[58] S. Kopp et al. (CLEO Collaboration), Phys. Rev. **D63**, 092001 (2001).

[59] A. Garmash et al. (Belle Collaboration), Phys. Rev. **D65**, 092005 (2002).

[60] S. Fajfer, T. Pham, and A. Propotnik, Phys. Rev. **D70**, 034033 (2004).

[61] H.-Y. Cheng and K.-C. Yang, Phys. Rev. **D66**, 054015 (2002).

[62] J. Heinrich, CDF note 5718.

[63] F. James, MINUIT Reference Manual. CERN Program Library Long Writeup D506.

[64] J. Link et al. (FOCUS Collaboration), Phys. Lett. **B621**, 72 (2005).

[65] M. Ablikim et al. (BES Collaboration), Phys. Lett. **B607**, 243 (2005).

[66] D. Barberis et al. (WA102 Collaboration), Phys. Lett. **B462**, 462 (1999).

[67] M. Achasov et al. (SND Collaboration), Phys. Lett. **B485**, 349 (2000).

[68] E. Aitala et al. (E791), Phys. Rev. Lett. **86**, 765 (2001).

[69] M. Baubillier et al., Z. Phys. **C17**, 309 (1983).

[70] D. Aston et al., Nucl. Phys. **B301**, 525 (1988).

[71] M. Ablikim et al. (BES Collaboration), Phys. Lett. **B603**, 138 (2004).

[72] M. Gronau and J. Rosner, Phys. Rev. **D72**, 094031 (2005).

[73] B. Aubert et al. (*BABAR* Collaboration), Phys. Rev. **D71**, 091102 (2005).

[74] K. Abe et al. (Belle Collaboration), Phys. Rev. Lett. **91**, 261602 (2003).

[75] A. Garmash et al. (Belle Collaboration) (2005).

[76] D. Barberis et al. (WA102 Collaboration), Phys. Lett. **B453**, 305 (1999).